STATISTICAL ANALYSIS OF ELECTROMAGNETIC COMPLEX

CAVITIES

By

NEDA NOURSHAMSI

Bachelor of Science in Electrical Engineering
Azad University
Tehran, Iran 2007

Master of Science in Mechatronics and Energy
University of Strasbourg
Strasbourg, France
2014

Submitted to the Faculty of the
Graduate College of the
Oklahoma State University
in partial fulfillment of
the requirements for
the Degree of
DOCTOR OF PHILOSOPHY
December, 2018

STATISTICAL ANALYSIS OF ELECTROMAGNETIC COMPLEX

CAVITIES

Dissertation Approved:

Dr. Charles F. Bunting
_____
Dissertation Advisor

Dr. George M. Scheets
_____

Dr. James C. West
_____

Dr. Albert T. Rosenberger
_____

ACKNOWLEDGMENTS

Words can not express how much I am thankful to my parents (Tahereh and Abbas Nourshamsi). It has almost been a decade since I am out of home and my parents have always been a constant source of inspiration and encouragement. My research and my thesis would not have been possible without their support at different levels; emotionally and intellectually.

I would like to express my gratitude to my advisor, Dr. Charles Bunting for his constant encouragement and guidance throughout the research. His technical advice and expertise in the field helped me to cross all the hurdles towards the successful completion of this dissertation.

My sincere thanks to Dr. James West and Dr. George Scheets, and Dr. Albert Rosenberger for taking part in my dissertation, and their time and feedback. My special thanks goes to Dr. Martin Hagan for his extensive contributions in chapter 4 and 6. I also would like to thank him for his excellent courses on statistical modeling. My warmest thanks to Carl Hagar at Naval Surface Warfare Center group (NSWCDD) for providing data, and his feedbacks in this dissertation.

My gratitude goes to Dr. Gustav Freyer for his expertise in EMC measurement techniques, and to Mechatronic and Energy department's committee in Univeristé de Strasbourg that gave me a chance to study in several universities around the world. I was lucky enough to be part of their program. I also like to thank all of my colleagues at Oklahoma State University, and my friends for their support. [1]

Name: Neda Nourshamsi

Date of Degree: December, 2018

Title of Study: STATISTICAL ANALYSIS OF ELECTROMAGNETIC COMPLEX CAV-
ITIES

Major Field: Electrical and Computer Engineering

In the last decades, statistical modeling of the maximum electromagnetic (EM) field has been calculated by applying extreme order statistics and the central limit theorem. However, this method only works in the over-moded regime when the parent distribution is known. In this dissertation, the Generalized Extreme Value (GEV) distribution is introduced as an alternative statistical methodology to model the maximum field level directly in different environments such as under-moded regime or a not well-stirred environment. The distribution can converge to three different asymptotic distributions which have different tails (an upper bounded or a fat tail). In order to validate the GEV distribution, mechanical stirring is used inside the reverberation chamber and the equipment under test (EUT) box. The samples from the external stirring follows a Rayleigh distribution. However, locating a small tuner inside the cavity ("internal stirring") generates a non-Rayleigh distribution. The GEV distribution is applied through samples from internal stirring in both under-moded and over-moded regimes. A maximum likelihood estimator is used to compute the parameters of the GEV distribution. The good agreement between parametric and non-parametric (empirical) samples is achieved which is of interest in the study complex EM cavities. Additionally, the effects of varying the shape parameter of the GEV distribution on the uniformity inside the reverberation chamber are presented. The typical uncertainties inherent inside a nested chamber are also assessed, which are required for statistical modeling. Finally, the GEV distribution has been used to model the maximum field level, while the quality factor of the EUT box has been decreased by locating absorbing material inside the box. This is typically representative of locating electronic devices inside the EUT box.

As an additional contribution, we introduce multi-layers perceptron (MLP) as a function approximator to estimate the dimension of materials to have a specific quality factor inside a small cavity. In other words, instead of using random number and dimension of absorbing material, we propose using a neural network to interact the process. A committee of networks and Monte Carlo cross validation are used to improve the performance of the network.

TABLE OF CONTENTS

LIST OF TABLES

LIST OF FIGURES

CHAPTER 1

INTRODUCTION

Electromagnetic compatibility (EMC) problems always involve two parties: the source of the interference (emissions) and the victim (immunity/susceptibility) [9]. A system contains equipment that can be a source (an aggressor) of emissions or can be susceptible (a victim). The equipment can act as a source and victim at the same time. The equipment can emit signals which can affect other equipment and are also susceptible to the noise in the environment. Therefore, a system is said to be electromagnetically compatible if it does not interfere with other systems, is not susceptible to emissions from other systems, nor does it cause interference with itself [9]. Figure 1.1 shows the equipment as a source and victim.
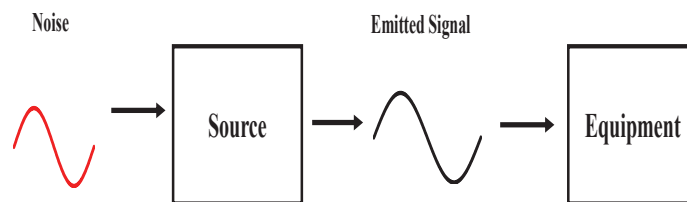
Figure 1.1: Source and Receiver.

It should be mentioned that electromagnetic energy transfers frequently with unintended coupling modes which causes interference only if the received energy has sufficient magnitude at the receiver input and causes some undesired impact on the operation of the system.

Different facilities to assess the electromagnetic compatibility include anechoic cham-

bers, transverse electromagnetic (TEM) cells, and reverberation chambers (RCs). The EMC community has proposed the use of the reverberation chambers, since they are reliable, repeatable and controllable test facilities that address a wide breadth of EMC problems. In addition, the well-established methods are available in order to perform various types of tests with reverberation chambers compared to other facilities. Especially, when the equipment under test (EUT) is an electronic device with a complex radiation pattern, performing the tests in reverberation chambers can deliver more reliable results than the more traditional methods [2]. Various standards allow the use of RCs to assess EMC including a process of performing different measurements such as these found in IEC $61000 - 4 - 21$ standard [10]. However, EMC engineers need to know the statistics of RCs in order to understand the nature of the electromagnetic environment that the EUT is exposed during a reverberation chamber assessment.

Reverberation chambers are large conductive rooms with highly reflective walls, which stir the fields or modal structure by various methods. There are three different means of obtaining a stirred environment inside the chamber: mechanical stirring, frequency stirring, and source stirring. In mechanical stirring, the tuner is rotated inside the chamber, while in frequency stirring, the frequency sweeps over some limited bandwidth and leads to the excitation of several modes. Source stirring can be achieved by changing the antenna position or using arrays of antennas on the walls in which several sources are fed sequentially [11], [12]. The stirrer decreases the variance of the field strength in the reverberation chamber which improves the accuracy of estimates of the space-averaged field strength. The advantage of using a reverberation chamber is that the EUT does not need to rotate inside the reverberation chamber. In addition, the existence of multi-path and reflections inside the reverberation chamber results the random phase and polarization between all waves, which is a key property of reverberation chambers for EMC testing and help us to mimic a harsh electromagnetic environment.

A diagram of a reverberation chamber with antennas at Oklahoma State University is

Figure 1.2: Reverberation Chamber (SMART-80) at Oklahoma State University with vertical tuner.

(a) Shielding box inside a spacecraft.

(b) HERP/O environment.
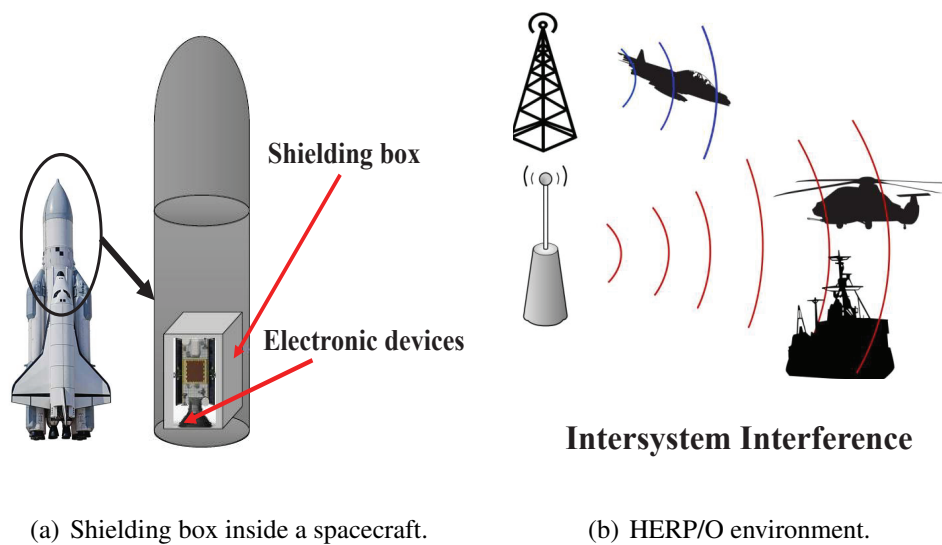
Figure 1.3: Unknown Interferences at different situations.
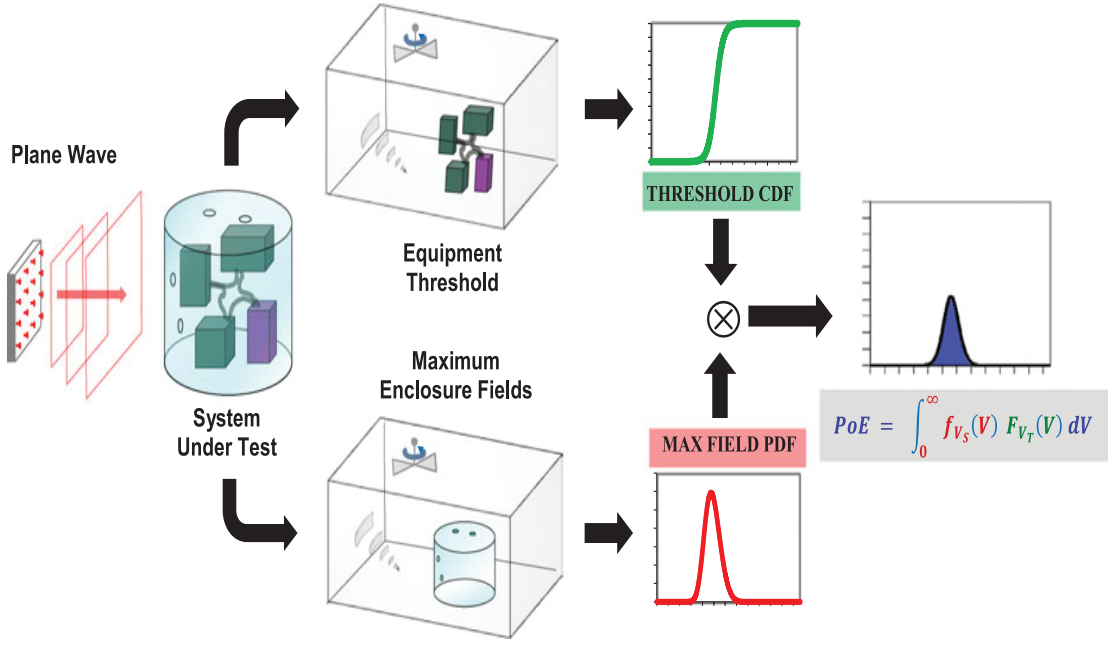
Figure 1.4: EMPAT framework [1].

shown in Figure 1.2. The reverberation chamber includes one horizontal and one vertical tuner at the corners, which stir the energy inside the chamber and change the boundary conditions. The transmitter antenna sends energy inside the reverberation chamber and the receiver antenna receives the energy as input to the Vector Network Analyzer (VNA). The VNA measures transmission and reflection coefficients that are critical parameters for RC characterization.

In recent decades, statistical modeling inside reverberation chambers is a topic of interest since it can be used in different types of EMC testing such as immunity testing, which is useful to understand the unknown interferences during launch phase of a spacecraft. The current certification test methods for the mentioned types of testing cannot meet the requirements for the higher field or power level since the present testing equipment are not able to generate the required high radio frequency (RF) power. Additionally, generating the necessary high field level or power could be dangerous for a person who conducts the testing and also provides the equipment and facilities will be costly [1]. Therefore, an alternative statistical method could be advantageous due to the mentioned reasons. Figure 1.3

4

shows an example of a spacecraft, and hazards of electromagnetic radiation to ordnance or personnel (HERO/P). The unwanted electromagnetic interferences can happen in two mentioned scenarios due to the high level of power during launch phase or to a new generation of Naval radar system in HERO/P environment.

Hagar et *al.* in [1] introduced an electromagnetic probability-of-effect assessment tool (EMPAT), which includes two different phases in order to "statistically assess safety margin to failure under any electromagnetic environment (EME) threat". Figure 1.4 shows the EMPAT framework. In the first phase, the external stress field is assessed by using a shielding effectiveness transfer function of the EUT. Notably, all of the electronic devices would interact with the maximum field in the electromagnetic environment (EME), so the distribution of maximum field is considered here. In that case, the Generalized Extreme Value distribution is presented, which is a generalization of three different asymptotic distributions, Gumbel, Fréchet and reverse Weilbull, that are recognized based on the sign of the shape parameter. This distribution is important since it can be used to model the maximum samples obtained from any parent distribution, and can also converge to either a fat tail distribution or an upper bounded distribution, which is helpful to predict the higher field level.

In this work, we will validate experimentally the GEV distribution inside a nested chamber. The test method is designed by applying only mechanical stirring inside the reverberation chamber (called external stirring) and the cavity box (called internal stirring). The test cavity is covered with two different aperture dimensions (small and large) which also can affect the type of parent distribution. A goodness of fit test is used in order to check the type of distribution inside both the reverberation chamber and the cavity. The maximum field distribution will be modeled inside the cavity box in both under-moded and over-moded regimes. Notably, Lehman and Freyer's methodology in [13] is not applicable for under-moded regime (there is a disagreement in types of parent distribution in under-moded regime [14], [15]) or when the parent distribution is not known. The typical uncertainties

inherent inside a nested chamber will be explained which are necessary to complete the statistical model. Electronic devices inside the reverberation chamber can be represented by loading the reverberation chamber. Therefore, the GEV distribution will be validated while the enclosure is loaded by absorbing material. In order to load the enclosure, a random number of absorbing material or random dimension is used. If the absorption is not enough, we will decrease or increase the dimension of absorbing material. As an alternative to this approach, a neural network applications (function approximator) was used in order to estimate the required absorbing dimensions inside the enclosure to have a specific amount of quality factor. Finally, the uniformity inside the reverberation chamber will be introduced and the relation between uniformity and the GEV parameter (only the shape parameter) will be assessed.

The outline of this work is as follows. Chapter 2 gives an overview of reverberation chambers and their application in various types of measurements. Chapter 2 also discusses important parameters and statistical properties that need to be considered in the reverberation chamber measurement and analysis. The effects of loading the reverberation chamber on the quality factor are described. Two types of tests are explained in detail, and the statistical theories used in these tests are described. Chapter 3 explains in detail the fundamental concepts in estimation theory and presents the maximum likelihood estimator and the Generalized Extreme Value (GEV) distribution. The results of applying the distribution inside the reverberation chamber for narrow band frequency are shown. Chapter 4 presents the application of the GEV distribution in the situation when the parent distribution is not clear. The results are shown while the EUT box is at both over-moded and under-moded regimes. Typical uncertainties associated with the statistical analysis are described and computed. Chapter 5 shows the results of the GEV distribution while the enclosure cavity is loaded. The results are presented for different values of quality factor inside the box. The effects of loading on the confidence intervals are also described. Chapter 6 explains one of the neural network applications (function approximator) to compute the required dimension of

absorbing materials inside the EUT box to have a specific amount of quality factor. For this purpose, multi-layer perceptron is used by applying the committee of networks and Monte Carlo cross validation. Chapter 7 presents the relation between the GEV distribution and the uniformity inside a reverberation chamber. The effects of loading on the number of independent samples are shown. The traditional method to calculate the maximum field level was compared to the GEV distribution. Chapter 8 summarizes the work and presents conclusions and suggestions for future work.

CHAPTER 2

LITERATURE REVIEW

2.1   Overview of Reverberation Chamber Theory

A reverberation chamber (RC) is a test facility that provides statistically uniform, isotropic, and randomly polarized field. These characteristics make the reverberation chamber a robust and all aspect angle test facility, which can be used in several applications such as antenna efficiency, immunity testing and shielding effectiveness.

A vector network analyzer (VNA) can provide an integrated measurement solution that is relatively reliable and accurate in the RC measurements. In addition, S-parameters can be used to show the behavior of the antennas, electric and magnetic field in the reverberant environment. Collecting reflection coefficient (S_{11}) can be used to correct the antenna efficiency. Insertion loss (S_{21}) is another important scattering parameter, which can help to better analyze some concepts such as shielding effectiveness [16] and the maximum power or field level inside the RC [13]. As an alternative, measurements can be performed using a signal generator to inject a signal into the cavity, while a spectrum analyzer measures the signal.

The highly conductive surfaces inside the RC create boundary conditions that must satisfy Maxwell equations. A Reverberation chamber is electrically large which refers to an enclosure that supports several modes (combination of electric and magnetic fields) at the lowest frequency of interest [17]. The excitation of the particular modes is dependent on the strength of the coupled source field into them. The measured field at any single point will be the summation of the modes at that point inside the cavity. The randomization of the field is achieved by varying boundary conditions of the chamber walls. Changing

8
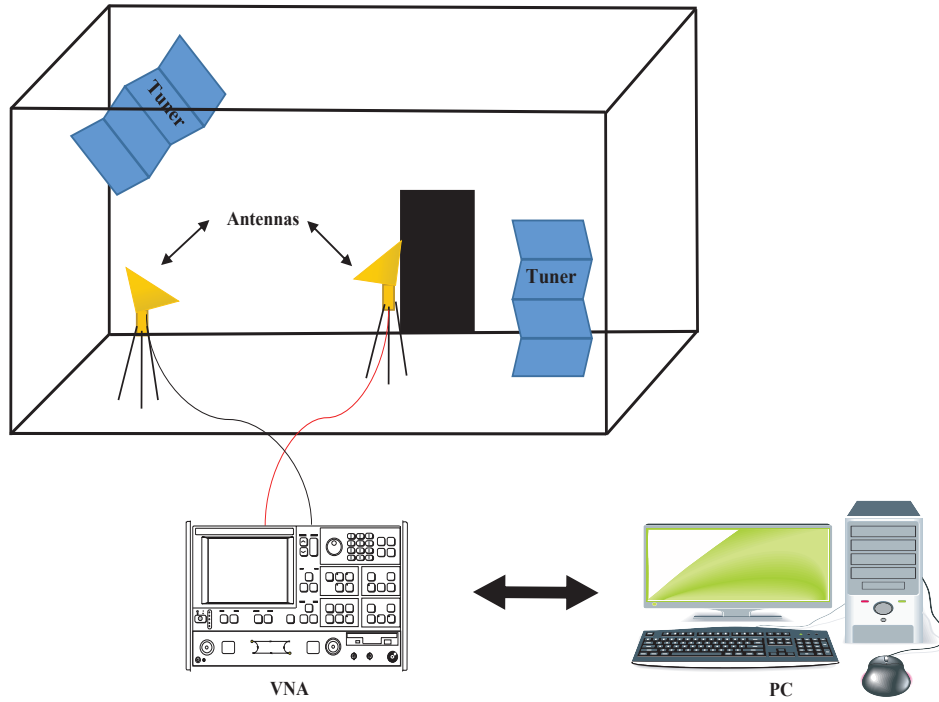
Figure 2.1: A diagram of an RC, tuners and antennas.

boundary condition would happen by applying two major approaches; Mechanical stirring and frequency stirring. Mechanical stirring can accomplished by using a tuner, which is electrically large and placed in a portion of the chamber volume. The equipment under test (EUT) inside RC is exposed by random fields in all directions compared to performing the measurements inside anechoic and semi-anechoic chamber, which the EUT needs to be turned in different directions. An alternative approach is frequency stirring. In this method, the frequency is sweeping over a narrow bandwidth of frequencies [18] and several different modes are excited in the frequency range.

Figure 2.1 shows the measurement setup that was used in this dissertation. The reverberation chamber has two z-fold tuners at the corners. The chamber connects by coaxial cables to bulkhead connectors through the walls and the VNA. The VNA collect data as S-parameters which will use to solve different EMC problems.

The measurement results shown in this work were taken using a VNA, and multiple

9

different types of antenna in the different locations inside the reverberation chamber.

2.2   Statistical Description inside Reverberation Chamber

Hill in [19] used a plane wave integral representation for well-stirred fields inside the RC. The statistical properties of the fields were derived from the angular spectrum by sampling the fields randomly at fixed incident angels. Hill showed the EM field at each position in the RC can be decomposed to in-phase and quadrature parts, which are statistically independent and have Gaussian (normal) distribution. Therefore, six parameters are described the total field inside the RC. The equations can be defined:

$$E_x = E_{xr} + jE_{xj}, \tag{2.1}$$

$$E_y = E_{yr} + jE_{yj}, \tag{2.2}$$

$$E_z = E_{zr} + jE_{zj}. \tag{2.3}$$

The real part of the x component of electric field follows Gaussian distribution:

$$f_X(\lambda) = \frac{1}{\sqrt{2\pi}.\sigma_x}.e^{\frac{-(\lambda)^2}{2.\sigma_x^2}}, \tag{2.4}$$

where σ_x shows the standard deviation of the real component of the electric field in the x direction. The real and imaginary parts of all orthogonal components of the electric and magnetic fields have the same expression as well. The magnitude of E_x, E_y and E_z can be defined:

$$|E_x| = \sqrt{(E_{xr})^2 + (E_{xj})^2}, \tag{2.5}$$

$$|E_y| = \sqrt{(E_{yr})^2 + (E_{yj})^2}, \tag{2.6}$$

$$|E_z| = \sqrt{(E_{zr})^2 + (E_{zj})^2}. \tag{2.7}$$

The χ distribution with ν degree of freedom is defined:

10

$$f_X(\lambda) = \frac{2}{2^{(\frac{2}{v})}.\sigma^v.\Gamma(\frac{2}{v})}.\lambda_{(v-1)}.e^{-(\frac{\lambda}{2\sigma_x^2})}, \qquad (2.8)$$

where the value of Γ-function can be obtained:

$$\Gamma(\lambda) = \int_0^\infty e^{-t}.t^{\lambda-1}.dt. \qquad (2.9)$$

If $v = 2$, Rayleigh distribution (χ_2) is defined by using equation 2.8. The magnitude of total field is χ distribution with 6 degrees of freedom ($\chi_{(6)}$). The $\chi_{(6)}$ distribution is defined:

$$f_Y(\mu) = \frac{1}{4.\sigma^6.\Gamma(3)}.Y^5.e^{-(\frac{\mu}{2\sigma^2})}, \qquad (2.10)$$

where

$$Y = \sqrt{|E_x|^2 + |E_y|^2 + |E_z|^2}. \qquad (2.11)$$

In the measurement or simulation, the power has chi-squared distribution (χ_v^2) distribution with v degrees of freedom, which can be defined defined:

$$f_Z(\theta) = 2^{(\frac{v}{2})}.\Gamma(\frac{v}{2}).\theta^{\frac{v}{1}-1}.e^{(\frac{\theta}{2})}, \qquad (2.12)$$

where

$$Z = Y^2 = E_x^2 + E_y^2 + E_z^2. \qquad (2.13)$$

The χ^2 distribution with 2 degrees of freedom (Exponential distribution) shows the received power for a single component inside the reverberation chamber. Similarly, the total power with all three components will follow $\chi_{(6)}^2$ distribution. Figure 2.2 shows the PDFs of Gaussian, $\chi_{(2)}$, $\chi_{(6)}$, $\chi_{(6)}^2$ distributions inside the reverberation chamber that represent respectively the real part of electric field, E field in x-component, total E field and the magnitude of the power for full stirrer rotation inside the reverberation chamber.

11
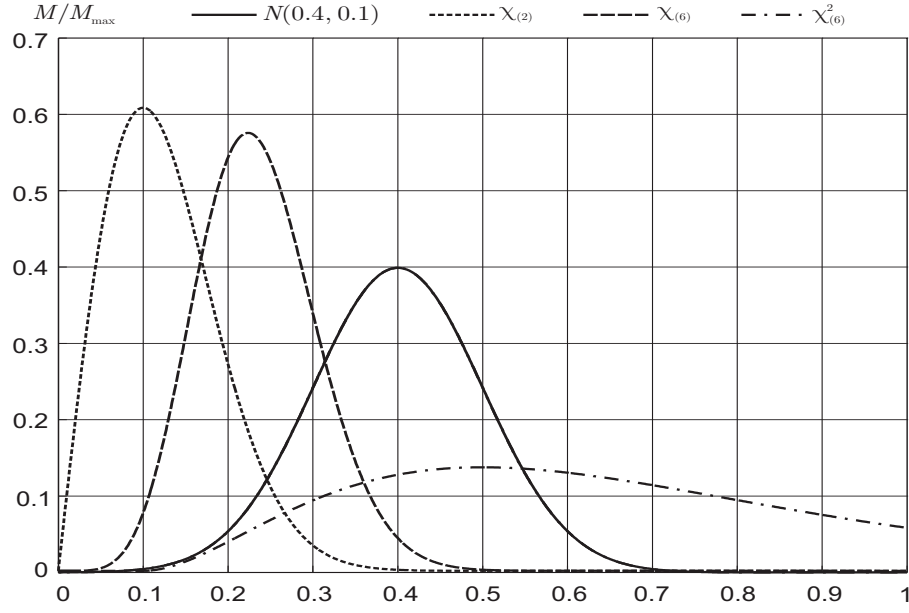
Figure 2.2: Gaussian, $\chi_{(2)}$, $\chi_{(6)}$, $\chi_{(6)}^2$ distributions (normalized over the maximum) [2].

Hill in [19] used the superposition of uniform plane waves directly to derive Rayleigh distribution. Assefa et al. showed in [20] a new method to reduce the computational load. The new method used the reciprocity theorem to excite the field and showed the induced current inside the EUT has Rayleigh distribution. Hill presented all of the defined statistical properties in the over-moded regime, which can be as [21]:

- The over-moded regime starts at the frequency which sixty modes exist inside the reverberation chamber.

- The over-moded regime starts at either three or six times the first dominant modes inside the RC.

In this work the components E_R and E_R^2 which follow Rayleigh and Exponential distributions are called the parent distributions.

2.3 Important Parameters inside Reverberation Chamber

One of the critical parameters of the chamber operation is the quality factor (or Q). The standard quality factor for over-moded regime can be defined [22] as a fraction of stored energy over the dissipated energy as following:

$$Q = \frac{\omega.U}{P_d}, \qquad (2.14)$$

where P_d shows dissipated energy. However, when the chamber is in an under-moded regime, the quality factor can be defined for a single mode as a fraction of center frequency over the half-power bandwidth:

$$Q \approx \frac{f_c}{\triangle f}. \qquad (2.15)$$

There are two different methods to measure the Q, one in the frequency-domain [10] and one in the time-domain [23]. The common method to estimate the Q in frequency domain is [10]:

$$Q \approx \frac{16.\pi^2.V}{\lambda^3 \eta_1 \eta_2} < \frac{P_r}{P_t} >, \qquad (2.16)$$

where

$$< \frac{P_r}{P_t} > \propto < |S_{21}|^2 >, \qquad (2.17)$$

and η_1 and η_2 are the efficiencies of the two antennas when operating in free space. The antenna efficiencies are given by (assuming two identical antenna as transmitter and receiver):

$$\eta_1 = 1 - |S_{11}^{FS}|^2, \eta_2 = 1 - |S_{22}^{FS}|^2, \qquad (2.18)$$

where S_{11}^{FS} and S_{22}^{FS} are the measured reflection coefficients of antennas in free space.

In the time domain, the quality factor (Q) of the chamber is directly related to the decay rate of the energy within the chamber. The mean time-domain response can be divided into

13

two distinct phases, the pre-reverberant phases where energy is being distributed across resonant modes within the the chamber and the reverberant phase where the energy level exponentially decays due to losses. The losses can be due to conductive losses on the walls, tuner, and other objects within the chamber, leakage from imperfect shielding of the enclosure, and loading by the signal-source and receive (if included) antennas. The decay time of the energy within the cavity represents a power-loss profile that can be used to find the Q. The chamber time constant is defined as [24]:

$$\tau = \frac{4.3429}{Slope\frac{dB}{\mu s}}(\mu s),\qquad(2.19)$$

where the slope term is the slope of the mean chamber time-domain response in $\frac{dB}{\mu S}$ in the reverberant phase of the response (which is linear since the exponential decay is represented in dB). The chamber quality factor is then found from

$$Q = 2\pi f_c \tau.\qquad(2.20)$$

where f_c is the frequency at the center of the time domain signal bandwidth. The mean time domain response will typically be noisy despite the averaging over multiple tuner positions. A linear regression is therefore typically applied to the reverberant phase response and Q found from the slope of the regression line. The bandwidth of the signal required to perform a Q measurement in the time domain has not been well established. Richardson [24] suggested that the bandwidth should be sufficiently large that the pulse duration is small compared to the chamber wall scattering time to allow comparison with continuous-wave (CW) measurements made at the band center. In some cases, however, this requirement can lead to such a large bandwidth that it is difficult to interpret the resulting measured Q as that at a single frequency. Nourshamsi et *al.* [23] has been recently shown that the bandwidth had little effect on the measured quality factor. It therefore does not appear that the signal bandwidth must be sufficiently high that the equivalent pulse duration is smaller than the wall scattering time. Instead, it appears that it is sufficient for the pulse to be small
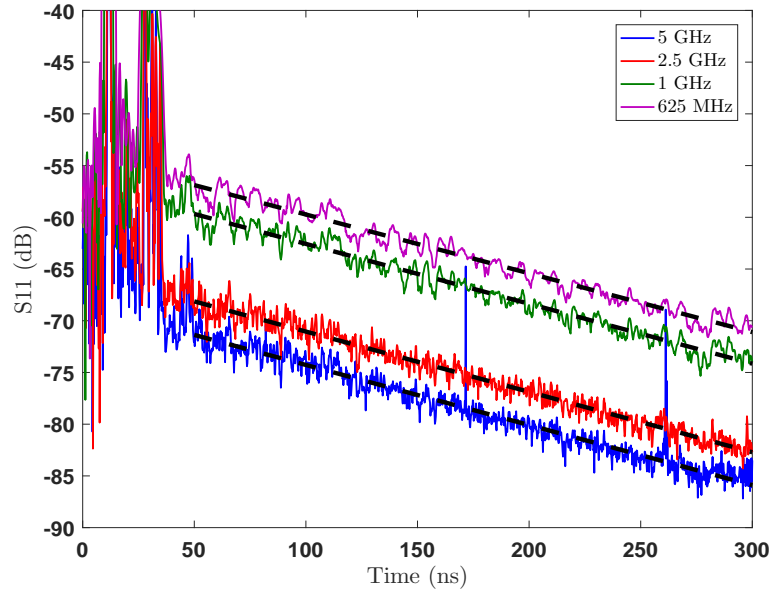
Figure 2.3: Measured mean chamber time-domain response for different signal bandwidths for unloaded chamber.

compared to chamber build-up and total measurement times. In fact, use of a narrower bandwidth pulse should give a more realistic representation of the chamber quality factor at the band center. Figure 2.3 shows the results of decay time in 5.5 GHz center frequency. Measurements were performed with bandwidths of 5 GHz, 2.5 GHz, 1 GHz, and 625 MHz. The largest bandwidth was chosen so that [24] was met when accounting for some loss of effective bandwidth due to the Kaiser-Bessel window used in forming the time-domain signal. It is noted that there is considerable overlap of the measurement bandwidths for adjacent frequencies when the measurement bandwidth is 5 GHz and none when the bandwidth is reduced to 625 MHz. The corresponding equivalent pulse durations are 0.4 ns, 0.9 ns, 2 ns, and 3.2 ns.

The measured Quality factor can be related to other test characteristics of the chamber such as number of independent samples, coherence bandwidth, the RMS delay spread for the time domain response of the chamber, the chamber's decay time [25], [26], [27].

Identifying the number of independent samples is critical, since the accuracy inside the

15
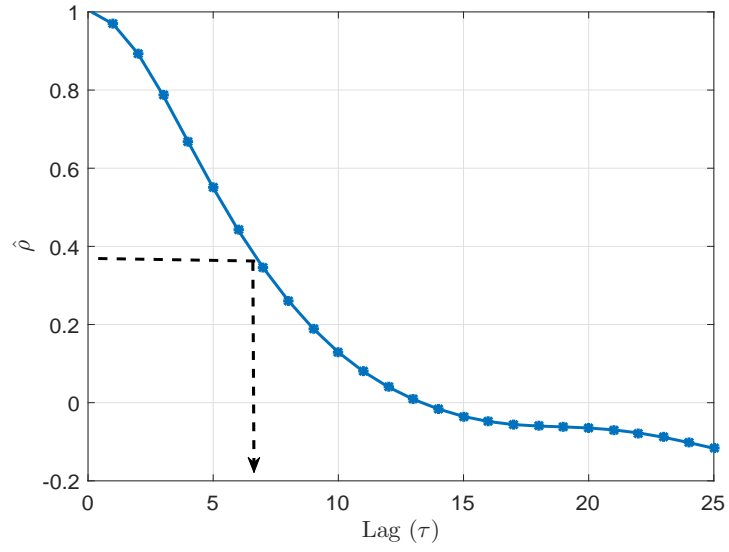
Figure 2.4: The auto correlation function and the offset ($\Delta = \frac{1}{e}$) at which the correlation is lost.

RC measurements relies on having a sufficient number of independent samples. In the other words, the number of independent samples is related to the estimation of the uncertainty associated with the test. In fact, the number of independent samples, that is, the number of the samples that are uncorrelated, are used to calculate the magnitude of the standard deviation (σ), which is important for defining the statistical environment inside the RC.

The number of independent samples can be computed in mechanical stirring and frequency stirring. In mechanical stirring, the number of tuner positions lead to the number independent, while in frequency stirring measurement samples are collected in a frequency range, but the frequency band with should not be too large to change the value of Q significantly. In both methods, the number of independent samples can be shown by using autocorrelation function (ACF) of the measured samples.

For an observed series $x_1, ... x_N$ and a lag of h, the estimated ACF is [10]:

$$\hat{\rho} = \frac{1}{N-1} \frac{\sum\limits_{i=1}^{N} (x_i - \bar{x})(x_{i-h} - \bar{x})}{\hat{\sigma}_x^2}, \tag{2.21}$$

16

where $\hat{\sigma}_x$ is the estimated standard deviation and defines:

$$\hat{\sigma}_x = \frac{1}{N-1} \sqrt{\sum_{i=1}^{N} (x_i - \bar{x})^2},$$

and the estimated sample mean is calculated as:

$$\bar{x} = \frac{1}{N} \sum_{i=1}^{N} x_i.$$

An operationally common practice assumes that $\hat{\rho} < \frac{1}{e}$ implies independence [10]. Figure 2.4 shows ACF and the offset (Δ) at which the correlation is lost.

2.4   Loading the Chamber

The quality factor can be affected by loading the chamber. The absorbing materials are used to change the quality factor inside the RC. Coder et al. showed in [28] effects of placing absorbing materials in different locations inside the reverberation chamber. The results were presented in terms of insertion loss in order to calculate the absorber effectiveness (A.E.), which is the difference between the insertion loss of empty chamber and the insertion loss of loaded chamber.

$$A.E. = <|S_{21}|^2>_{empty} - <|S_{21}|^2>_{loaded}. \tag{2.22}$$

Nourshamsi et al. showed in [29] the effects of absorbing materials with the same volume and different surfaces inside the enclosure. The results was shown as absorption reduction in Q which defines:

$$\Delta Q = Q_{empty} - Q_{loaded}. \tag{2.23}$$

Figure 2.5 shows the decay rate of S_{11} inside an enclosure. It can be seen the decay time will be faster when the chamber is loaded. Figures 2.6(a) to 2.6(c) show the shapes of the absorbing materials. Figure 2.7 shows the location of absorbing materials inside the
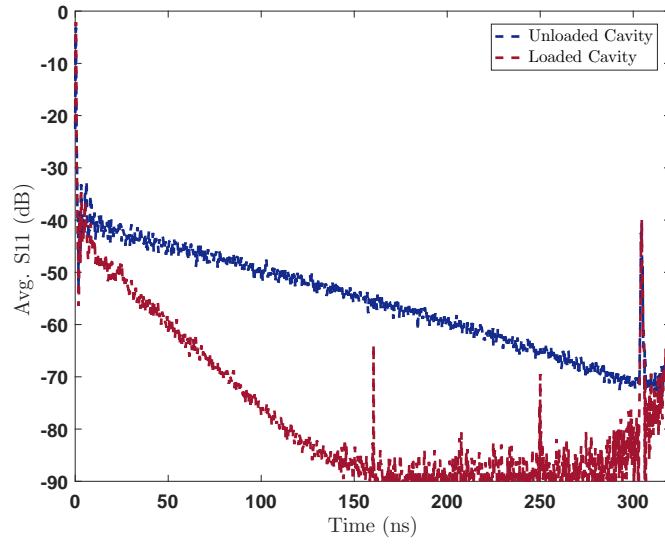
Figure 2.5: Averaged S_{11} for unloaded and loaded cavity.

(a) Sphere. (b) RP1. (c) RP2.

Figure 2.6: Absorbing material shapes.

cavity. As can be seen, rectangular parallelepiped (RP1) was located on the wall (position 1) or in the corner horizontally (position 2) and vertically (position 3).

It is necessary to mention that the surface area in Position 1 to 3 are as follows:

$$S_{Position1} > S_{Position2} = S_{Position3}, \qquad (2.24)$$

and the volume of RP1, RP2 and sphere are as follows:

$$V_{RP2} > V_{RP1} > V_{sphere}. \qquad (2.25)$$

18
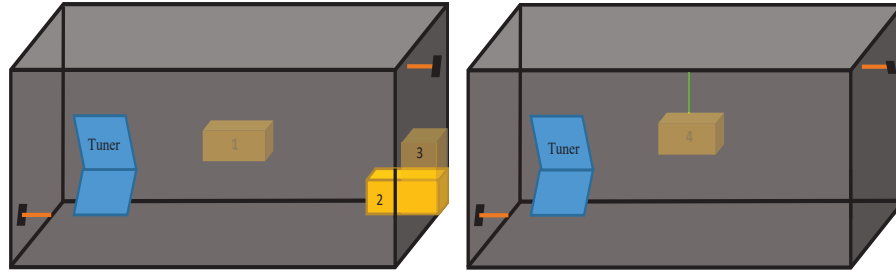
(a) Material locations on the walls of the (b) Material location inside the working
enclosure.   volume of the enclosure.

Figure 2.7: Location of absorbing materials.

Figures 2.8 and 2.9 show respectively the reduction in Q of different position of RP1 versus various center frequencies on the surface area and the different shapes versus various center frequencies inside the working volume.
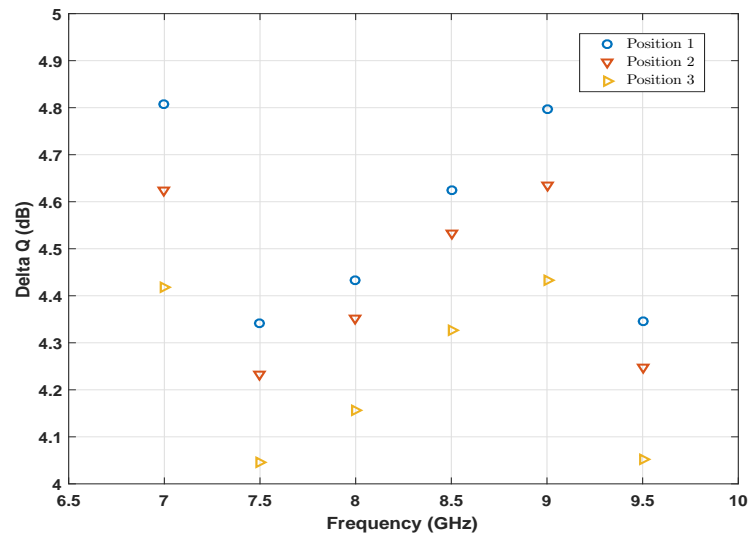
Figure 2.8: Comparison of Q factor vs different positions on the walls of the enclosure.

On these plots, it can bee seen that by placing absorbing materials with largest surface area on the cavity wall or in the working volume of the enclosure, the material will absorb the energy and we will have higher Q reduction (more losses). The surface area hypothesis is accepted by using one shape of material with various surface areas in three different

19

locations on the wall surfaces of the cavity, in the corner (vertically and horizontally), and three different shapes of materials with the same volume and different surface area inside the working volume of the cavity. It is shown that materials with the largest surface area absorbs the most energy inside the working volume since all of the surfaces can absorb energy.
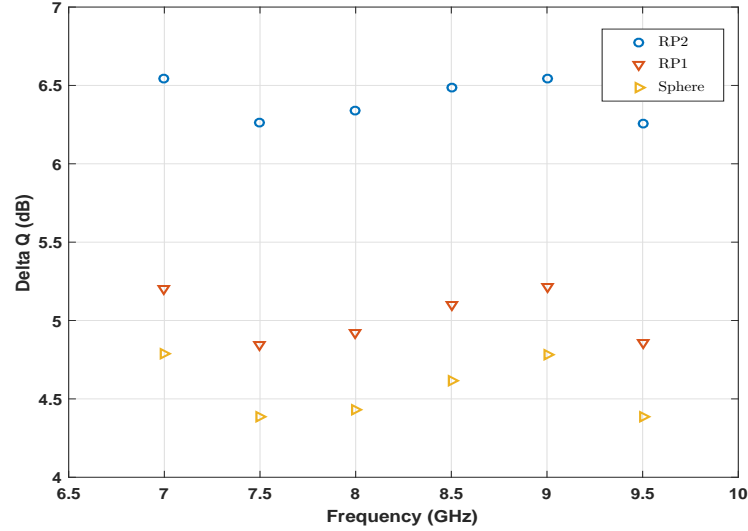
Figure 2.9: Comparison of Q factor vs different loading shapes in the working volume of the enclosure.

2.5 Testing in Reverberation Chamber

The use of RCs for various applications in avionics, automotive, and consumer testing is allowed today by several military and commercial standards [10]. In recent years, immunity tests are being increasedly performed in RCs since there is no need to rotate the EUT and they have the capability to generate high field levels. In immunity testing, knowing the statistical properties of the RC will be vital since the maximum power or field level at each frequency should be known. The statistical theory for electromagnetic environment (EME) is represented by the χ^2 and χ distributions with two degrees of freedoms respectively for the power level and field strength.
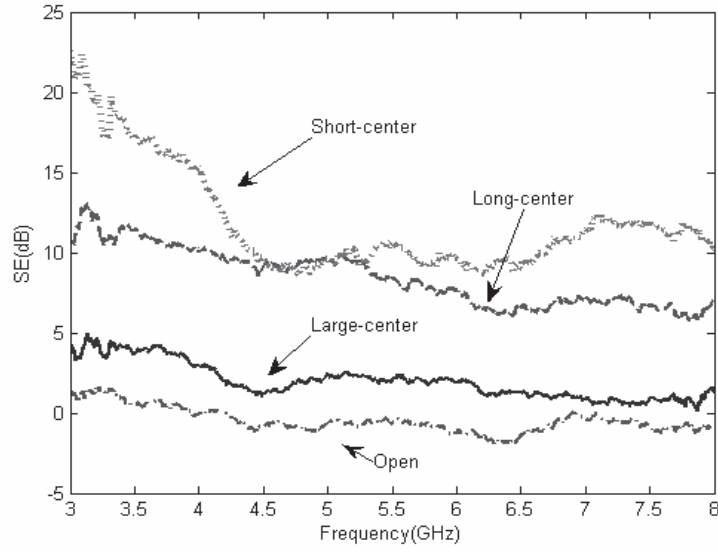
Figure 2.10: Effects of aperture dimension on shielding effectiveness [3].

There are several methods to find the maximum level of field or power inside the RC. Lehman et *al.* in [13] presented the Extreme Value Theory to find the maximum distribution of the power inside the RC. The theoretical and the experimental results of Extreme Value Theory had a good agreement. The maximum distribution has a long flat tail, which is important in several types of the tests. But, this method is not applicable in under-moded regime or not well-stirred reverberation chamber.

He et *al.* showed [3] that the magnitude of a component of the electric field in frequency stirring has different distributions inside the cavity due to aperture sizes. When the energy is induced inside the nested cavity (small box with aperture inside the reverberation chamber) which has a large aperture, the two cavities act as one chamber in terms of electromagnetic field. However, when the aperture dimension is small, the environment inside the box and the chamber should be independent. The author showed the results in terms of shielding effectiveness (SE). Figure 2.10 shows the results of SE for different aperture dimensions inside the nested chamber. As can be seen the SE changes due to aperture dimension. When the aperture is large, shielding effectiveness is really low and when the aperture is small, shielding effectiveness is really high.
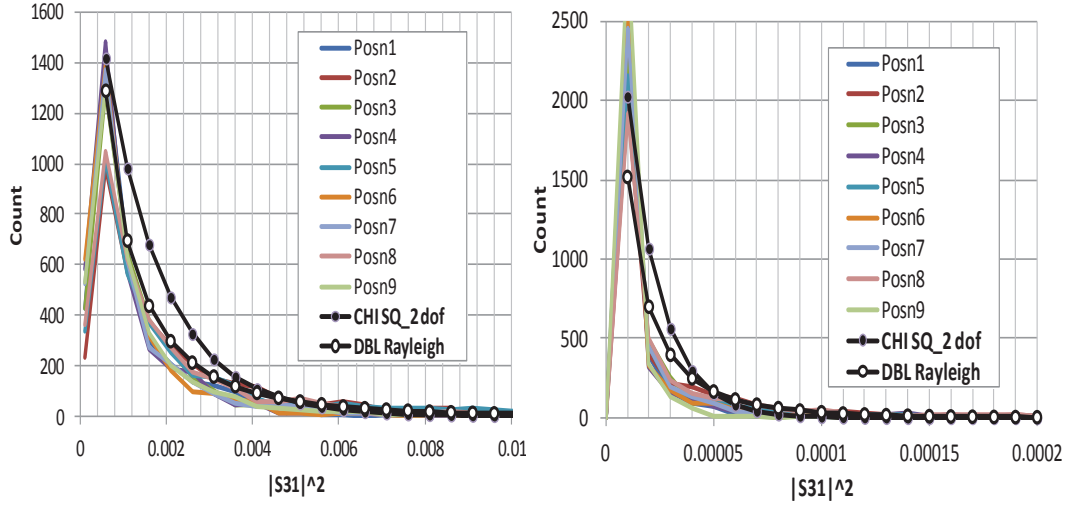
Figure 2.11: Histograms of data with Rayleigh and Double-Rayleigh distributions; large aperture (left) and small aperture (right) [4].

Kovalevsky et *al.* [30] recently presented statistical energy analysis (SEA) that predicts the mean and the variance of the EM response for a cavity with a circular aperture in a reverberation chamber for high frequencies. The SEA prediction uses the concept of the Gaussian Orthogonal Ensemble (GOE), but the advantage is that GOE does neither model the cavity structure nor apply Monte Carlo simulation. Therefore, the SEA consumes lower time compared to numerical simulation, which uses the Maxwell equations to provide the results.

Bremner et *al.* in [4] extended this foregoing model to estimate the mean and maximum of the induced current inside the small box with various aperture dimensions, which was located in the reverberation chamber and validated it experimentally. However, the experimental results showed different distributions by applying frequency stirring due to dimension of the aperture of the small box. Bremner showed the model requires minimal EMC design information and solves orders of magnitude faster than existing numerical models, but the model requires a knowledge about the parent distribution (for field or power) in each frequency. Figure 2.11 shows the histograms of Rayleigh and Double-Rayleigh dis-
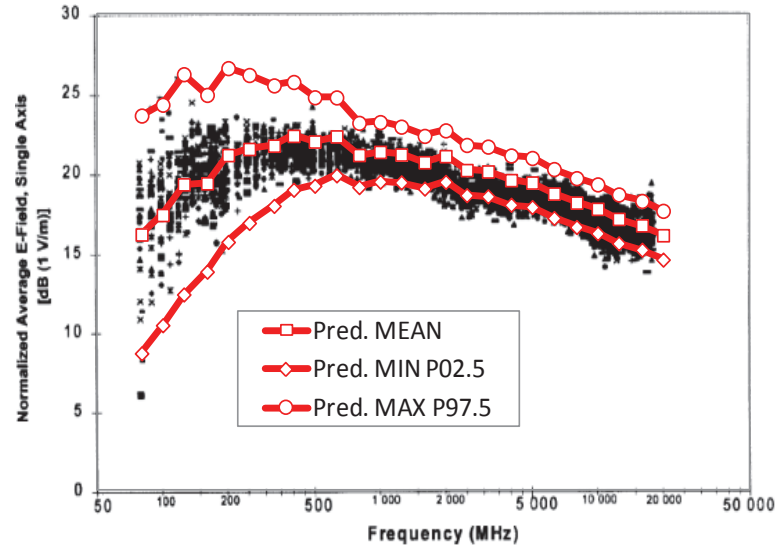
Figure 2.12: Predicted maximum and minimum for $\text{Avg}[E_r]$ in the RC [4].

tributions inside the nested chamber with two different apertures. The measurements were performed inside the nested chamber with large and small aperture. The probe was located in 9 different positions inside the box and S_{21} are collected for frequency range from 800 MHz to 2 GHz.

Bremner also applied the model to predict the mean, maximum and minimum value for average electrical field in x-component in mechanical stirring. Figure 2.12 shows the results for maximum and minimum for electrical field in one component for frequency range from 800 MHz to 2 GHz for nine different probe positions inside the nested chamber. As can be seem, the method relies on the parent distribution.

Orjubin [5] presented the Generalized Extreme Value (GEV) distribution to find the maximum field inside the RC. The distribution is a family distribution that includes:

- The bounded distribution which is called reverse Weilbull distribution and the Fréchet distribution with fat tail in order to project high field level.

- The GEV distribution has the advantage of finding the maximum distribution without a *priori* knowledge about the parent distribution.

23
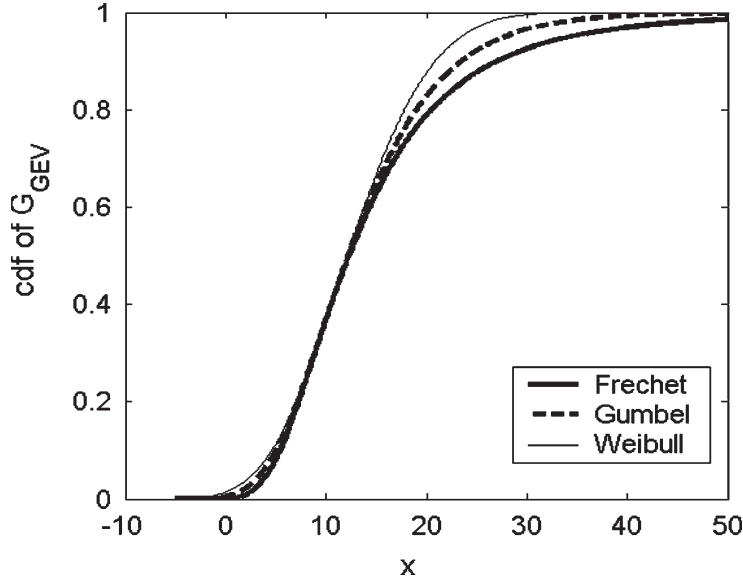
Figure 2.13: CDF Plot of the GEV distribution (field) with Enclosure in over-moded regime [5].

Figure 2.13 shows the CDF plot of GEV distribution of field level inside an enclosure. Orjubin simulated a chamber by using Finite Element Method (FEM) and used the data to prove the new maximum distribution inside an empty chamber in the over-moded and under-moded regimes.

Hagar et *al.* in [31] validated experimentally the GEV distribution for an unloaded chamber in over-moded regime. The author covered the entire outside body of the chamber with the absorber and located the antenna outside to the front of the chamber aperture. However, the effects of aperture shapes and dimension in a nested chamber need to be shown and verified. In addition, the independency of GEV distribution from the parent distribution is still required to be experimentally validated. Finally, all mentioned results need to be verified in the loaded nested chamber, when Q is decreased.

2.6 Conclusion

This concludes the review of previous work related to this research. Hill showed that for electrically large or over-moded reverberation chamber, the rectangular electric field component from external stirring inside the nested chamber E_R and E_R^2 always follow respectively Rayleigh and Exponential distribution. The common method to find the maximum level of power or field is based on Extreme Value Theory [13] and [10]. This means the maximum level of field or power is dependent on E_R distribution (the parent distribution). Kovalevsky [30] and Bremner [4] provide the SEA model to estimate the maximum and mean of induced current inside a nested chamber in frequency stirring, but this method only works if there is a *priori* knowledge about the distribution inside the box. In addition, it seems that the distribution changes due to aperture dimension in frequency stirring.

Orjubin and Hagar provided the new distribution to extract the maximum level of field or received power inside the RC directly. The advantage of this distribution is that it can provide the maximum level of field or power directly without having a knowledge about parent distributions. This distribution might be helpful in a nested chamber with large apertures inside the box and have an internal stirring, which the statistical analysis does not show any specific type of distributions. This work will further investigate the GEV distribution and seek to apply it in the different possible measurements, various regimes or at multiple locations inside the RC (which do not have the parent distributions), while the equipment under test (EUT) is either unloaded or loaded.

CHAPTER 3

GENERALIZED EXTREME VALUE DISTRIBUTION

In this chapter our discussion begins with a brief review of the parametric estimation and explanation of maximum likelihood estimator. Likelihood function is defined as a key role that can be used to find the location that a parameter is maximized. In section 3.2, we introduce extreme value theorem and Generalized Extreme Value (GEV) distribution. Additionally, effects of aperture dimension on the maximum level of field inside the nested chamber in over-moded regime are shown and analyzed. Anderson Darling test is presented to check the type of distribution inside nested chambers. Finally, the effect of probe location is analysed by using data blocking to show the mean and the variance of the maximum data in each probe location. [1]

3.1 Parametric Estimation Method

Before going into the details of the statistical properties inside the reverberation chamber, we need to get into some fundamental concepts in stochastic system which is the basis of statistical description inside the reverberation chamber. The process of using sample data to estimate the parameters of the selected distribution is called parameter estimation. Parameter estimation plays a vital role in accurately describing system behavior through mathematical models such as statistical probability distribution functions. In this work, the notation $\hat{\theta}$ and $E[\theta]$ show the estimated parameter and mean of the parameter respectively.

---

[1]This chapter was presented under the title "Effects of Aperture Dimension on Maximum Field Level Inside Nested Chambers by Applying the Generalized Extreme Value Distribution", N. Nourshamsi, J.C. West, C.F. Bunting, IEEE EMC Symp., 2018 [32].

There are two important parameters in any type of estimators; bias and variance. The two mentioned parameters could be useful to show the accuracy of the estimator. The bias could be defined as [33]:

$$B_{\hat{\theta}}(\theta) = E_{\theta}(\hat{\theta}) - \theta, \tag{3.1}$$

and the variance could be defined [33]:

$$V_{\hat{\theta}}(\theta) = V_{\theta}(\hat{\theta}). \tag{3.2}$$

It is important to mention that the variance and the bias are both function of θ which is usually an unknown constant. In any type of the estimator, there is a relationship between bias, variance and the mean-square error (MSE), which can be defined [33]:

$$E_{\theta}[(\theta - \hat{\theta})^2] = B_{\hat{\theta}}(\theta)^2 + V_{\hat{\theta}}(\theta), \tag{3.3}$$

So the MSE of an estimator can determine how far off the estimator is "on average". The estimator is unbiased if

$$B_{\hat{\theta}}(\theta) = 0. \tag{3.4}$$

We will present maximum likelihood to estimate the parameters in section 3.1.1 which is a linear unbiased estimator.

3.1.1 Maximum Likelihood Estimator

One of the important concept in the parametric estimation is the idea of maximum likelihood (MLE) since it can be used in any type of parametric family of distributions in any class of distributions for finite set of parameters $(\theta_1, \theta_2, ..., \theta_n)$. The idea of MLE is "to choose the parameter $\hat{\theta}_{ml}$ under which the observed data, was most likely" [33]. In fact, the $\hat{\theta}_{ml}$ would maximize the likelihood function and the distribution can be modeled by having

the estimated parameter. We use maximum likelihood estimators since they are very good in large sample properties, consistent, and asymptomatically efficient.

If X and Y are random variables, Bays rule can be defined [33]:

$$f_{Y|X}(\mu|\lambda) = \frac{f_{X|Y}(\lambda|\mu).f_Y(\mu)}{f_X(\lambda)}, \tag{3.5}$$

where $f_{Y|X}(\mu|\lambda)$, $f_Y(\mu)$ present respectively posterior and prior densities. The likelihood can be defined as the posterior density, when the prior density is constant.

If the set of samples $X_1, X_2, ..., X_n$ are independent and identically distributed random variables. We assume data are sampled from a distribution with density $f(Y|\theta)$ for a (unknown but fixed) parameter θ. The likelihood function can be defined [33]:

$$L_n(\theta|X) = f_X(X|\theta) = \prod_{i=1}^{n} f_{X_i}(X_i|\theta), \tag{3.6}$$

which shows the joint density function of the samples. The log-likelihood function $l_n(\theta|X)$ is the natural logarithm of the likelihood function $L_n(\theta|X)$,

$$l_n(\theta|X) = \log L_n(\theta|X) = \sum_{i=1}^{n} \log f_{X_i}(X_i|\theta). \tag{3.7}$$

Then, $\hat{\theta}_{ml}$ that maximizes the likelihood function by using equation 3.6 or log-likelihood function by using equation 3.7:

$$\hat{\theta}_{ml} = \arg\max_{\theta} l(\theta|X). \tag{3.8}$$

To maximize the likelihood function,

$$S_{(\theta|Y)} = \frac{\partial l_n(\theta|X)}{\partial \theta} = 0. \tag{3.9}$$

However, analytical solution of the likelihood equations (equations 3.6 and 3.7) are not always available. In this case, Nelder-Mead optimization would be used to solve the equa-

tions which is explained in Appendix B. All of the mentioned concepts are prerequisites before starting statistical analyzing in the reverberation chamber.

3.2 Generalized Extreme Value Distribution and Fisher–Tippett Theorem

Suppose $X_1, X_2, ..., X_n$ are independent and identically-distributed random variables. If $M_n = max\{X_1, X_2, ..., X_n\}$ and a sequence of pairs of real numbers (a_n, b_n) exists such that

$$\lim_{x \to \infty} P(\frac{M_n - b_n}{a_n} \leq x) = F(x), \tag{3.10}$$

and each $a_n > 0$, where F is a non degenerate distribution, the limit distribution F converges to one of the following distributions, either the Gumbel, the Fréchet or the reverse Weibull family. These can be grouped into the generalized extreme value distribution by using Fisher–Tippett theorem [34]:

$$F_1(x) = \exp\left[-\exp\left(\frac{-x-m}{s}\right)\right], \quad \text{for all } x, \quad Gumbel \tag{3.11}$$

$$F_2(x) = \begin{cases} \exp\left[-\frac{(x-m)}{s}\right]^k, & \text{if } x > m \\ 0, & \text{otherwise} \end{cases} \quad Fréchet \tag{3.12}$$

$$F_3(x) = \begin{cases} \exp\left[-\frac{m-x}{s}\right]^k, & \text{if } x \leq m \\ 1, & \text{otherwise} \end{cases} \quad r. \ Weibull \tag{3.13}$$

where m, s and k represent location, scale and shape parameters, $-\infty < x < \infty$ for $k = 0$, $m + \frac{s}{k} \leq x < +\infty$ for $k > 0$ and for $k < 0$, $-\infty < x \leq m + \frac{s}{k}$. The corresponding probability density function (PDF) is [34] :
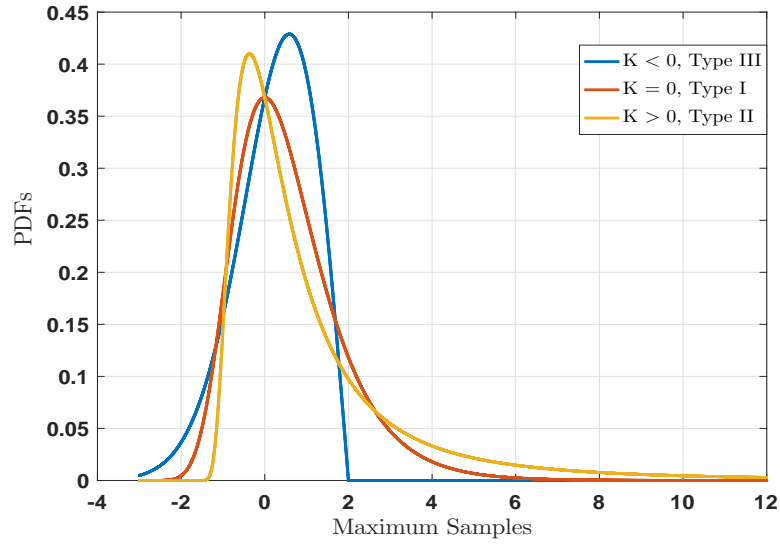
Figure 3.1: Three different distributions: Gumbel, Fréchet, r. Weibull.

$$
f(x) = \begin{cases} -\dfrac{1}{s}\left(1 + k\dfrac{(x-m)}{s}^{\left(-\frac{1}{k}\right)-1}\right)\exp\left[-\left(1 + k\dfrac{(x-m)}{s}\right)^{-\frac{1}{k}}\right], & \text{if } k \neq 0 \\[3ex] \dfrac{1}{s}\exp\left[-\exp\left(-\dfrac{(x-m)}{s}\right)\right], & \text{if } k = 0 \end{cases} \tag{3.14}
$$

when $k > 0$, $x > \frac{-1}{k}$, when $k < 0$, $x < -\frac{1}{k}$. In the case $k = 0$ the density is positive on the whole real line. Figure 3.1 shows three different distributions.

These three distributions can all reformulate to one distribution, which has the following Cumulative distribution function (CDF) [35] :

$$
F(x) = \begin{cases} \exp\left\{-\left[1 + k\left(\dfrac{x-m}{s}\right)\right]^{-\frac{1}{k}}\right\}, & \text{if } k \neq 0 \\[3ex] \exp\left[-\exp\left(\dfrac{x-m}{s}\right)\right], & \text{if } k = 0 \end{cases} \tag{3.15}
$$

The role of the extreme value theorem for maximum samples is similar to that of central limit theorem for averages. The only difference is that the central limit theorem applies to

30

the average of a sample from any distribution with finite variance, but the Fisher-Tippet theorem only applies if the distribution of a maximum converges and the limit has to be one of a particular class of distributions [30]. Location parameter shows the shifting in the distribution and is related to the location of function on the x-axis, while scale parameter determines statistical dispersion (stretching or shrinking) of probability distribution. Since the shape parameter (k) can vary from positive value to zero or below zero, GEV distribution can be defined as a family distribution [34]. Notably, The GEV distribution is not a symmetric distribution since the skewness (third order centered moment) is not zero as shown in Figure 3.2. Notably, red line shows location of mean value in all cases.

The tail of these three distributions will change due to the shape parameter. The distribution is Gumbel with $k = 0$, Fréchet with $k > 0$ and reverse Weibull (with three parameters) $k < 0$. The distributions with exponential decreasing tail lead to Gumbel; the distributions with polynomial decreasing tails (fat tail) lead to Fréchet; and the ones with finite tail lead to reverse Weibull distribution [34]. Figure 3.3 shows the thin, normal and fat tail distributions. The fat tail means if the probability of extreme value is particularly high, the CDF converges slowly to asymptotic value of 1. Kurtosis (4th order centered moment) is one way to show how distribution's tail changes. Westfall defined in [6] that "higher kurtosis means more of the variance is the result of infrequent extreme deviations, as opposed to frequent modestly sized deviations." In the other words, this method compares the tail of the distribution with Gaussian distribution. If the tail is heavier than Gaussian, Kurtosis will be higher than 3 [36].

3.3 Results and Analysis

In this section, the application of GEV distribution are shown in the nested cavity in over-moded regime. This application would help to better analyze the GEV distribution when the small box has the various apertures. The measurement were performed in the nested chamber. The sample EUT is fabricated from Aluminum with a rectangular shape
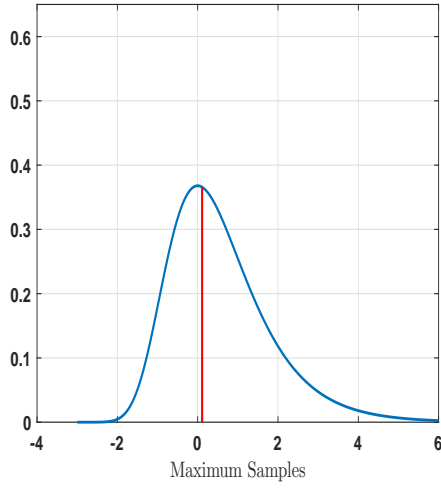
(a) Gumbel distribution.
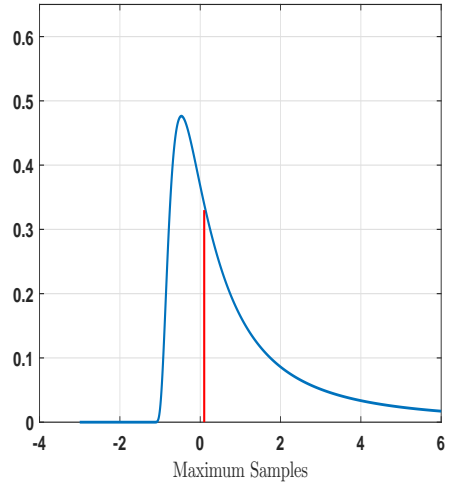
(b) Fréchet distribution.
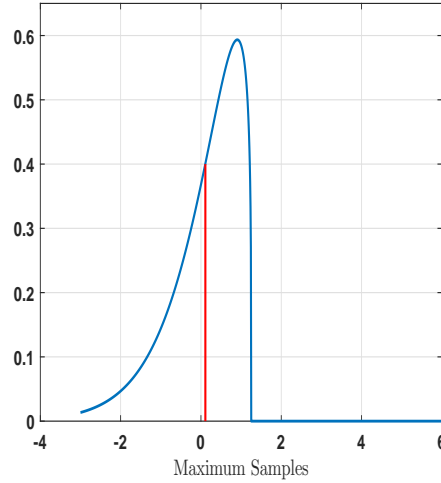
(c) r. Weibull distribution.

Figure 3.2: Density function for Gumbel, Fréchet and r. Weibull distributions. Red line shows location of mean value.

with the dimension of 30 cm $\times$ 30 cm $\times$ 12 cm. The wire probe is 10.4 cm in length with a radius of 0.41 mm. Figure 3.4 shows the apertures shape and table 3.1 shows the dimension of the apertures.

The probe is fed to the wall of the enclosure by applying the N-type connector. The small enclosure was located on the styrofoam inside the rectangular chamber with the in-
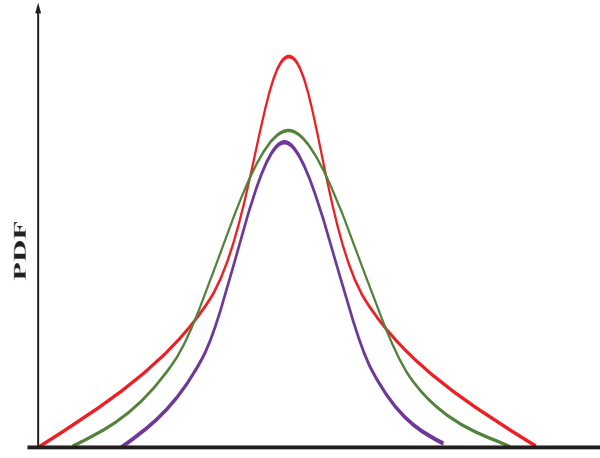
Figure 3.3: Kurtosis results (purple line shows thin tail distribution, green line shows normal distribution and red line shows heavy tail distribution [6].

Table 3.1: Dimension of Apertures

Aperture	**dimension** (*cm*)
AP1	15×6
AP2	5×3
AP3	4×2 (2 apertures)
AP4	15×1
AP5	2×2
AP6	30×12

| (a) AP 1. | (b) AP 2. | (c) AP 3. | (d) AP 4. |

| (e) AP 5. | (f) AP 6. |
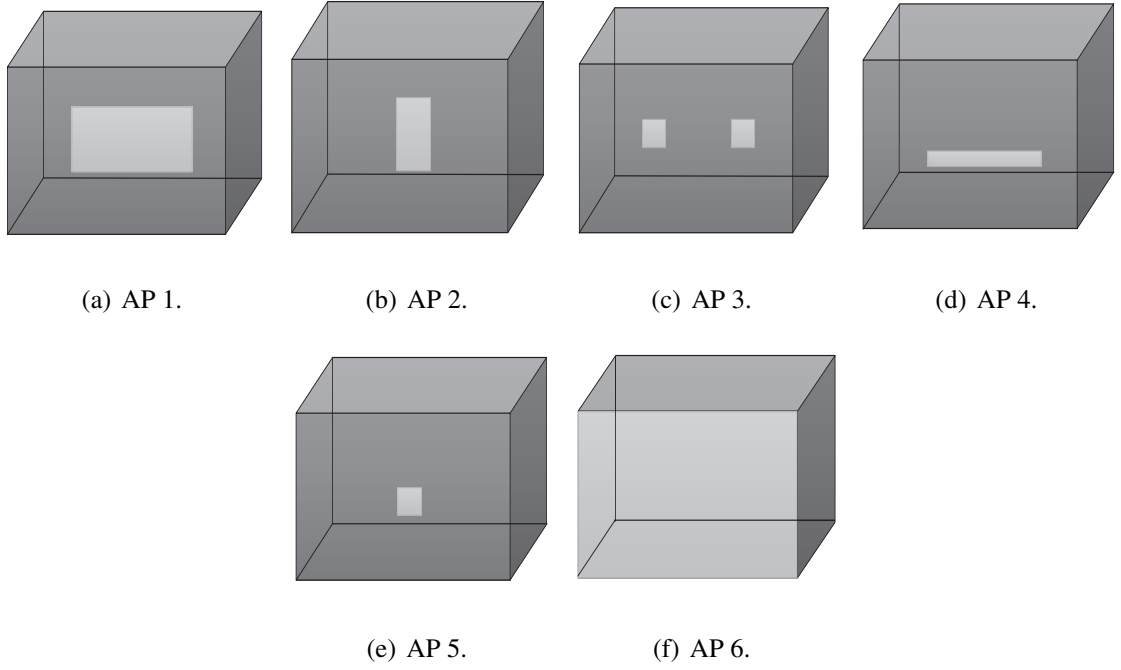
Figure 3.4: Aperture shapes.

ternal dimensions of 13.2 m × 6.15 m × 4.95 m whose dimensions are based on the ETS-Lindgren SMART-80 reverberation chamber. For a rectangular cavity, where dimensions $c > a > b$, the dominant resonant mode resonant in TE110 can be derived:

$$f_{mnp} = \frac{1}{2\sqrt{(\mu\varepsilon)}}\sqrt{(\frac{m}{a})^2 + (\frac{n}{b})^2 + (\frac{p}{c})^2}. \tag{3.16}$$

Figure 3.5 shows the resonant modes inside the small box. The TE110 = 707 MHz is the first dominant mode and three times of that gives the optimistic frequency that the cavity is in over-moded regime, which is around 2.7 GHz. The SMART-80 walls is fabricated from galvanized steel, producing a highly conductive reflective surface. The chamber has two tuners, vertical and horizontal, manufactured from steel. The two tuners can stir the field inside the chamber mechanically and create an isotropic, uniform field. Figure 3.6 shows the top view of the probe's location. Figure 3.7 shows the measurement set-up. The small box was covered with different aperture shapes and sizes. The aperture sizes are as follows, 15 cm by 6 cm, 2 small apertures with dimension 2 cm × 4 cm, 3 cm × 5 cm, 15 cm × 1
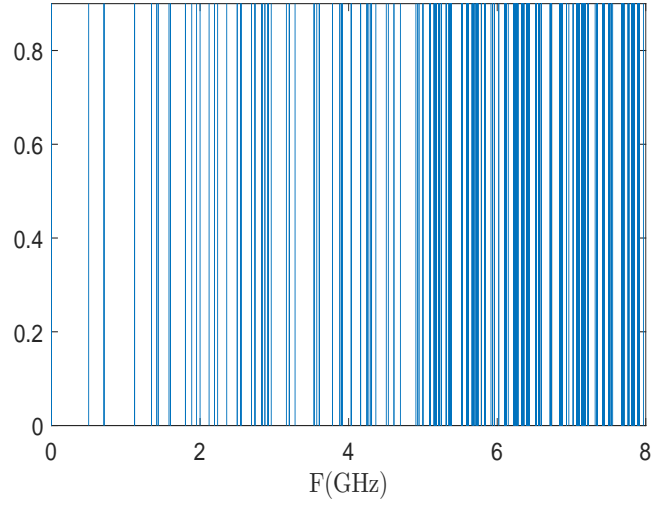
Figure 3.5: Mode positions for $30 \times 30 \times 12$ cm cavity up to 8 GHz.

cm, 2 cm $\times$ 2 cm, and 30 cm $\times$ 12 cm.

To have the uncorrelated samples in the frequency stirring:

$$\delta f > \frac{Q}{f_0}, \tag{3.17}$$

where Q, f_0 represent respectively quality factor and center frequency; the fraction of them shows coherence bandwidth, which shows the maximum bandwidth that data are dependent. we need to make sure δf will be larger than the coherence bandwidth. For the VNA measurement system, the calibration is performed immediately before the measurement, and all calibration information (magnitude and phase of both the transmission characteristics and the reflection characteristics) is used to correct for imperfections in the instrumentation and equipment. The measured frequency range was 5 to 5.1 GHz due to equation 3.17. The vertical tuner was rotated during the measurements to yield 50 random independent samples in each fixed probe positions, while the horizontal tuner was held stationary throughout the measurements. We measured 100 samples in 100 MHz frequency band to make sure δf is much greater than the coherence bandwidth. Then, we changed the probe location and

35
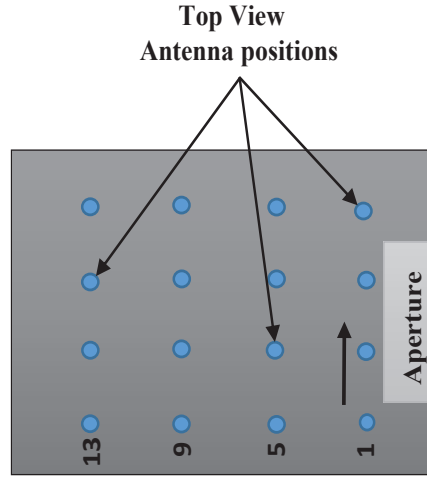
Figure 3.6: Antenna positions inside the enclosure.

re-performed the measurements till 16*th* probe location.

Notably, registration marks are used on the styrofoam block to keep the box at the same position and orientation in all sixteen measurements with each aperture. The 15 unused probe-location holes were covered with conducting tape during each measurement to prevent additional, unwanted coupling between the internal and external environments.

3.3.1 Statistical Analysis with External Stirring

Hill in [19] is shown the square magnitude of any electric field component is Rayleigh distribution (chi distributed with two degrees of freedom) in every frequency and it follows:

$$f_X(\lambda) = \frac{\lambda}{\theta} e^{\frac{-\lambda^2}{(2.\theta^2)}}, \tag{3.18}$$

where θ is scale parameter. Rayleigh distribution can compute by applying different Goodness-of-fit test such AD test and also by comparison between empirical CDF and mathematical model of CDF. The parameter of Rayleigh distribution can be defined by applying the concept of maximum likelihood in section 3.1.1. The estimated parameter $\hat{\theta}$ can be calculated:

36
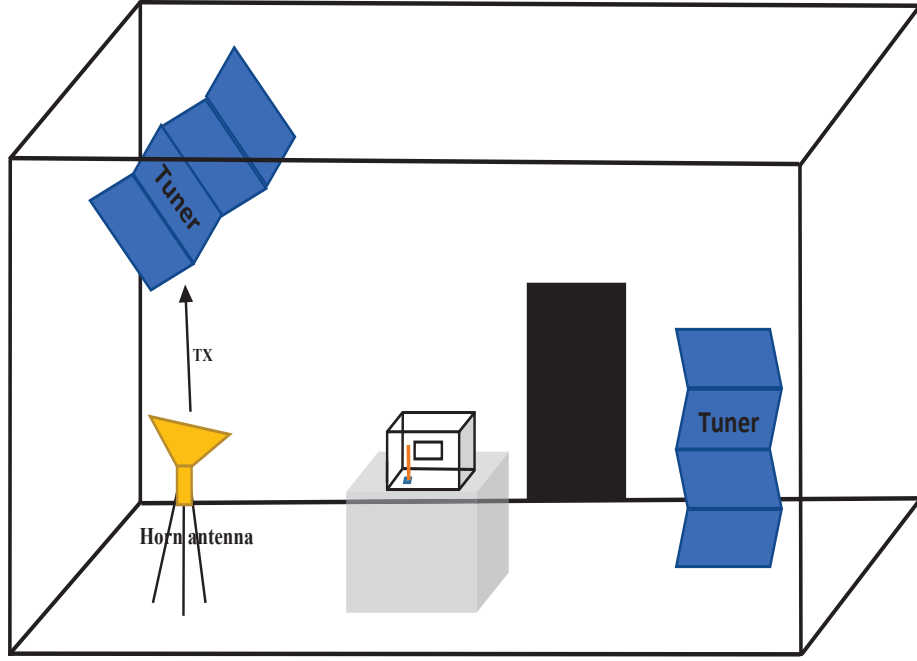
Figure 3.7: Measurement setup.

$$\hat{\theta} = \sqrt{(\frac{1}{2N}\sum_{i=1}^{N}x_i^2)}, \tag{3.19}$$

where $X_1,...,X_i$ shows the number of samples. The confidence interval is a type of interval estimate and consists of a range of values that act as good estimates of the unknown population parameter. The 95% confidence interval of the estimation is:

$$\hat{\theta} - 1.95\sigma_{\hat{\theta}} < \theta < \hat{\theta} + 1.95\sigma_{\hat{\theta}}. \tag{3.20}$$

Suppose i, j show respectively frequency step and the number of tuner positions. For every j there exist $|S_{21}|_i$ such that the frequency steps and tuner positions vary from $i = 1,...,100$ (number of tuner positions $j = 1,...,50$). Therefore, at each frequency step, for all $|S_{21}| \in j$ show a Rayleigh distribution [19]. The results of comparison between empirical and mathematical model of CDFs in 95% confidence interval is shown in Figure 3.8. As can be seen the empirical CDFs are inside the confidence interval. The AD test also performed

(a) CDF in AP 1.

(b) CDF in AP 2.

(c) CDF in AP 3.

(d) CDF in AP 4.

(e) CDF in AP 5.

(f) CDF in AP 6.
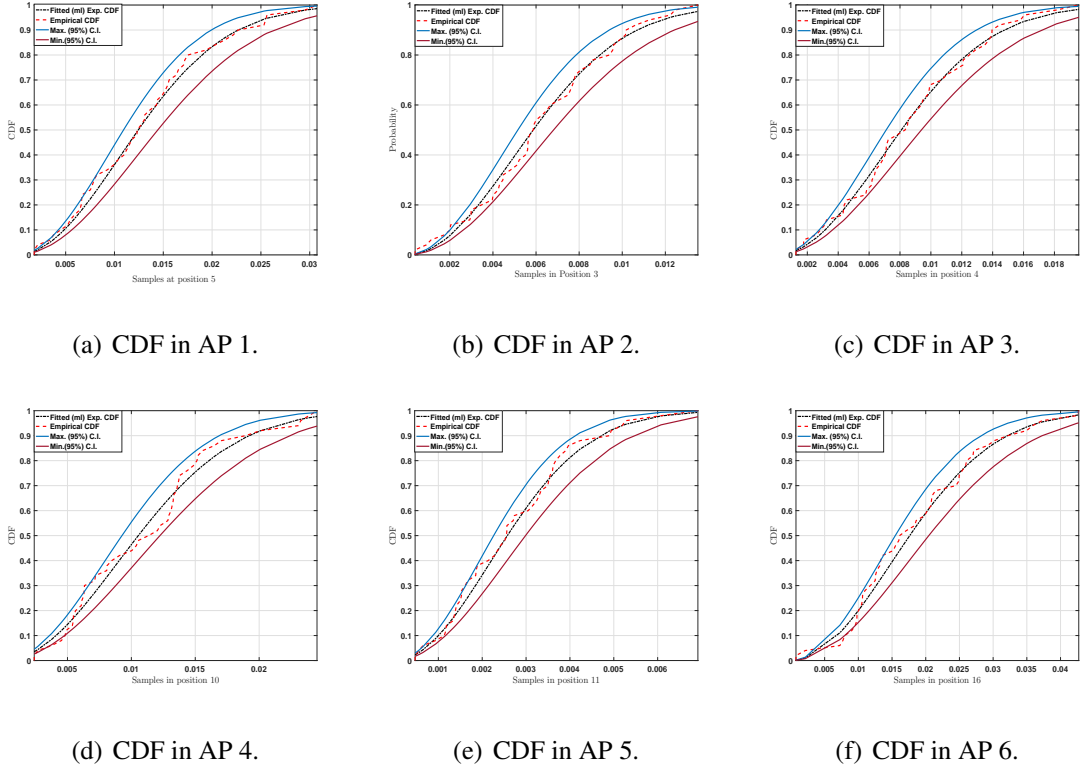
Figure 3.8: CDF in different aperture shapes in $f = 5$ GHz.

on the results in order to show the data have Rayleigh distribution in all frequencies.

The hypotheses for the AD-test are:

H_0: The data comes from a specified distribution.

As far as AD test is concerned initially, the parameter of the distribution needs to be estimated by applying maximum likelihood estimator which is shown in equation 3.19.

Then, the expression of the AD statistics (A^2) is defined [37]:

$$A^2 = \frac{\sum_{i=1}^{N}(2i-1)[ln(F(x_i)+ln(1-F(x_{N+1-i})))]}{N} - N, \qquad (3.21)$$

where $F(x_i)$ and N show respectively the estimated CDF and number of samples. Critical values and p-values formula to be compared with A^2, depend on the type of distribution tested. Critical values and p-values formula for the modified statistic $A^2(1+(\frac{0.6}{N}))$ are presented for the Rayleigh case in [37]. If the value of p-value exceeds the significant level (α), one accepts the hypothesis (H_0) that the observations are from a Rayleigh distribution. It

38
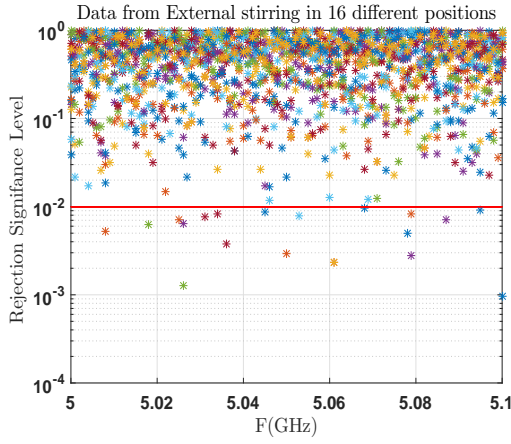
(a) AP 1.
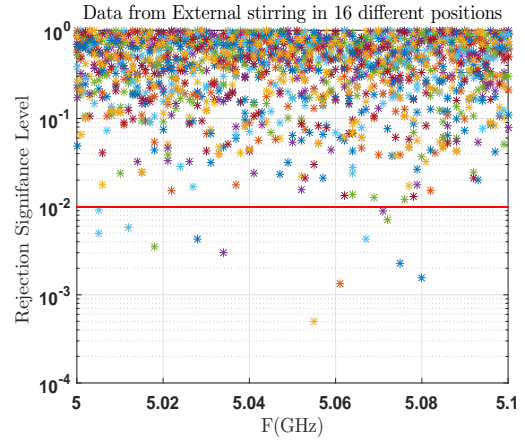
(b) AP 2.

Figure 3.9: AD test for 16 different probe locations for AP1 , AP2.
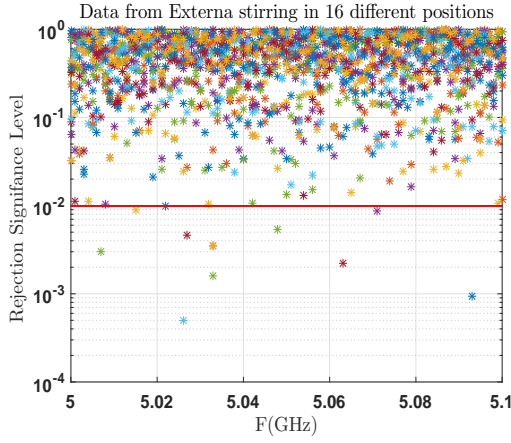
(a) AP 3.
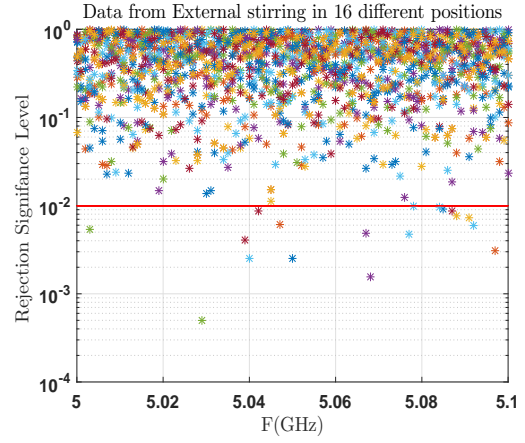
(b) AP 4.

Figure 3.10: AD test for 16 different probe locations for AP3 , AP4.

is important to mention that α is the threshold for p-value which the experimenter assumes the null hypothesis is false.

Figures 3.9(a) to 3.11(b) show the results with $\alpha = 1\%$ (red lines) in all apertures. 50 samples were collected at a single frequency for each test. Points below 0.01 indicate that the null hypothesis of magnitude samples following a Rayleigh distribution was rejected for that particular frequency and wire-probe positions at $\alpha = 1\%$ confidence level. It is important to mention the highest rejection rate belongs to the probe location in front of

(a) AP 5.

(b) AP 6.
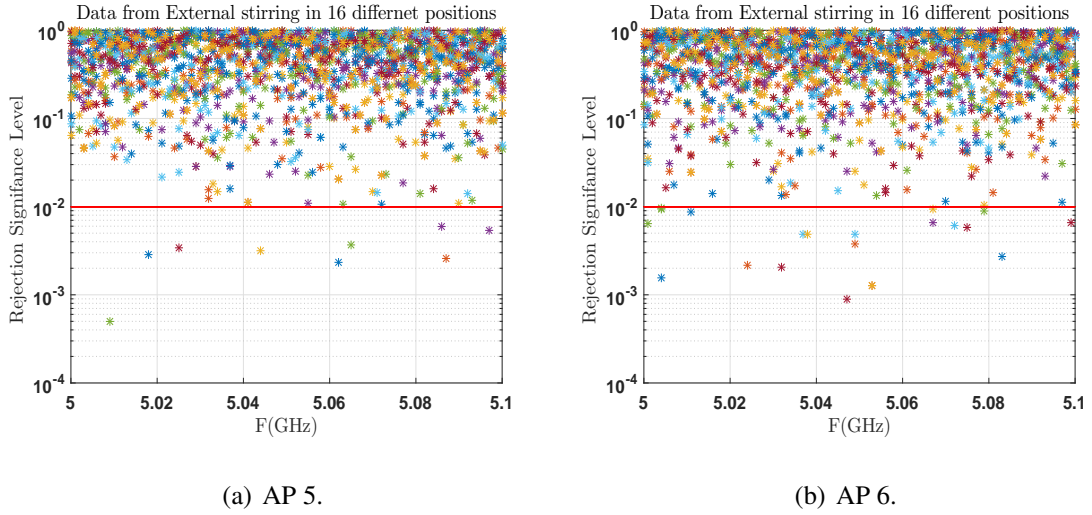
Figure 3.11: AD test for 16 different probe locations for AP5 , AP6.

the aperture. Overall, the null hypothesis was rejected about 2% in all cases of the time, slightly higher than the 1% that would be expected for ideally Rayleigh-distributed data in all cases. The slightly elevated rejection rate likely results because the chamber is not truly ideal [37].

3.3.2 The GEV Distribution for Maximum Field Level

A sample set of maximum values was prepared by extracting the maximum of each stir sequence subset:

$$x(i) = \{|S_{21}(1)_j|, ..., |S_{21}(i)_j|\}, \tag{3.22}$$

where $i = 1, ..., N$ and $j = 1, ..., 100$ show the tuner position and the number of frequency step. The set of maximum values is:

$$X(i) = \{max(x(i))\}. \tag{3.23}$$

The maximum S_{21} was chosen in each tuner position and the measurement repeated in the next probe position.

40

A dual-ridge horn antenna was located 1 meter far away from the enclosure aperture. The antenna is not delivering energy directly to the aperture and the enclosure will receive the illumination energy from the reverberant environment. The probe needs to be located inside the box λ away from the walls and other probe positions due to spatial correlation. However, the spatial sampling between each 50 sample maximums can be verified by computing the correlation coefficient.

The correlation coefficient between two random variables can define by using sections A.1.6 and 3.1 as:

$$\hat{r} = \frac{\sum\limits_{i=1}^{n} (x_i - \bar{x})(y_i - \bar{y})}{\sqrt{\sum\limits_{i=1}^{n} (x_i - \bar{x})^2} \sqrt{\sum\limits_{i=1}^{n} (y_i - \bar{y})^2}}, \tag{3.24}$$

where the nominator shows the estimated covariance between two random variables,

$$\bar{x} = \frac{1}{n} \sum_{i=1}^{n} x_i, \tag{3.25}$$

and

$$\bar{y} = \frac{1}{n} \sum_{i=1}^{n} y_i. \tag{3.26}$$

For the set of samples $X_1, X_2, ..., X_n$ that are independent and identically distributed, the log-likelihood function for the set computes using section 3.1:

$$\ln[(l(\theta|x)] = -m \ln(s) - \sum_{i=1}^{N} \left[\left(\frac{1}{k} + 1 \right) \ln(y_i) + y_i^{\left(-\frac{1}{k} \right)} \right], \tag{3.27}$$

where $\theta = (m, s, k)$ and $y_i = [1 + k(\frac{x-m}{s})]$. The estimated parameters $\hat{\theta} = (\hat{m}, \hat{s}, \hat{k})$ can be found by using Nelder-Mead optimization in order to find the global maximum for each parameter, which correspond to setting zero the first derivatives of equation 3.6.

41

The 800 sample maximums were collected during each measurement from AP1 to AP6 and the results are shown as follows.

3.3.2.1 AP1 Results

Parameters	$\hat{k}$	$\hat{s}$	$\hat{m}$
$\hat{\theta}$	-0.0728	0.1448	1.1669
C.I. (95%)	-0.1142	0.1373	1.1559
	-0.0313	0.1528	1.1780
$\sigma_{\hat{k}}^2$	$4.477e-4$	$1.558e-5$	$3.188e-5$

Table 3.2: Estimated parameters in AP1 case

Figure 3.12: CDFs.

(a) Empirical Histograms and parametric PDFs.

(b) The correlation between samples in the different positions.

Figure 3.13: Parametric and non-parametric PDFs and the correlation between the samples for AP1 case.

Tables 3.2 to 3.7 show the estimated parameters $(\hat{k}, \hat{s}, \hat{\mu})$, parameters in the 95% confidence intervals, and the asymptotic variances by using maximum likelihood estimator.

In AP1 to AP6 except AP5, $\hat{k} < 0$ which shows that the data follows the r. Weibull distribution. However, the values of $\hat{k}$ in 95% confidence interval (C.I.) in AP4 starts with negative value and stops at positive value which shows the data follows upper bounded and unbounded distributions.

3.3.2.2 AP2 Results

Parameters	$\hat{k}$	$\hat{s}$	$\hat{m}$
$\hat{\theta}$	-0.0988	0.1147	0.6795
C.I. (95%)	-0.1364	0.1088	0.6708
	-0.0611	0.1210	0.6882
$\sigma_{\hat{k}}^2$	$3.696e-4$	$9.6424e-6$	$1.973e-5$

Table 3.3: Estimated parameters in AP2 case
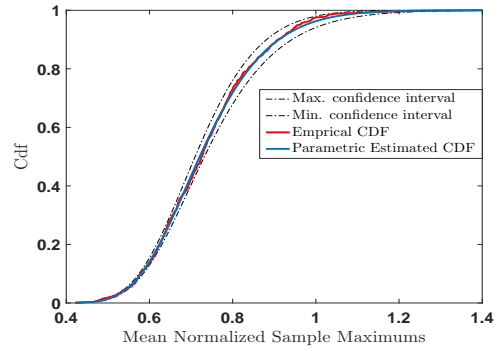
Figure 3.14: CDFs.
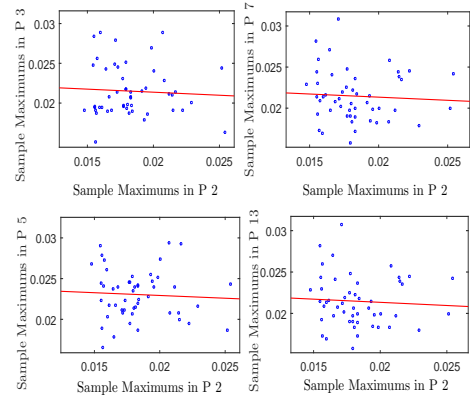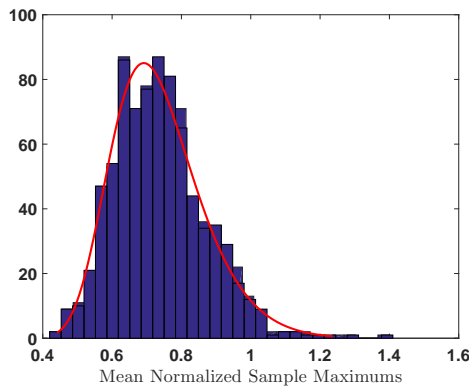
(a) Empirical Histograms and parametric PDFs.

(b) The correlation between samples in the different positions.

Figure 3.15: Parametric and non-parametric PDFs and the correlation between the samples for AP2 case.

This means that the estimated parameters in confidence interval include the Gumbel

distribution, which align with the traditional distribution that is used in over-moded regime of the chamber theory [5]. The results for AP5 follow the Fréchet distribution. This may indicate the other apertures are providing a direct coupling path from the outer cavity to certain probe locations which is effecting the uniformity of the inner cavity.

3.3.2.3 AP3 Results

Parameters	$\hat{k}$	$\hat{s}$	$\hat{m}$
$\hat{\theta}$	-0.0362	0.1247	0.8197
C.I. (95%)	-0.0846	0.1179	0.8101
	-0.0122	0.1318	0.8294
$\sigma_{\hat{k}}^2$	$6.099e-4$	$1.253e-5$	$2.435e-5$

Table 3.4: Estimated parameters in AP3 case
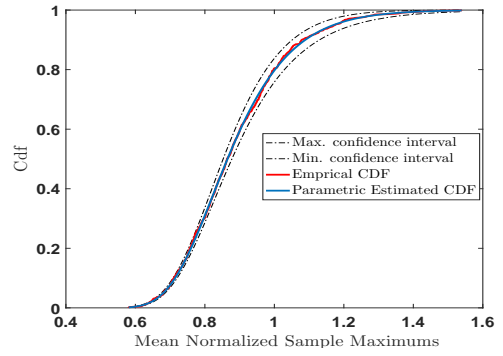
Figure 3.16: CDFs.
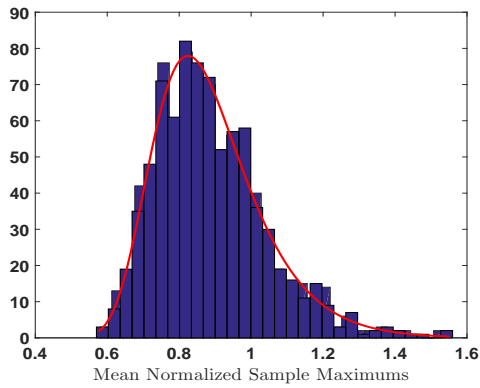
(a) Empirical Histograms and parametric PDFs.
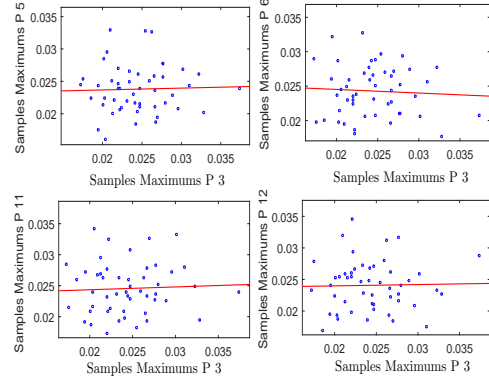
(b) The correlation between samples in the different positions.

Figure 3.17: Parametric and non-parametric PDFs and the correlation between the samples for AP3 case.

Possibly the smaller apertures are limiting the direct path component and hence we see

a more uniform field in the inner cavity. In addition, it seems that the variance of estimated parameters are quite small, especially for k parameter. This means that the k parameter has less spread in the confidence interval, which is important in showing the type of GEV distribution.

3.3.2.4 AP4 Results

Parameters	$\hat{k}$	$\hat{s}$	$\hat{m}$
$\hat{\theta}$	-0.0950	0.1475	0.9864
C.I. (95%)	-0.1396	0.1398	0.9751
	-0.0505	0.1556	0.9977
$\sigma_{\hat{k}}^2$	$0.5164e-3$	$0.0164e-3$	$0.0334e-3$

Table 3.5: Estimated parameters in AP4 case
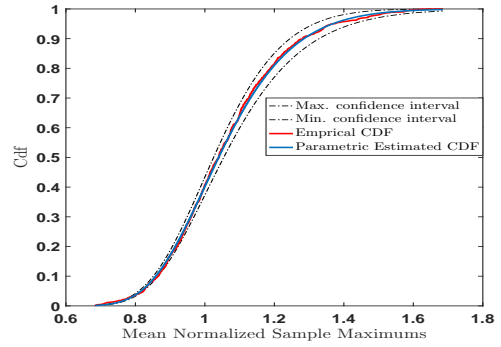
Figure 3.18: CDFs.
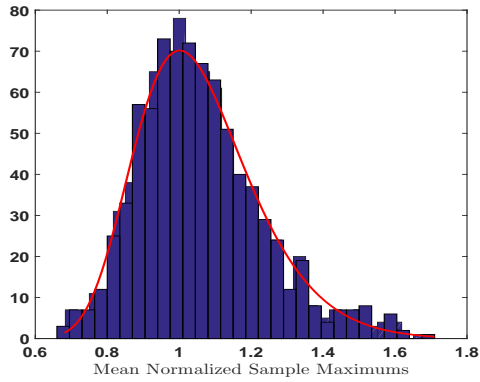
(a) Empirical Histograms and parametric PDFs.
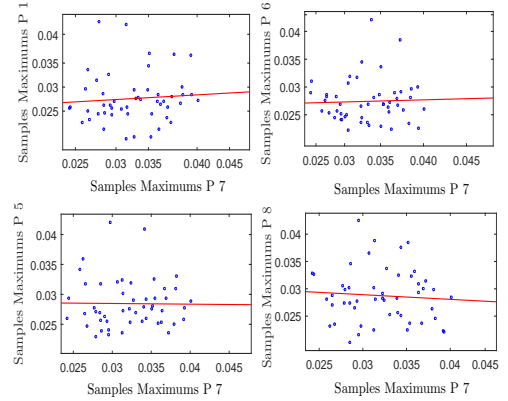
(b) The correlation between samples in the different positions.

Figure 3.19: Parametric and non-parametric PDFs and the correlation between the samples for AP4 case.

Figures 3.12, 3.14, 3.16, 3.18, 3.20, and 3.22 show empirical and parametric CDFs

based on estimated parameters ($\hat{\theta}$) from maximum likelihood estimator for all aperture dimensions. On these plots we can see that the empirical CDFs are in 95% confidence interval by using equation 3.20. The results show a high quality agreement between the mathematical model and empirical result.

3.3.2.5 AP5 Results

Parameters	$\hat{k}$	$\hat{s}$	$\hat{m}$
$\hat{\theta}$	0.0214	0.2315	0.8601
C.I. (95%)	-0.0434	0.2179	0.8414
	0.0861	0.2460	0.8610
$\sigma_{\hat{k}}^2$	$3.672E-4$	$2.7315e-5$	$5.7926e-5$

Table 3.6: Estimated parameters in AP5 case
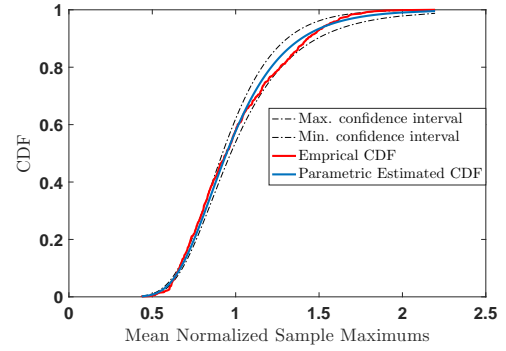
Figure 3.20: CDFs.
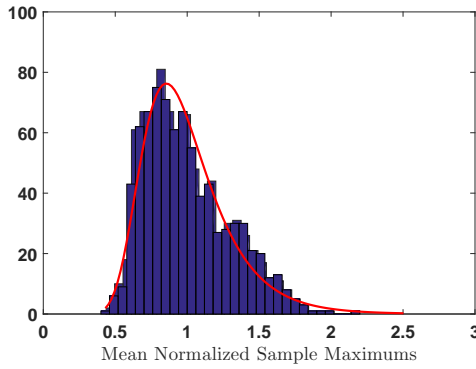
(a) Empirical Histograms and parametric PDFs.
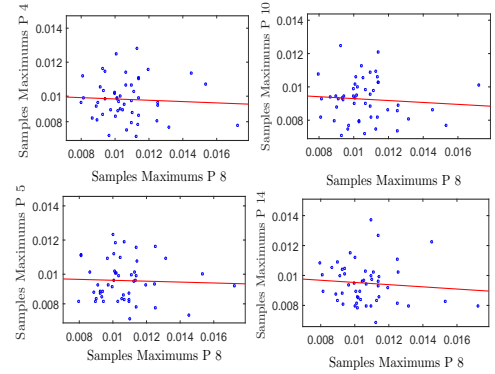
(b) The correlation between samples in the different positions.

Figure 3.21: Parametric and non-parametric PDFs and the correlation between the samples for AP5 case.

The maximum samples S_{21} can be binned to a histogram, for comparison with the ideal GEV distribution. Figures 3.13(a), 3.15(a), 3.17(a), 3.19(a), 3.21(a) and 3.23(a) show

46

histogram of GEV distribution (empirical) with arbitrary bin widths and red line shows the parametric estimated PDFs by using each aperture dimension. As can be seen there is a good quality of agreement between the red line and the blue bins.

3.3.2.6 AP6 Results

Parameters	$\hat{k}$	$\hat{s}$	$\hat{m}$
$\hat{\theta}$	-0.1442	0.1971	1.5087
C.I. (95%)	-0.1817	0.1871	1.4938
	-0.1066	0.2076	1.5236
$\sigma_{\hat{k}}^2$	$3.672e-4$	$2.7315e-5$	$5.7926e-5$

Table 3.7: Estimated parameters in AP6 case
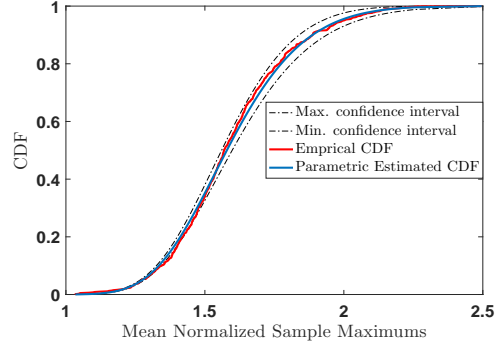
Figure 3.22: CDFs.
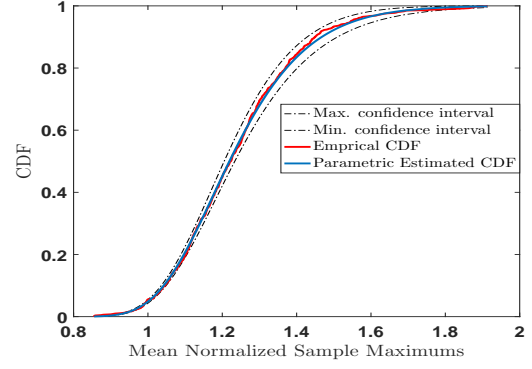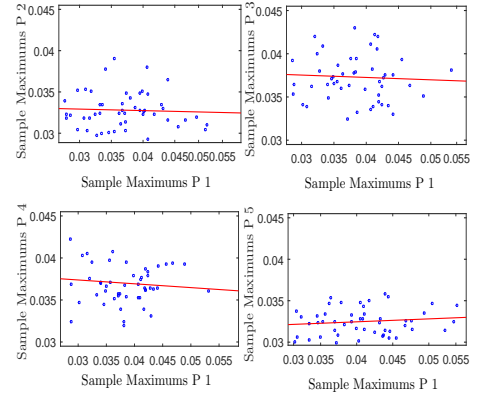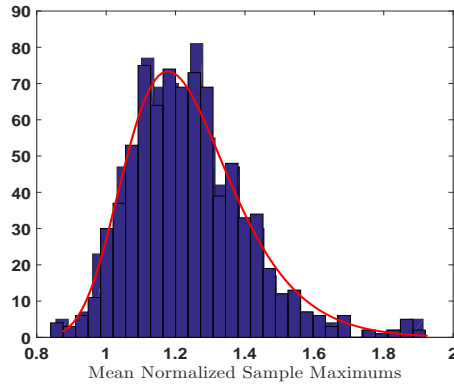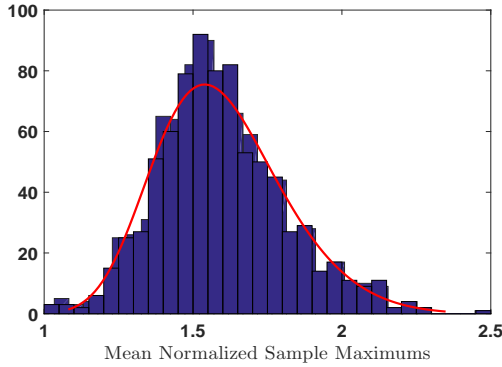

(a) Empirical Histograms and parametric PDFs.
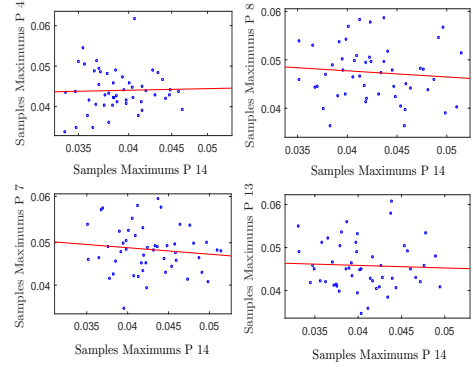
(b) The correlation between samples in the different positions.

Figure 3.23: Parametric and non-parametric PDFs and the correlation between the samples for AP6 case.

The position of the probe was chosen by using spatial correlation. However, the 50 maximum samples S_{21} from each position need to be verified from 50 maximum samples S_{21}

on the other positions. Figures 3.13(b), 3.15(b), 3.17(b), 3.19(b), 3.21(b) and 3.23(b) show the correlation between one probe location with other probe locations by using equation 3.24. As can be seen the samples from different locations are uncorrelated.

The comparison between PDFs and CDFs of all apertures dimension are shown in figures 3.24(a), 3.24(b) and 3.24(c). As can be seen, the PDFs from the different apertures have different parameters. Between all scenarios only AP5 follows Fréchet distribution which has an upper heavy tail. It seems that the small aperture can affect significantly on GEV distribution parameters due to separation of the environment inside and outside the box [3].

On these plots, it can be seen that the variance of the maximums are dependent on the aperture dimension. When the aperture is small (AP5), the variance of the maximums is lower due to independency of the environment inside and outside the box. This results more uniform environment inside the box. When the aperture is large (AP1 and AP6), the environments inside and outside the box are dependent on each other and the variance is larger than the other cases. In addition, when the aperture is large, more energy goes inside the box (AP6 and AP1) and the mean has a larger value compared to other cases. While in the small aperture dimension such as AP5 case, less energy goes inside the box and the mean is smaller than the other cases.

3.3.3   Analysing Data in Each Probe Location

In this section, we present the comparison between the maximum data in each of the probe's locations.

Suppose i, j represent the number of tuner positions and probe locations respectively. If $j = 1, ..., 50$ for every i and $i = 1, ..., 16$, the sample maximums in each probe location can be defined as:

$$P_i = X_j(i). \tag{3.28}$$
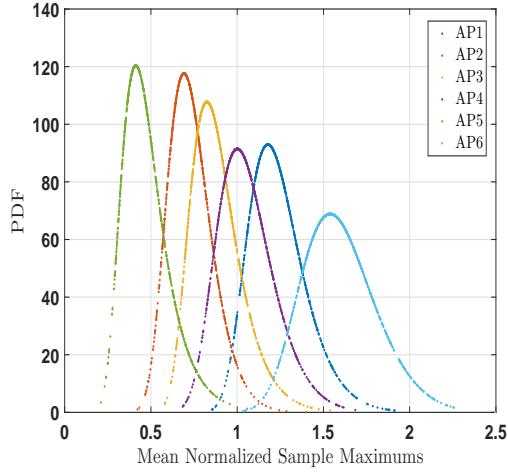
(a) PDFs.
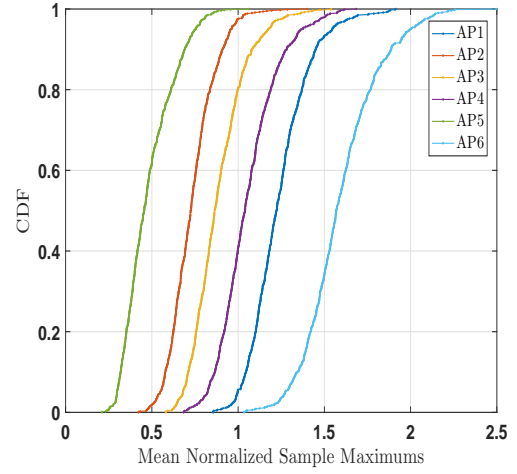
(b) CDFs.
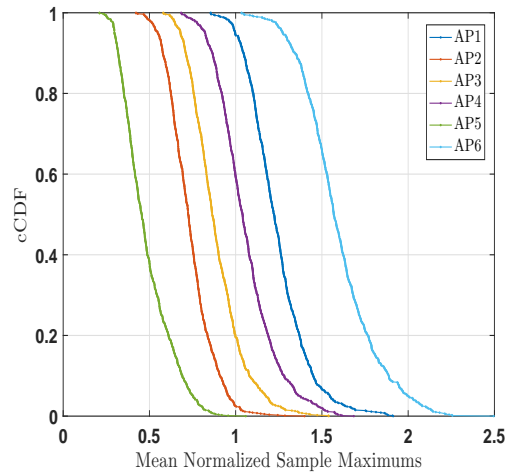
(c) cCDFs.

Figure 3.24: Comparison between different apertures.
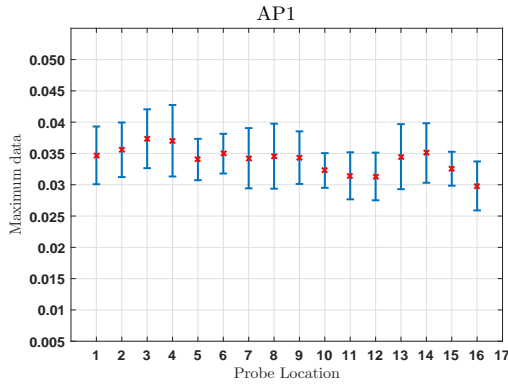
(a) Mean and variance of maximums.
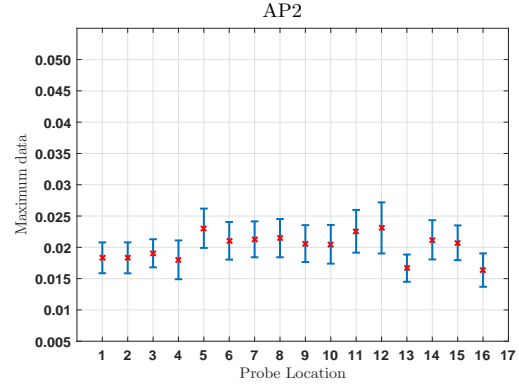
(b) Mean and variance of maximums.

Figure 3.25: Mean and variance of maximum samples for AP1 (left), AP2 (right).
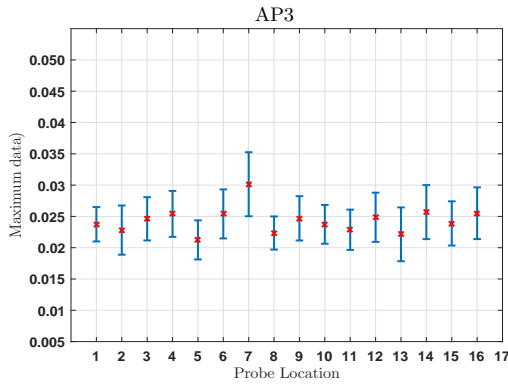
(a) Mean and variance of maximums.
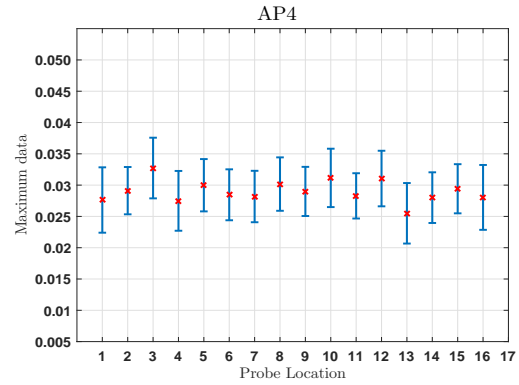
(b) Mean and variance of maximums.

Figure 3.26: Mean and variance of maximum samples for AP3 (left), AP4 (right).

The mean and the variance of all 50 sample maximums in each probe positions are calculated to analyze the variation. Figures 3.25(a) to 3.27(b) shows the results for each aperture size. The mean and the variance of every P_i which are in front of the aperture in AP5, are lower than the other apertures since the aperture dimension is really small and the lower amount of energy can go through the aperture inside the box. It seems that the normal reverberant environment has less effects on the environment inside the box, when AP5 is used on the front face of the box. However, the mean and the variance of AP1 and AP6 are larger than the others due to the aperture's dimension.
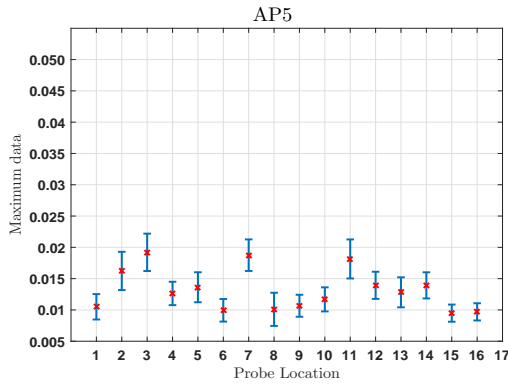
(a) Mean and variance of maximums.
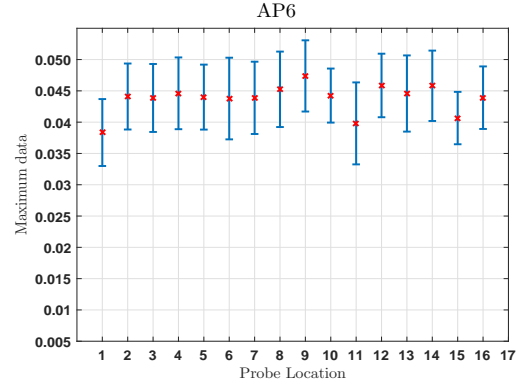
(b) Mean and variance of maximums.

Figure 3.27: Mean and variance of maximum samples for AP5 (left), AP6 (right).

3.3.4 Conclusion

Statistical models for maximum field level inside the complex cavities have historically been derived from the parent distributions and this results a maximum unbounded distribution that only works for over-moded cases. In this work, we introduced Fisher-Tippett Theorem and Generalized Extreme Value (GEV) distribution to model the maximum level of fields inside the enclosure directly. The purpose of this chapter was to show the GEV distribution can model the maximum of the field within a complex cavity in over-moded regime, when the various aperture dimensions were used. In this way, the tail of the distribution will change due to shape parameter (k). In addition, the effects of aperture dimension on the maximum distribution were shown. The results are of interest in study of electromagnetic complex cavities, and also immunity testing [38].

CHAPTER 4

APPLYING THE GENERALIZED EXTREME VALUE DISTRIBUTION INSIDE ELECTROMAGNETIC COMPLEX CAVITIES

The advantage of the GEV distribution is that it is not theoretically dependent on the parent distribution. Though demonstrated by [5], the applicability of the GEV distribution to model the maximum distribution while the parent distribution is unknown, requires experimental validation. In this chapter, the GEV distribution is applied directly to compute the maximum field level when the parent distribution is unknown. In section 4.1, apertures' dimensions, the measurement set up to collect data as Rayleigh distribution, and non-Rayleigh distribution are explained. In section 4.2, after discussing mechanical stirring (both external and internal stirrings) inside nested chamber, the GEV distribution is used to model the maximum distribution in different situations. In addition, statistical analysis is used to assess the shielding effectiveness uncertainty inside the nested chamber. [1]

4.1 Measurement Setup

4.1.1 Test Cavity

One of the conditions that the parent distribution is unknown can be defined as the field from the internal stirring inside the nested chamber, while front face of the EUT box is covered with several different aperture dimensions. In this section cavity dimension, aperture shapes and dimension and the transmitter and receiver antenna configurations are

---

[1]This chapter was presented under the title "Investigation of Electromagnetic Complex Cavities by Applying the Generalized Extreme Value Distribution", N. Nourshamsi, J.C. West, C.F. Bunting, IEEE EMC Symp., 2018 [39].

discussed. The rectangular enclosure's dimension is explained in chapter 3 and is known as equipment under test (EUT) as shown in Figure 4.1(a). The tuner was mounted 9 cm from the back wall of the enclosure (relative to the face with the aperture considered the front face) and 6.5 cm from the left side wall as shown in Figure 4.1(b). The tuner is 10 cm in height. The lower "arm" of the z-shape is 5 cm in length and the upper arm has 7.4 cm length as shown in Figure 4.1(c).

(a) Cavity dimension.

(b) Top view of probe and tuner position.

(c) Tuner dimension
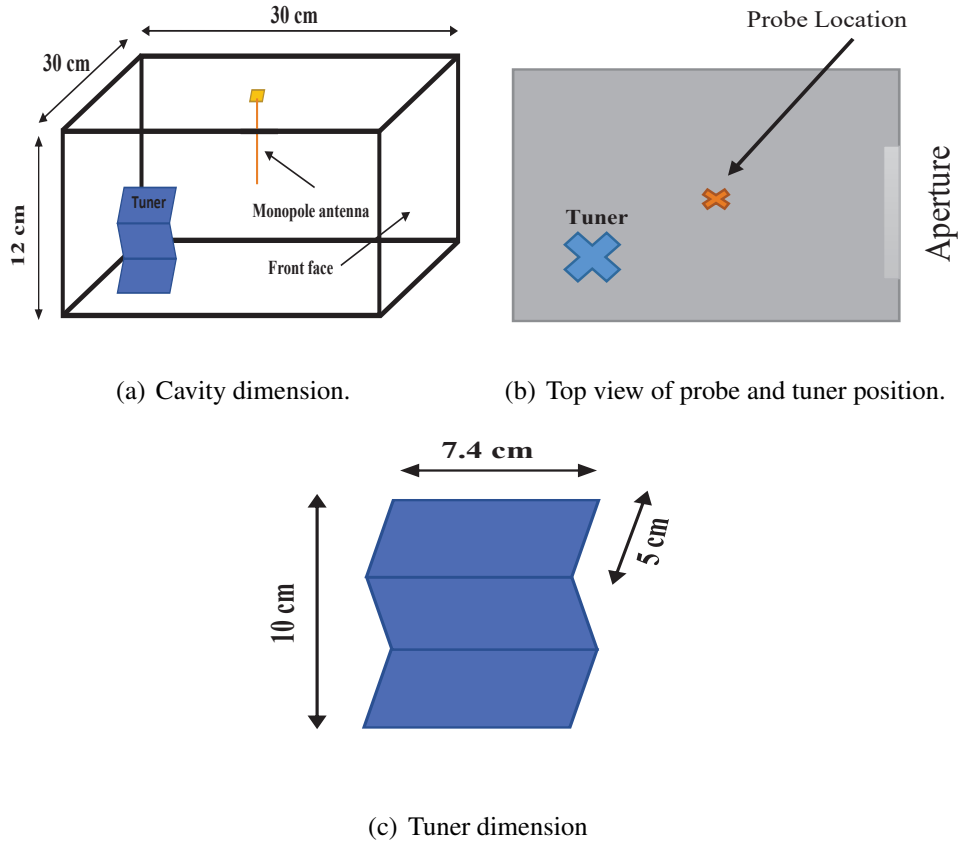
Figure 4.1: Cavity information.

The wire probe is 10.4 cm in length with a radius of 0.41 mm. An N-type connector is used to connect the probe to the wall of the enclosure. The probe is connected to the center of the box in front of the aperture as explained in chapter 3. The adapter to connect cable to antenna is shown in Figure 4.2 and probe antenna is shown in Figure 4.3. The small cavity is located within the working volume of a rectangular reverberation chamber (SMART-80 ETS-Lindgren) which has dimensions of 13.2 m × 6.15 m × 4.95 m. The

reverberation chamber walls are fabricated from galvanized steel in order to have highly conductive surfaces.
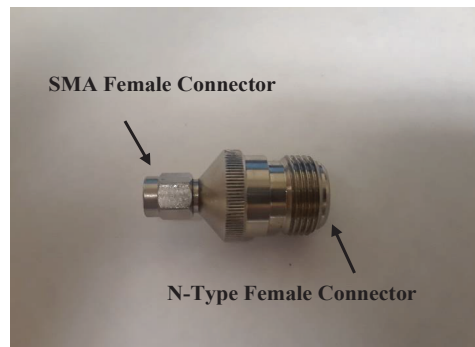
Figure 4.2: SMA female / N-type female adapter.

Figure 4.3: Monopole Antenna.
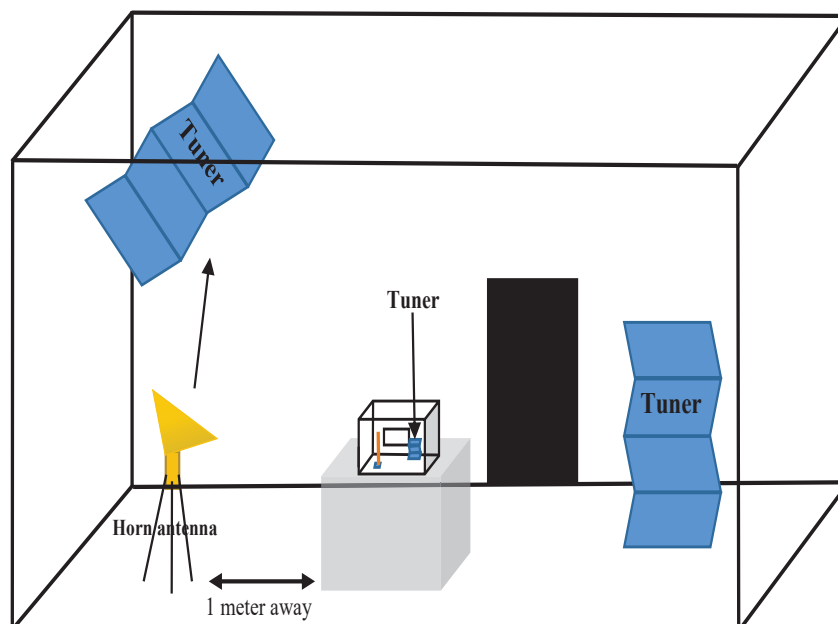
Figure 4.4: Measurement Setup inside SMART-80.

Table 4.1: Measurement Parameters

Parameter	Value
Frequency range	1 - 6 GHz
Number of frequency points	1601
VNA sweep time	8 Sec.
Paddle step size inside the SMART-80 (Only vertical)	7.2 °
Paddle step size (inside the EUT box)	7.2 °

The field inside the chamber was stirred with two tuners, one vertical and one horizontal, to produce a uniform and isotropic random field. For the purpose of the work in this research, only vertical tuner was rotated inside the chamber. A dual-ridge horn antenna used as transmitter antenna, 1 meter away from the box. The box placed on styrofoam block in order to be in working volume of the chamber. Figure 4.4 shows the location of the enclosure, tuners and antenna inside the reverberation chamber. Table 4.1 shows the measurement parameters. The small box includes covered with different aperture shapes and sizes which will be explain in next section.

4.1.2 Aperture Dimension

The "aperture" plates are fabricated from 5-gauge aluminum sheet metal, giving a thickness of approximate 0.01λ, where λ is the electromagnetic wavelength, at the highest test frequencies to be considered in this work, thereby minimizing the excitation of aperture resonances that may affect the electromagnetic measurements. Figure 4.5 shows aperture configurations and Table 4.2 shows the aperture sizes.

(a) AP1.   (b) AP2.

Figure 4.5: Apertures' dimensions and shapes.

Table 4.2: Dimension of Apertures

Aperture	**Dimension** (*cm*)
AP1	15×6
AP2	$Radius = 1.5$

4.1.3   Data Collection

The GEV distribution can model the maximum distribution directly. One way to validate this property is examining the field from internal stirring inside the nested chamber with several different aperture dimensions on the enclosure. For the VNA measurement system, calibration is performed immediately before the measurement, and all calibration information (magnitude and phase of both the transmission characteristics and the reflection characteristics) is used to correct for imperfections in the instrumentation and equipment. The data collection is proceed as follows:

1. The SMART-80 tuner will be set to one of 50 positions.

2. The EUT test box tuner will be set to one of 50 positions.

3. The S_{21} coupling between the dual ridge antenna and the test-box measurement probe will be collected from 1 GHz to 6 GHz over $1,601$ steps.

4. Steps 2 and 3 will be repeated until measurement at 50 test box tuner positions have been completed.

5. Step 1 through 3 will be repeated until measurement at 50 SMART-80 tuner positions has been completed.

4.2 Results and Analysis

4.2.1 Initial Statistical Analysis

The $2,550$ samples at each frequency step were collected during each measurement (external and internal stirring). There are two different situations in this scenario:

- Case 1: Fixed internal tuner position, rotating the external tuner positions.

- Case 2: Fixed external tuner position, rotating the internal tuner positions.
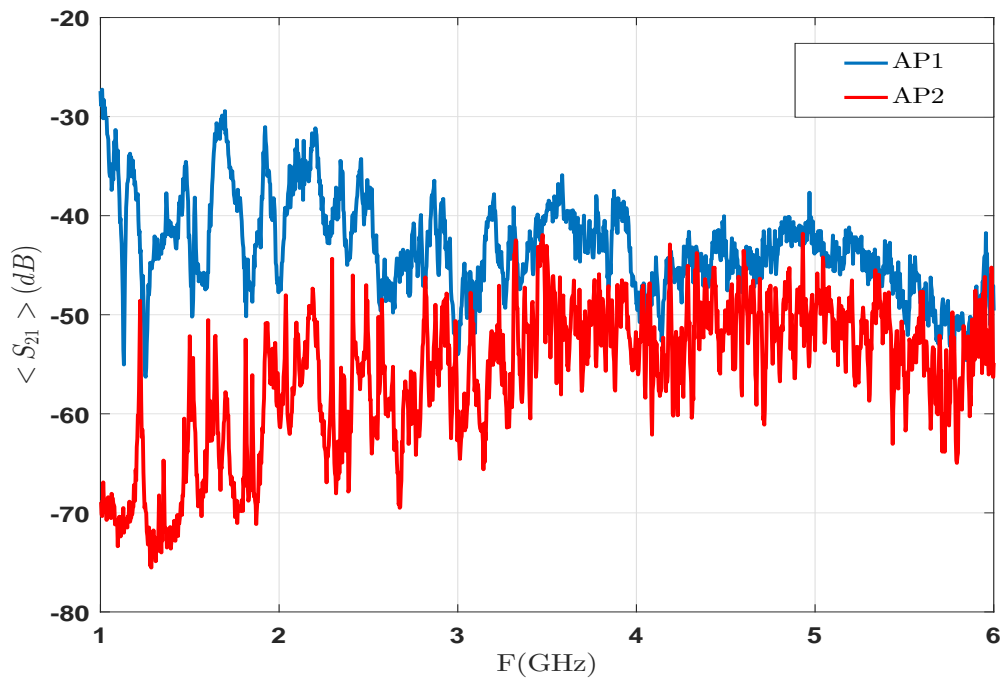
Figure 4.6: Average S_{21} over 50 tuner positions from external stirring (case 1) with AP1, AP2.

The Equations 4.1 and 4.2 show cases 1 and 2 mathematically.

$$x(e) = |S_{21}|_{i=1,....,50}\Big|_{e},\qquad(4.1)$$

$$x(i) = |S_{21}|_i\Big|_{e=1....50},\qquad(4.2)$$

where e and i show external, internal tuner positions respectively.

Figures 4.6 shows the average S_{21} (the transmission response) over 50 external tuner positions with AP1 and AP2. Additionally, it seems varying aperture shapes and dimensions change the strengths and frequencies of the resonant responses. This can be seen at low frequencies where the widths and strengths of the first resonance happen at 1.12 GHz in AP1 and at 1.25 GHz in AP2. Notably, the mean of Rayleigh distribution is changed in each frequency step, which is explained in detail in [40]. This means that there is a Rayleigh distribution with a specific mean at each frequency step.

The overall behavior in two different apertures indicate that there are strong resonances at the low frequencies. This happens since the largest apertures dimension is smaller than a wavelength below 2 GHz in both cases. Additionally, as frequency increases resonant frequencies ratios (from pick to null) decrease, specially above 4 GHz due to the aperture dimensions (more clear in AP1 case). This means that the largest apertures dimension in both scenarios (AP1 and AP2) is larger than a wavelength above 4 GHz, allowing energy go inside the EUT enclosure easily.

Figure 4.7 shows the resonant reflection responses of the wire probe (average S_{22} over 50 external tuner positions) in the environment of the test enclosure while the front face is covered with AP1 and AP2. This can be useful to understand the behavior of the straight probe while the EUT box is covered with different apertures (effects of aperture resonance on the wire probe). As can be seen more strong resonances exist around 5 GHz in both cases. Figure 4.8 shows average S_{11} (reflection response of transmitter antenna) over 50 external tuner positions. As indicated, the resonant frequencies are the same for transmitter
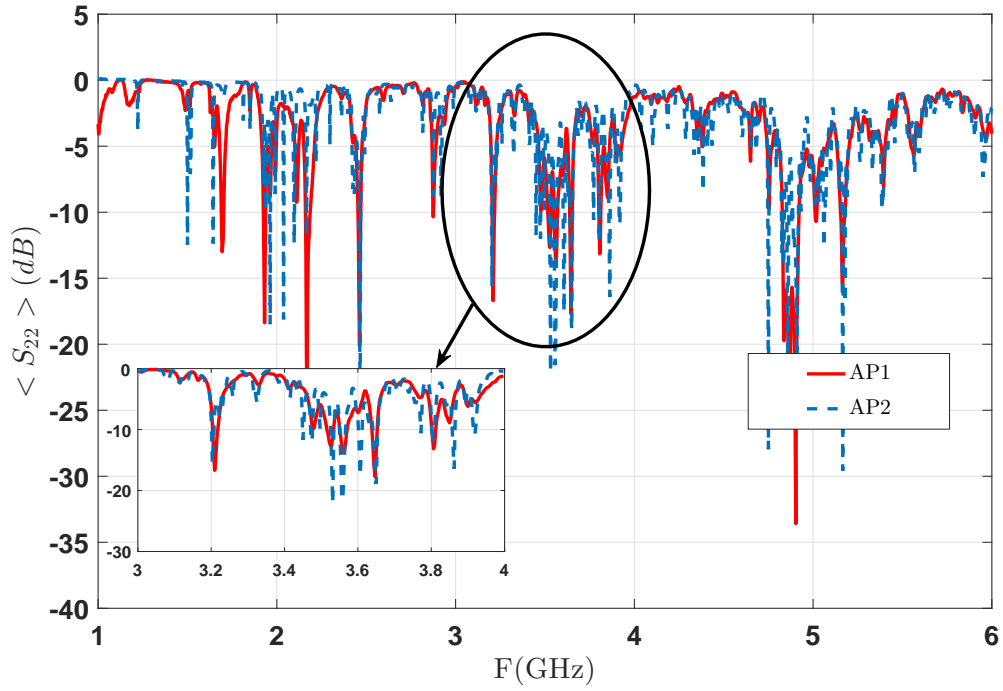
Figure 4.7: Average S_{22} over 50 tuner positions from external stirring (case 1) with AP1, AP2.

antenna in both cases.

Initially, a goodness-of-fit test for Rayleigh distribution was applied on the data (cases 1 and 2) from the internal and external stirring. The AD test is applied with Stephen's values, since it focuses on the tails more than the other tests with small number of samples [37]. The parameter of Rayleigh distribution used in the AD test can be defined by applying the concept of maximum likelihood in chapter 3. The estimated parameter $\hat{\theta}$ is defined by using Equation 3.27.

The AD test is applied for the 50 measured samples which is related to the 50 tuner positions at each frequency step for two mentioned different situations (cases 1 and 2). The results within 99% confidence interval are shown in Figures 4.9 and 4.10 for AP1 and AP2. Points below 0.01 indicate that the null hypothesis of magnitude samples following a Rayleigh distribution was rejected for that particular frequency and wire-probe position at $a = 1\%$ confidence level. Overall, the samples follows Rayleigh distribution with rejection

rate of 8% in Figure 4.9, which is consistent with the results in [19].
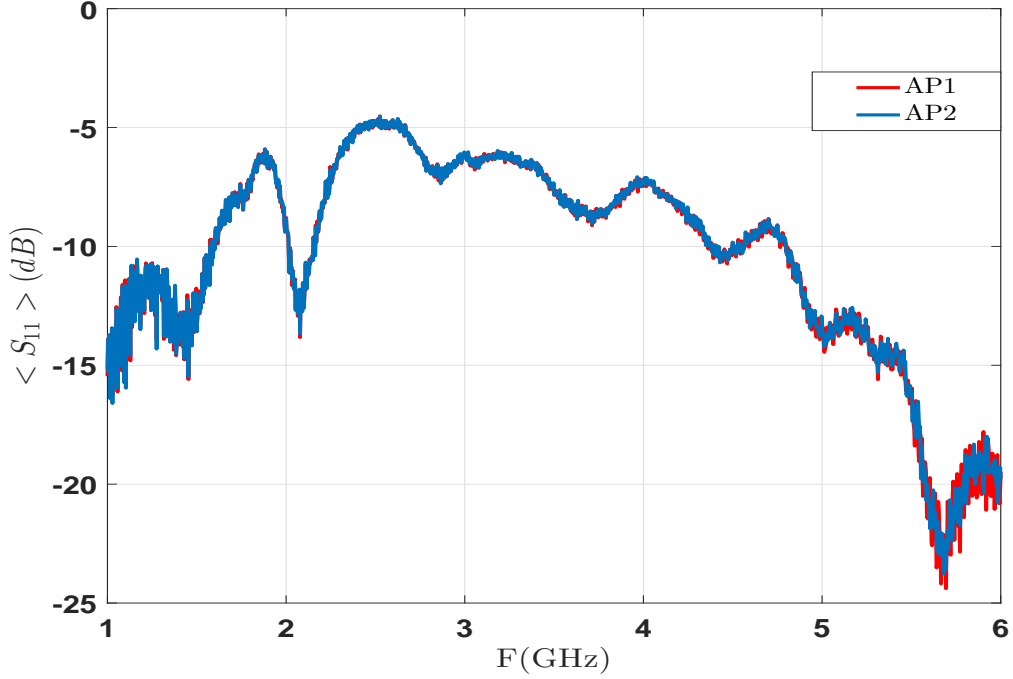
Figure 4.8: Average S_{11} over 50 tuner positions from external stirring (case 1) with AP1, AP2.

This is higher than 1% which is expected for ideal reverberation chamber but the chamber is not truly ideal here. However, for AP2 in low frequencies (below 2 GHz) the rejection rate is high (around 60%). This is likely due to the aperture dimensions. The aperture dimension is smaller than a wavelength below 2 GHz. Thus, energy could not couple through the aperture and the EUT box's environment reached to the noise floor [40]. Notably, the apertures are located at the center of the front face and effects of aperture's location remains a topic for future discussion.

Figure 4.10 shows the results for the internal rotation while the external tuner was fixed (case 2) at first tuner position. As shown, the samples are not generally following Rayleigh distribution. It seems that internal stirring inside the EUT box creates samples which follow a new distribution (a non-Rayleigh distribution). However, the rejection rate for AP1 at high frequencies is lower than the other scenario since both aperture dimensions are larger
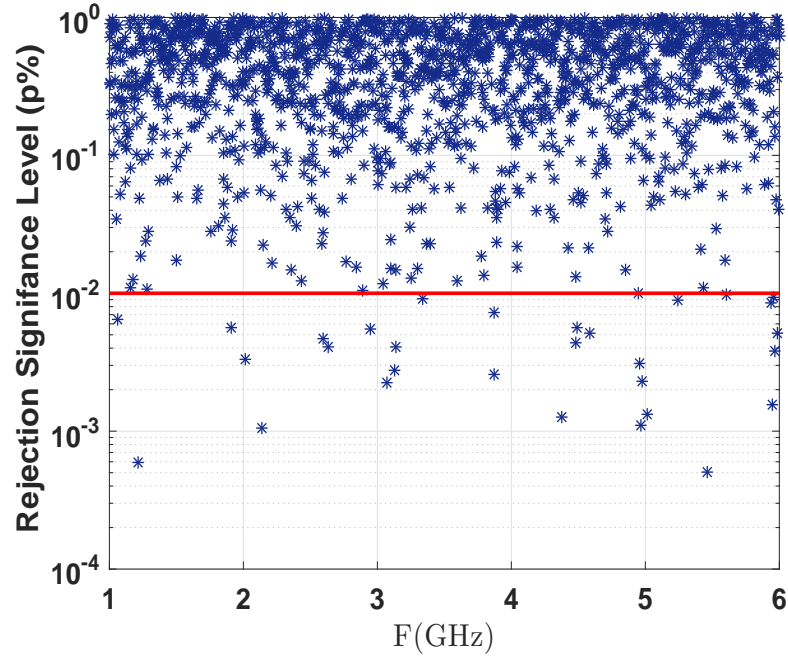
(a) Results from AP1.
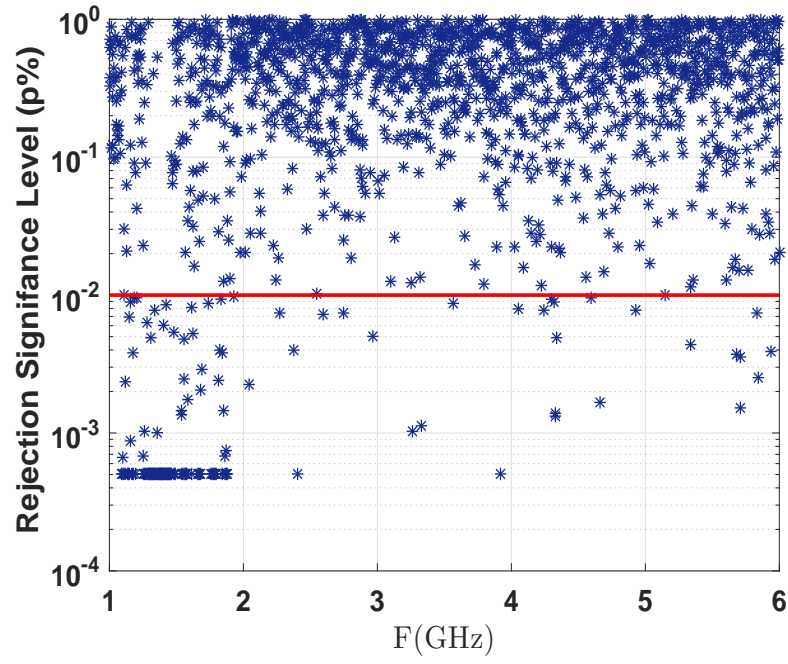
(b) Results from AP2.

Figure 4.9: Anderson-Darling test for Rayleigh distribution from external stirring (case 1) inside the EUT box in the nested chamber.
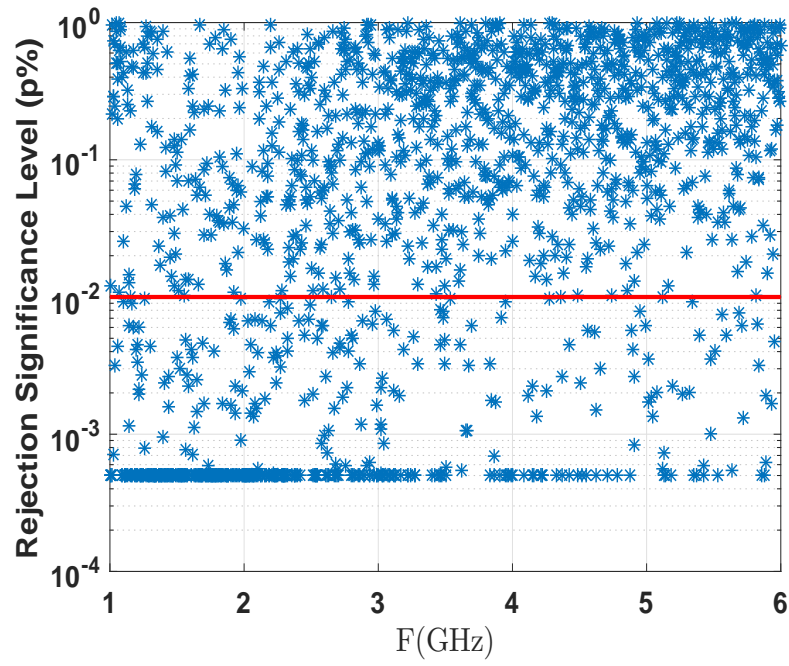
(a) Results from AP1.
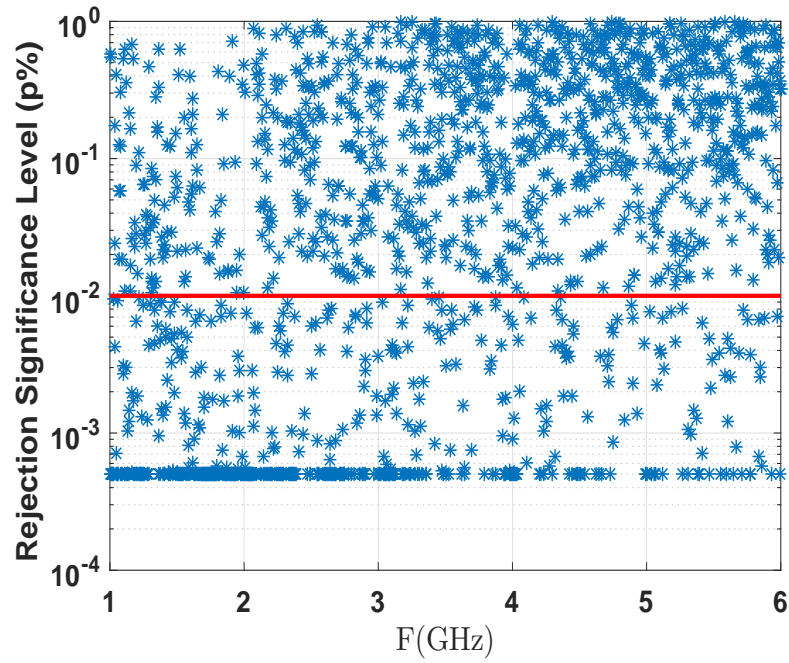
(b) Results from AP2.

Figure 4.10: Anderson-Darling test for Rayleigh distribution from internal stirring (case 2) inside the EUT box in the nested chamber.

than a wavelength at high frequencies [40]. The results in Figure 4.10 are consistent with the results in He [3] who showed that the field coupled through a small aperture on a straight wire probe in nested chambers does not follow Rayleigh distribution. However, the research made use of mechanical and frequency stirring while we used only mechanical stirring (external and internal).

4.2.2 The GEV Distribution Application

The maximum samples for all internal tuner positions (inside the enclosure) at a specific frequency at each external stirring step (till full rotation) is:

$$X(f,m) = \left\{ \max[E(f,m)] \Big|_{n=1....N} \right\} \tag{4.3}$$

where $n = 1....N$ indicates that the maximum over internal tuner position is taken.

This process generates $2,500$ samples in a specific frequency, which provide 50 maximum samples in this frequency. This resampling technique is called data blocking in [41]. In an under-moded regime, the environment is complicated due to a low number of modes (there is complex coupling between incident energy and enclosure modes). Therefore, the distribution becomes dependent on measurement location and a measurement at one location in an under-moded regime is no longer representative of the statistical distribution at another location. In that case, spatial sampling is suggested [38] from multiple probe locations across a volume of the EUT in order to provide the more realistic estimation of the GEV distribution and decrease uncertainty inside the EUT box. Since the box is in an under-moded regime below 2.7 GHz, the measurement was repeated with AP1 and AP2 in four positions with distance larger than $\Delta x = \frac{\lambda}{4} = 1.60 \; cm^2$ from each other (and from the walls) [19]. In total 200 maximum samples are produced by using spatial sampling and internal stirring. The GEV distribution can be applied at different frequencies. In this work, $f = 3.8$ GHz ($N \cong 175$, number of available modes), $f = 4.53$ GHz ($N \cong 301$), and

---

[2]The distance was calculated from the larger wavelength in this measurement.

$f = 5$ GHz ($N \cong 407$) are chosen since the EUT box is in the over-moded regime at those frequencies and $f = 1.93$ GHz ($N \cong 20$) is chosen since the EUT box is in the under-moded regime at this frequency.

As θ is a multidimensional variable for the GEV distribution, the standard deviation of the unbiased estimated of $\hat{\theta}$ can be defined as a square root of variance of θ which can be obtained from diagonal elements on the covariance matrix [42]. The covariance matrix between N variables can be defined as:

$$\mathbf{cov(x)} = \begin{bmatrix} x_1^2 & x_{12} & \cdots & x_{1N} \\ x_{21} & x_2^2 & \cdots & x_{2N} \\ \vdots & \vdots & \vdots & \vdots \\ x_{N1} & x_{N2} & \cdots & x_N^2 \end{bmatrix} \tag{4.4}$$

where $x_j^2 = \frac{1}{N}\sum_{i=1}^{N}(x_{ij} - \bar{x}_j^2)$ is the variance of the j-*th* variable, $x_{jk}^2 = \frac{1}{N}\sum_{i=1}^{N}(x_{ij} - \bar{x}_j)(x_{ik} - \bar{x}_k)$ is the covariance between j-*th* and k-*th* variables, and $\bar{x}_j = \frac{1}{N}\sum_{i=1}^{N}x_j$. The confidence interval is a type of interval estimation and consists of a range of values that act as good estimates of the unknown population parameter and it can be calculated by using Equation 3.20.

4.2.3 The EUT box in Over-moded regime

The EUT box is in over-moded regime at frequencies over 2.7 GHz as described in chapter 3. The GEV distribution is applied at frequencies 3.8 GHz, 4.53 GHz, and 5 GHz. In this work, we consider the distribution for each frequency separately as maximum distribution at each frequency is the topic of interest. As described in chapter 3, the GEV distribution has three different parameters, shape, scale and location that are needed to estimate. For this purpose, the maximum likelihood estimator was used to find the estimated parameters using Equation 3.27 in each aperture case.

Table 4.3: Estimated GEV distribution parameters for f = 3.8 GHz

Aperture	Parameters	$\hat{k}$	$\hat{s}$	$\hat{m}$
	$\hat{\theta}$	-0.0766	0.3082	1.0938
		-0.1791	0.27573	1.0457
$AP1$	C.I.(95%)			
		0.0259	0.3447	1.1419
	$\sigma^2_{\hat{k}}$	0.0027	$3.0841e-4$	$6.0192e-4$
	$\hat{\theta}$	-0.2301	0.2280	0.6593
		-0.3326	0.2041	0.6239
$AP2$	C.I.(95%)			
		-0.1275	0.2547	0.6947
	$\sigma^2_{\hat{k}}$	0.0027	$1.6545e-4$	$3.2631e-4$

Tables 4.3, 4.4, and 4.5 show the estimated parameters $\hat{\theta} = (\hat{k}, \hat{s}, \hat{m})$ for all aperture cases, the parameters within 95% confidence intervals, and the variances of each parameter for mentioned frequencies. As indicated, all samples in all situations follow the r. Weibull distribution which is an upper bounded distribution. This is consistent with the numerical and theoretical results in [38] and [5]. However, hybrid stirring was used in [38], while here only mechanical stirring and spatial sampling were applied. The estimated parameter within the 95% confidence interval may include values below zero to above zero in AP1 case, which indicate the existence of the Gumbel distribution inside the nested chamber. In addition, the estimated parameter (k) within 95% confidence interval follows the r. Weibull distribution in AP2, which is due to small dimensions of the aperture that do not allow coupling between two environments. The variance of the shape parameter is larger in all cases with AP2 than AP1 due to small aperture dimension which make two environments (inside and outside of the box) independent [3].
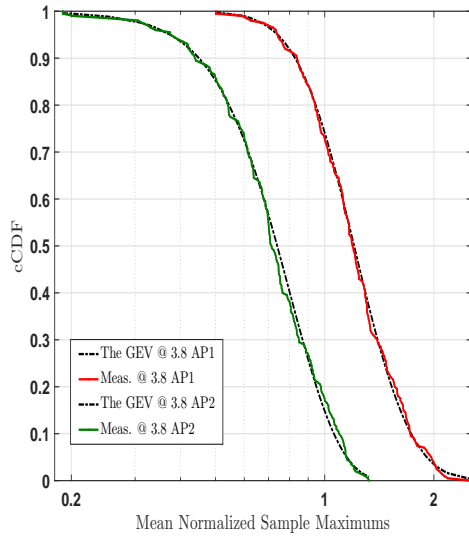
(a) cCDF.
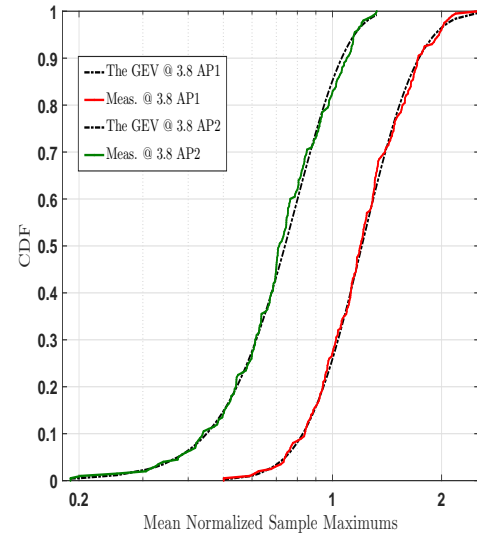
(b) CDF.
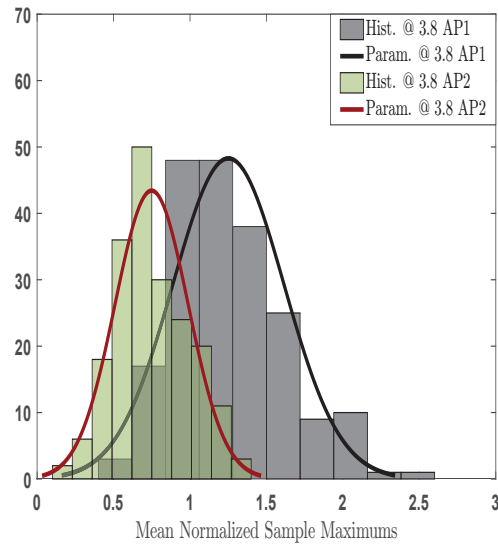
(c) PDF.

Figure 4.11: GEV vs. test data at f = 3.8 GHz.

Table 4.4: Estimated GEV distribution parameters for $f = 4.53$ GHz

Aperture	Parameters	$\hat{k}$	$\hat{s}$	$\hat{m}$
	$\hat{\theta}$	-0.0747	0.3016	1.1671
		-0.1730	0.2701	1.1202
$AP1$	C.I.(95%)			
		0.0235	0.3368	0.2139
	$\sigma^2_{\hat{k}}$	0.0025	$2.8805e-4$	$5.7105e-4$
	$\hat{\theta}$	-0.0899	0.2270	0.5655
		-0.1982	0.2027	0.5298
$AP2$	C.I.(95%)			
		0.0185	0.2542	0.6011
	$\sigma^2_{\hat{k}}$	0.0031	$1.7192e-4$	$3.3150e-4$

Figures 4.11(a), 4.12(a), and 4.13(a) show cCDF plots (empirical and parametric models) and Figures 4.11(b), 4.12(b), and 4.13(b) show CDFs (empirical and parametric models). The prametrically distribution is computed by applying the estimated parameters ($\hat{\theta}$) from maximum likelihood estimator for all aperture dimensions. The results show a high quality agreement between the mathematical and empirical (non-parametrically estimated distributions) results.

The maximum samples S_{21} can be binned to a histogram, for comparison with the ideal GEV distribution. Figures 4.11(c), 4.12(c), and 4.13(c) show histogram of the GEV distribution (empirical) with arbitrary bin widths. Black and dark red lines show the parametric estimated PDFs by using each aperture's dimension. As can be seen, there is a good agreement between the smooth line and the bins. The mean of the GEV distribution at all frequencies in AP1 is higher than AP2 due to large aperture dimension, which means more energy goes inside the box for all cases with AP1 compared to AP2.
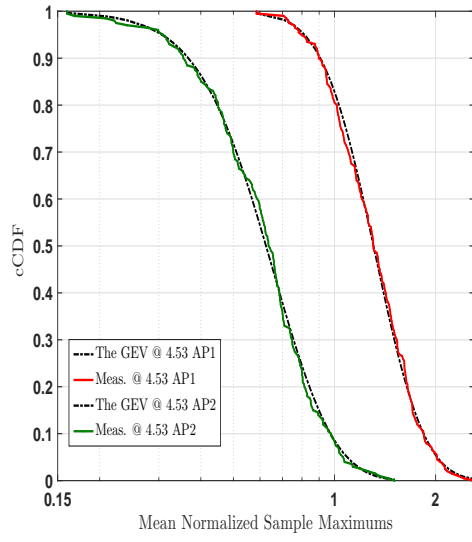
(a) cCDF.
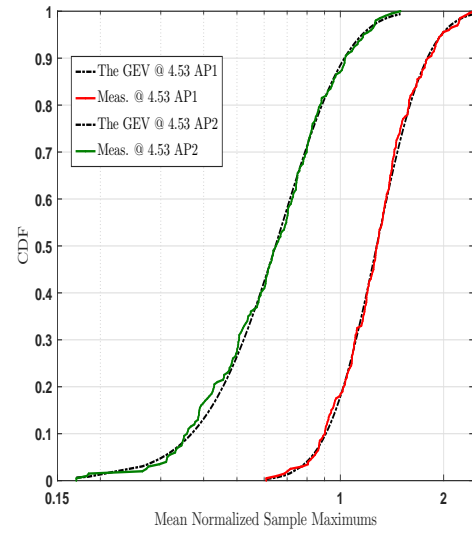
(b) CDF.
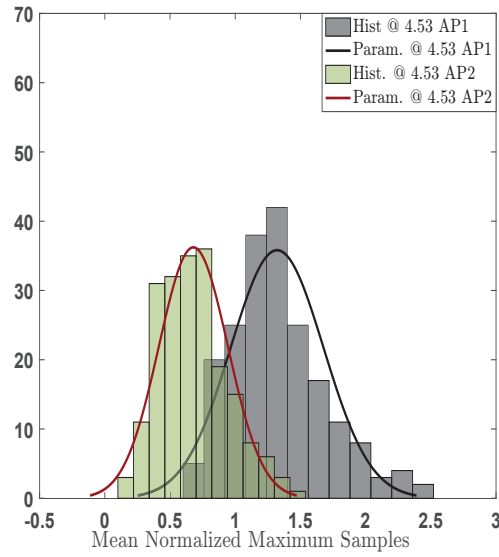
(c) PDF.

Figure 4.12: GEV vs. test data at $f = 4.53$ GHz.

Table 4.5: Estimated GEV distribution parameters for $f = 5$ GHz

Aperture	Parameters	$\hat{k}$	$\hat{s}$	$\hat{m}$
*AP*1	$\hat{\theta}$	-0.1215	0.3083	1.1082
	C.I.(95%)	-0.1934	0.2780	1.0616
		-0.0495	0.3420	1.1548
	$\sigma_{\hat{k}}^2$	0.0013	$2.6489e-4$	$5.6588e-47$
*AP*2	$\hat{\theta}$	-0.0307	0.2131	0.6328
	C.I.(95%)	-0.1304	0.1906	0.5996
		-0.0690	0.2383	0.6659
	$\sigma_{\hat{k}}^2$	0.0026	$1.4746e-48$	$2.8641e-4$

Overall, the GEV distribution converged to the r. Weibull distribution at strongly over-moded regime and aperture's dimension is not critical. The r. Weibull distribution which is known as an upper bounded distribution might be of interest in study of Electromagnetic Probability-of-Effect Assessment Tool (EMPAT) [1]. The measured results are consistent with previous measurement findings in terms of GEV distributions [38]. In this work, we used the maximum likelihood estimator to estimate the parameters. However, in previous work the empirical average and standard deviation of maximum values (theoretical expressions of the first and second central moment) was applied to estimate the parameters. Additionally, the GEV distribution can also be applied when the chamber is not sufficiently over-moded or not well stirred. This environment is called under-moded regime inside a reverberation chamber. The GEV distribution will be applied at this environment at a specific frequency and the results in terms of CDF, cCDF and PDF will be presented at the next section.
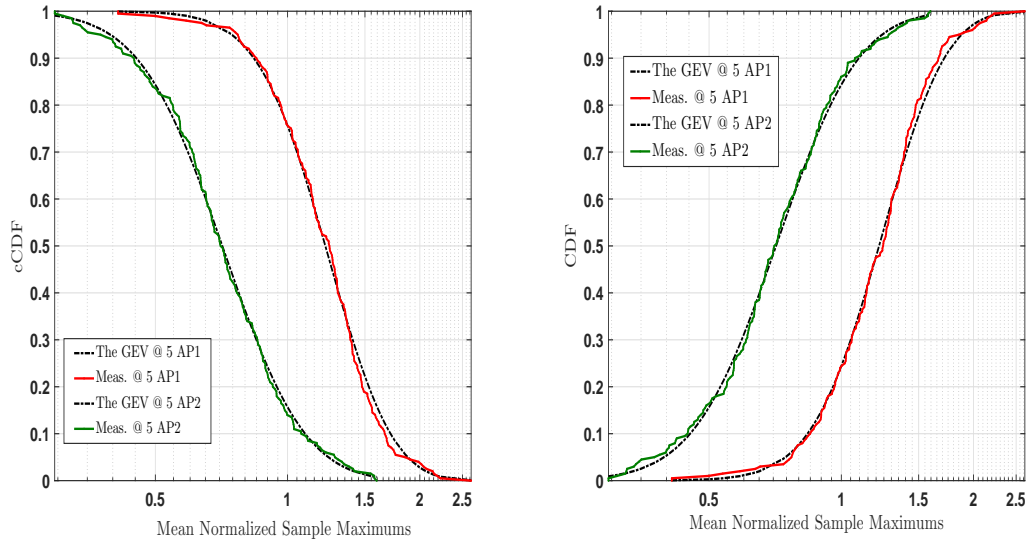
(a) cCDF.

(b) CDF.
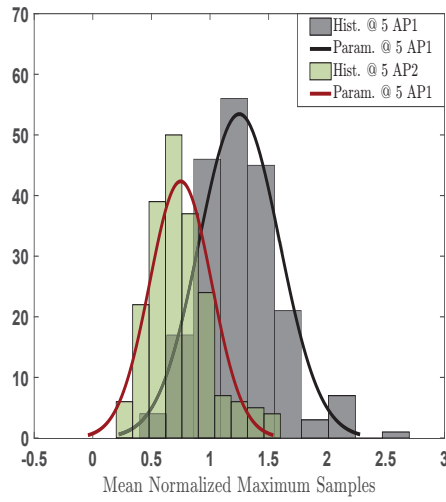
(c) PDF.

Figure 4.13: GEV vs. test data at f = 5 GHz.

4.2.4 The EUT box in Under-moded regime

The EUT box is in under-moded regime at frequencies under 2.7 GHz as explained in chapter 3. The GEV distribution is applied at frequency 1.93 GHz where a few modes exist

$(N \simeq 20$ [43]).

Table 4.6: Estimated GEV distribution parameters for f = 1.93 GHz

Aperture	Parameters	$\hat{k}$	$\hat{s}$	$\hat{m}$
	$\hat{\theta}$	−0.0059	0.6712	1.3613
$AP1$	C.I.(95%)	−0.1153	0.5980	1.2556
		0.1036	0.7533	1.4671
	$\sigma_{\hat{k}}^2$	0.0031	0.0016	0.0029
	$\hat{\theta}$	0.1973	0.0854	0.1839
$AP2$	C.I.(95%)	0.0778	0.0753	0.1704
		0.3168	0.0969	0.1974
	$\sigma_{\hat{k}}^2$	0.0037	$3.0232e-5$	$4.7703e-5$

The maximum likelihood estimator was again used to find the estimated parameters using Equation 3.27 in this case. Table 4.6 shows the estimated parameters $\hat{\theta} = (\hat{k}, \hat{s}, \hat{m})$ for all aperture cases, the parameters within 95% confidence intervals, and the variances of each parameter for mentioned frequency.

As indicated, all samples in AP2 case followed the Fréchet distribution with a fat tail ending, which is of an interest for EMC testing (predict higher field level) [1]. The estimated parameter within the 95% confidence interval all include values above zero, which shows that the value of $\hat{k}$ has not change significantly at the under-moded regime. This is consistent with the results in [41]. However, that works in [41] was emphasized under-moded regime in both reverberant environment and the EUT box, while we focused only on under-moded regime inside the EUT box. The results from AP1 case was differently (followed the r. Weibull distribution) due to the large aperture dimensions. In other words, the large aperture caused more energy from the reverberant environment goes inside the EUT box and makes two environment (inside and outside the EUT box) dependent [3]. Therefore, aperture's dimension has a critical role here.

Figures 4.14(a), 4.14(b) and 4.14(c) show the cCDF, CDF and PDF plots from para-

metric and non-parametric results at $f = 1.93$ GHz. As shown, all plots have an excellent agreement in each scenario and the results are within the confidence interval. Applying the GEV distribution throughout the under-moded regime in AP2 case showed that the maximum samples followed the Fréchet distribution. Notably, at low frequencies where a few modes exist, the GEV could not reasonably be applied.
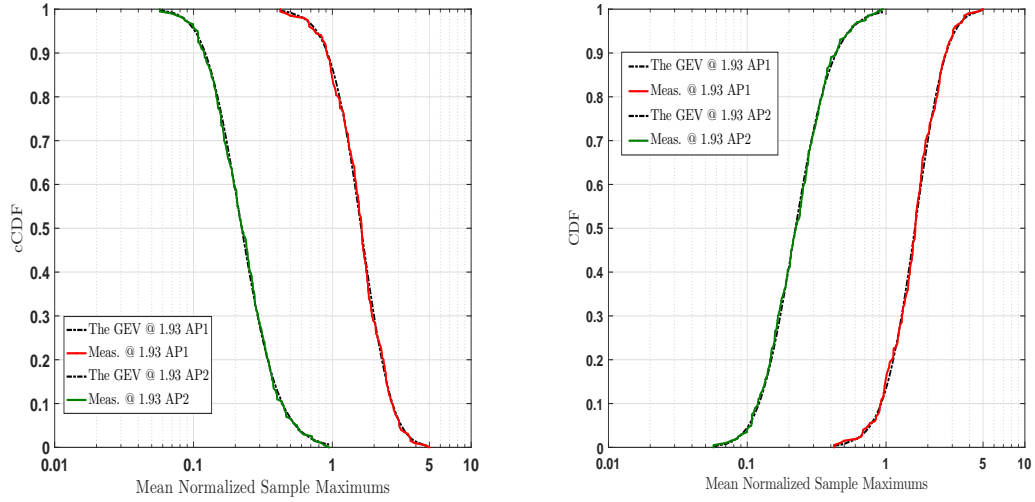
(a) cCDF.

(b) CDF.
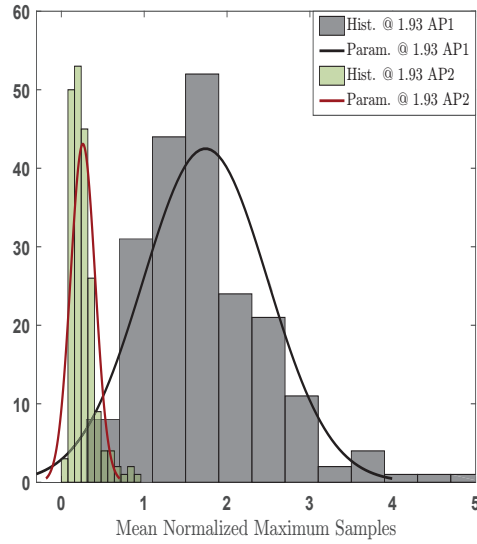
(c) PDF.

Figure 4.14: GEV vs. test data at $f = 1.93$ GHz.

As shown in sections 4.2.3 and 4.2.4, when the reverberant environment moves from an under-moded regime to over-moded regime, the GEV distribution switches from the Fréchet to the r. Weilbull distribution, which includes the Gumbel distribution. This aligns with the results in [38]. However, the results were presented in power while we focused on the magnitude of electric field. Overall, all results indicate that different types of the GEV distribution can be used inside the nested chamber and this might be interesting for EMV/C testing. Additionally, by decreasing the frequency and moving towards the under-moded regime, the variance of k parameters increase.

4.2.5 Uncertainty

This subsection relies heavily on the work of Tait et *al.* [43], and is included for completeness of the calculation of uncertainty. In this paper, mechanical stirring is used to mix the modes supported within an over-moded cavity. Locating a tuner within the EUT box generated a non-Rayleigh distribution. Since the parent distribution of the GEV estimation is unknown, the uncertainties of the expected maximum field measurement cannot be found analytically. However, since the GEV distribution is analogous to statistical transfer function, shielding effectiveness estimation uncertainty found from the same samples is considered here.. However, since the GEV distribution is analogous to statistical transfer function and there is a finite number of mode-stirring samples, three different uncertainties considered here. Notably, the addition of internal stirring to reverberation chamber testing is useful because it adds more independent samples of the internal field distribution and decreases the uncertainty in the field level measurements. The uncertainty due to internal stirring and spatial sampling (which can be commonly used for EMC/V testing to increase the number of samples) can be assessed by applying the central limit theorem to the samples collected under internal mechanical stirring and spatial sampling with the external tuner in a fixed position. As described in previous section, there are 200 samples (4 different probe position) from spatial sampling and internal stirring.
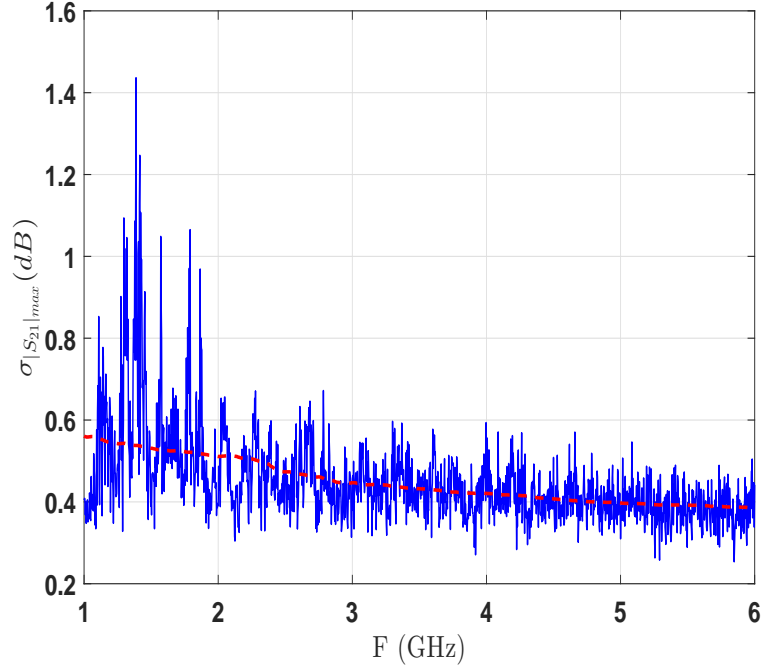
Figure 4.15: Standard deviation of $|S_{21}|_{max}$ in a probe position. Red dash line shows the general trend by varying standard deviation vs. frequency.

As described in previous section, there are 200 samples (4 different probe position) from spatial sampling and internal stirring. The standard deviation of $|S_{21}|_{max}$ in dB is [10]:

$$\sigma_{|S_{21}|_{max}}(dB) = 20\log\left[1 + \frac{\sigma_{|S_{21}|_{max}}}{< |S_{21}|_{max} >}\right]. \tag{4.5}$$

The uncertainty in the estimate of the mean of $|S_{21}|_{max}$ using 50 samples taken with one probe position can be found by applying the central limit theorem to Equation 4.5 and replacing the numerator with $\frac{\sigma_{|S_{21}|_{max}}}{\sqrt{N}}$, which gives [43]:

$$\sigma_{< |S_{21}|_{max} >}(dB) \cong 20\log\left[1 + \frac{\frac{\sigma_{|S_{21}|_{max}}}{\sqrt{N}}}{< |S_{21}|_{max} >}\right]. \tag{4.6}$$

Figure 4.15 shows the uncertainty of 50 samples in one probe location. The values range from around 0.25 dB to 1.45 dB, with a mean of approximately 0.45 dB. The range and mean are nearly the same at all four probe positions. When the internal tuning and

74

spatial sampling are used together to yield 200 independent samplings, equation 4.6 with $N = 200$ gives a total uncertainty of 0.3 dB in the estimate of the mean of $|S_{21}|_{max}$ when all 200 samples simultaneously. Notably, adding mechanical stirring within the EUT gives a critical improvement in the uncertainty of the measurement of the internal field, but can not remove it completely. This will be shown in chapter 6. Additionally, there are absolute uncertainties in the measurement [43] within the EUT box when the internal tuner is included which must be assessed. This will be a topic of future investigation.

4.2.6 Conclusion

The GEV distribution has three different parameters and this work has focused on the shape parameter that can change the type of the distribution. The GEV distribution was applied in scenarios that the parent distribution was unknown (non-Rayleigh distributed) inside an unloaded EUT in order to model the maximum field level. The situations occurred when mechanical tuning was applied to the EUT enclosure in both external and internal stirring and there was no frequency stirring. Moving the tuner with certain steps inside the enclosure effectively might lead to change in the configuration of the EUT itself in the same way that frequency stirring can do statistically and is discussed [40]. In fact, adding internal stirring fundamentally and statistically changes the operation of a reverberation chamber test. Since there are conditions that the parent distribution is not clear and the traditional method [13] is not useful, the GEV distribution is well suited. Notably, the analysis here was experimentally based. The effects of differing numbers of samples [44] or aperture locations other than centered on a EUT enclosure wall were not considered. Also, the measurement probe was limited to a simple straight monopole. Measurement with a long-wire probe that samples more of the EUT internal volume could potentially lead to different results, particularly at low frequencies where the modal density within the enclosure is low [43]. These effects will be examined in subsequent work.

CHAPTER 5

VALIDATION OF THE GENERALIZED EXTREME VALUE DISTRIBUTION INSIDE A LOADED CHAMBER

In this chapter, we will begin in section 5.1 with the description of a one-port technique to measure the quality factor (Q) inside the EUT box, while it is loaded by absorbing materials. In section 5.2, the results of quality factor while EUT box is loaded is shown and analyzed. Additionally, the GEV distribution is applied to model the maximum field level when the EUT box is loaded, compared to the Bremner's work in [4] which needs a high quality factor. Additionally, Holloway *et al.* mentioned in [45] that the statistical description inside the reverberation chamber might change due to locating absorbing materials inside a reverberation chamber. Therefore, the GEV distribution is required to be validated in the load EUT box. The results of applying the GEV distribution with unloaded vs. loaded EUT box in AP1 case are shown and analyzed. Additionally, comparison between unloaded and loaded EUT box is presented.

5.1   Quality Factor inside the EUT Box

5.1.1   Quality Factor Measurement

Quality factor (Q) is a critical parameter for reverberation chambers analysis, that defines the available energy inside a reverberation chamber for a given input power. The quality factor determines the available stored energy that interacts with the EUT and is related to other test characteristics of the chamber such as build-up and decay times that impact the time domain response. The same EUT cavity and tuner as described in chapter

(a) Measurement set-up.

Top View
Absorbing Material positions
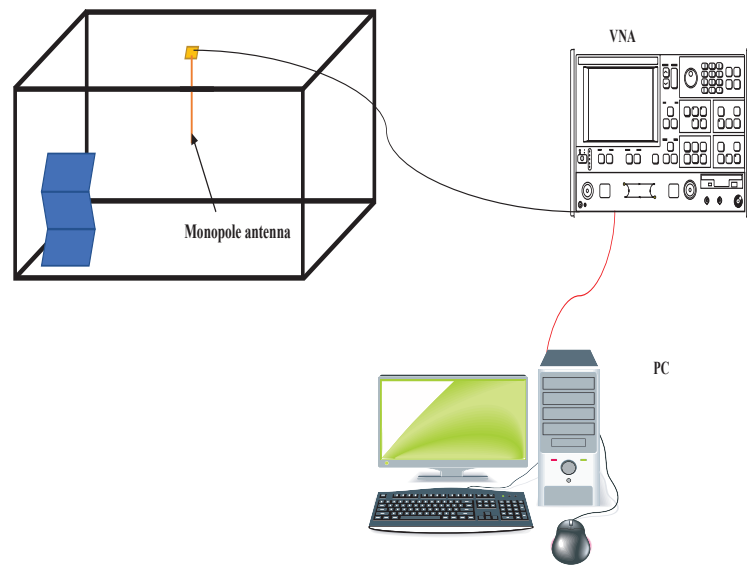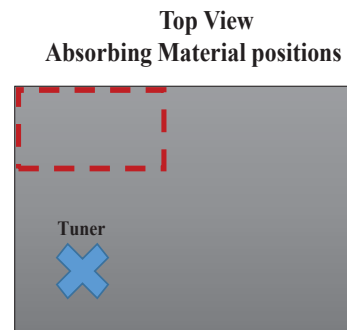
(b) Absorbing material location.

Figure 5.1: Quality factor Measurement cavity configuration with z-fold tuner. The absorber position is shown by the dashed line on the cavity floor.

[4](#) were used in this chapter. The internal dimensions of the cavity are too small to allow the inclusion of two antennas that are well isolated in order to reduce direct coupling for measurement. Instead the one-port time domain method of [46] was used. Notably, the methodology was compared to modal curve fitting in [47] and the potential use and consistency between two techniques are demonstrated. Use of a single antenna has the added advantage that the cavity is less loaded by measurement ports and gives a better representation of the Q of the chamber alone [48]. The measurement was performed by placing a VNA on the probe feed connector and measuring the S_{11} scattering parameter (or reflection coefficient) at that port at discrete frequencies within the operating band across numerous tuner positions. The VNA then synthesized the time-domain response of the reflection from the frequency-domain S_{11} using a fast Fourier transform. A Kaiser-Bessel window is applied to the frequency-domain spectrum to avoid replication of the signal. Once the time-domain response has been found for each tuner position, they are all averaged across tuner positions to give a mean chamber time-domain response. The decay time of the energy within the cavity represents a power-loss profile that can be used to find the Q. The chamber time constant is calculated by using Equation [2.19](#) and Q is computed by using Equation [2.20](#). In the results shown below, the mean chamber time-domain response was found by averaging the time-domain S_{11} over 50 tuner positions. $1,601$ frequency samples, the maximum capability of the VNA, were used at each bandwidth considered so the frequency sampling step is a function of the signal bandwidth. The center frequency was from 3 to 6 GHz in 1 GHz step, and the bandwidth was 1 GHz (as explained in chapter [3](#), the EUT box is over-moded regime, at frequencies above 2.7 GHz).

The sampling step used in the frequency domain by the network analyzer at the greatest bandwidth was

$$\Delta f = \frac{1 \times 10^9}{1600} = 0.625\,\text{MHz},\tag{5.1}$$

which corresponds to a maximum response time of

$$\frac{1}{\Delta f} = 1.6 \, \mu\text{s}. \tag{5.2}$$

The measurements were performed with the cavity both unloaded and loaded with an absorbing material. Figure 5.1 shows the required setup to measure Q inside the EUT box. The loading material used was a 10 cm by 10 cm by 0.25 cm section of ARC Technologies model UD-11554 silicon rubber absorber. The materials were located at the corner of the box in front of the tuner that as shown in Figure 5.1 and the measurements repeated for the same center frequencies and bandwidth used for the unloaded cavity.

5.2 Results and Analysis

5.2.1 Quality Factor Measurement Results

The responses are plotted only to 300 ns for all center frequencies for ease of comparison.
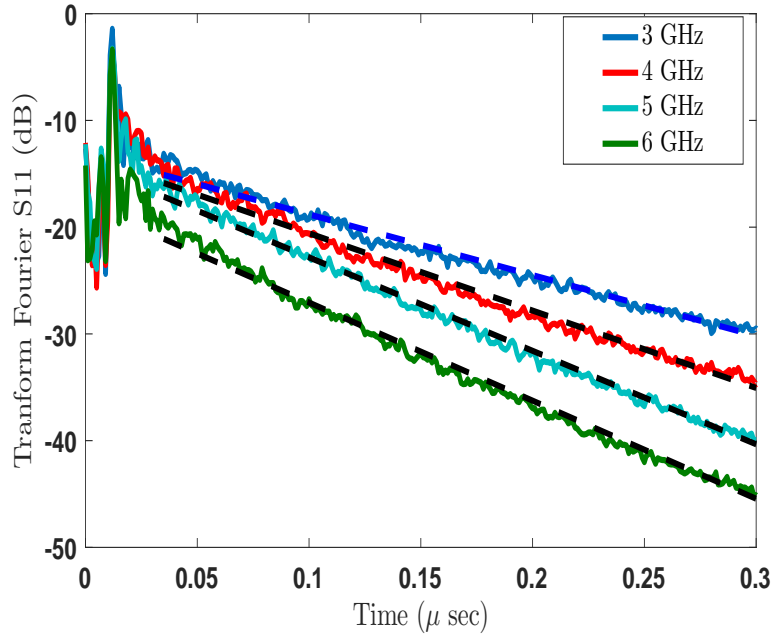
Figure 5.2: Measured mean chamber time-domain response for different center frequencies when the cavity is unloaded.

The pre-reverberant phase extends for approximately 30 ns in each case. The linear regression fit to establish the chamber decay time was therefore applied to the range from 4 ns to 300 ns to ensure that the reverberant stage had been established. The linear fits associated with each response are shown as the dashed lines. The responses with different center frequencies (only linear response) are shown in Figure 5.2. Energy normalization in the VNA processing algorithm explains the dependence on the overall level of the responses on signal bandwidth. The overall level does not affect the decay rate or extracted Q so is not compensated. The response levels are plotted as directly provided by the VNA.
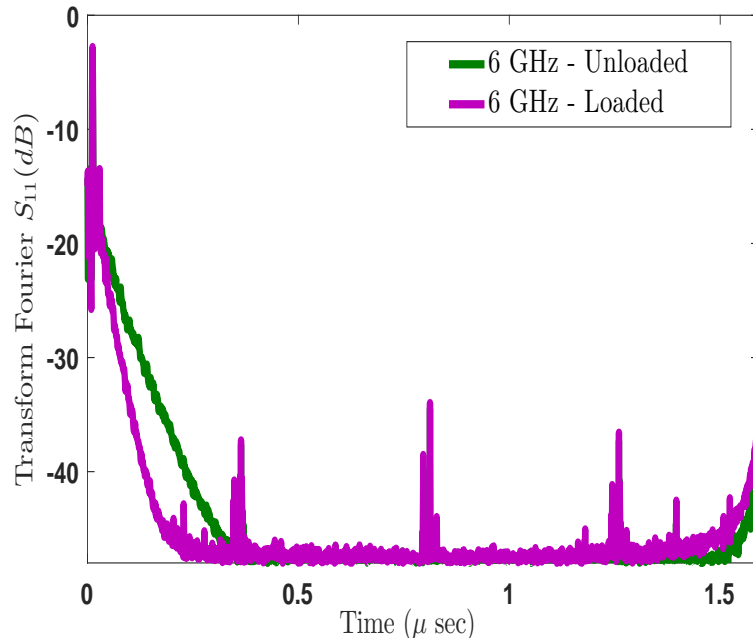
Figure 5.3: Measured mean chamber time-domain response for when the cavity is unloaded and loaded at 6 GHz.

Figure 5.3 shows the comparison between time domain responses for both unloaded and loaded EUT box at 6 GHz. The Q values found from each fit are summarized in Table 5.1. Notably, absorbing materials change the slope of time domain response and reduce the quality factor inside the EUT box. This loading is representative of a moderately loaded chamber to represent electronic devices inside the reverberant environment (loading the

chamber). Standards recommend 12 dB of loading [10] to asses chamber performance when expected loading due to an EUT is unknown. As can be seen, the Q was decreased around 8 dB by locating UD material inside the box.

Table 5.1: Q factor as a function of center frequency for unloaded and loaded cavity.

$Q(dB)$	Center Frequency			
	3 GHz	4GHz	5 GHz	6 GHz
Unloaded	31.43	32.68	33.65	34.44
Loaded-UD	23.13	24.38	25.34	26.14

5.2.2 Statistical Analysis

The measurement in section 4.1 was repeated again to collect the samples with AP1 and AP2 while the EUT box is loaded. The GEV distribution is applied in the over-moded and under-moded regimes to model the maximum distribution. Several different frequencies are chosen in the under-moded and over-moded regimes in order to validate the GEV distribution, while the EUT box has a low quality factor in AP1 and AP2 cases.

$$\Delta Q = Q_{unloaded} - Q_{Loaded} \approx 8 \ dB.$$

The methodology to calculated the quality factor that described in section 5.1 is only valid at over-moded regime and non-linear (second-order polynomial) extrapolation was used to estimate the quality factor value at the under-moded regime. The estimated parameters tables and CDF and cCDF plots are shown in next section in order to compare unloaded and loaded EUT box.

5.2.3 Unloaded EUT box vs. Loaded EUT box

The GEV distribution needs to be validated the maximum field in the cases that the quality factor of the EUT box is decreased, since the other method [4] is only valid in

81

unloaded EUT box. Validation of the GEV distribution was performed with both AP1 and AP2 cases at frequencies 6 GHz, 5 GHz (extremely over-moded regime), and 1.93 GHz (under-moded regime).

Tables 5.2 and 5.3 show the estimated shape parameter in each aperture case and compare the values with unloaded EUT box scenario. As indicated, shape parameter in all cases in AP1 case has a negative value which indicates the GEV distribution converges to the r. Weibull distribution. This means that the large size of the aperture allows coupling between two environments. However, the GEV distribution converges to the r. Weibull distribution in over-moded regime in AP2 case and to the Fréchet distribution in under-moded regime (positive value of shape parameter).

Table 5.2: $\hat{k}$ value for AP1 case - unloaded vs. loaded.

Frequencies	6 GHz	5 GHz	1.93 GHz
Q(dB)	34.44	33.65	30.02
$\hat{k}$- unloaded EUT	-0.1561	-0.1215	-0.0059
Q(dB)	26.14	25.34	21.58
$\hat{k}$- loaded EUT	-0.0538	-0.0837	-0.0346

Table 5.3: $\hat{k}$ value for AP2 case - unloaded vs. loaded.

Frequencies	6 GHz	5 GHz	1.93 GHz
Q(dB)	34.44	33.65	30.02
$\hat{k}$- unloaded EUT	-0.0328	-0.0307	0.1973
Q(dB)	26.14	25.34	21.58
$\hat{k}$- loaded EUT	-0.0036	-0.1338	0.1226

(a) cCDF.

(b) CDF.
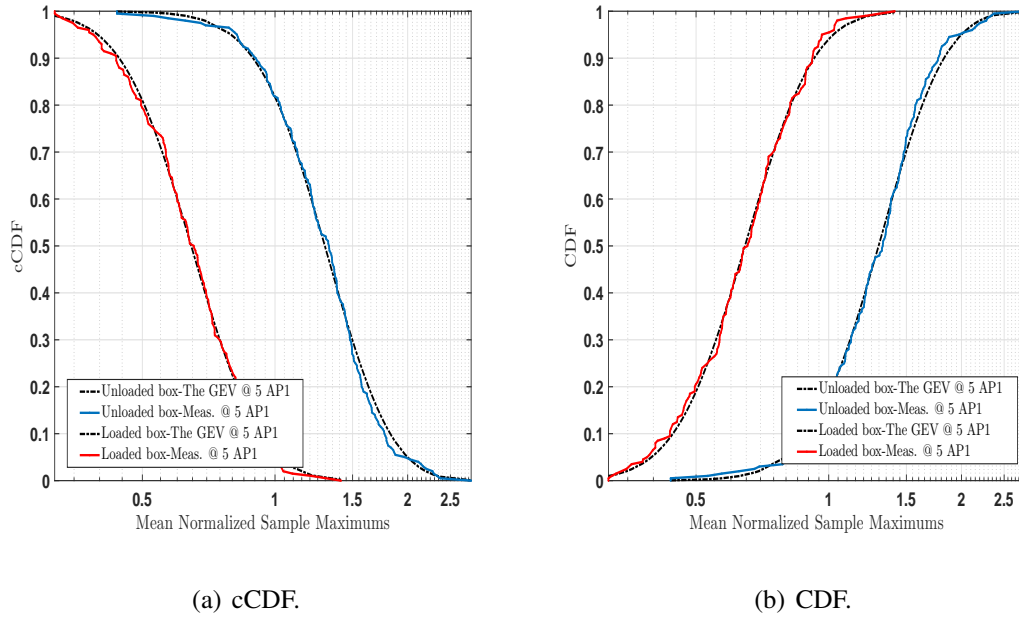
Figure 5.4: GEV distribution-unloaded vs. loaded EUT box in AP1 case at f = 5 GHz.

In fact, Tables 5.2 and 5.3 suggest that the dimensions of the aperture in validation of the GEV distribution is not critical at over-moded regime, despite of the amount of available energy that exists inside the EUT box. In other words, it seems that the maximum distribution converges to the r. Weibull distribution at over-moded regime regardless the dimension of the aperture at the EUT box. However, the dimension of aperture has a key role in under-moded regime. As can be seen, the results followed the r. Weibull distribution in AP1 scenario due to the aperture's dimension while converged to the Fréchet in AP2 case. It seems more energy goes inside the EUT box in AP1 scenario despite the UD material absorb a specific amount of the energy. Overall, a small aperture makes two environments inside and outside the EUT box independent [3] and the maximum field level converges to the Fréchet distribution which is consistent with the results in chapter 4. Figure 5.4 shows the cCDF, CDF of the GEV distribution for the mentioned frequencies at AP1 case. It can be seen that, the parametric and non-parametric results are fitted very well. The samples in unloaded AP1 case have a larger mean than the samples from loaded AP1 case due to

the locating absorbing materials inside the EUT box, which cause energy absorbs before coupling on the straight wire probe from the aperture.

(a) cCDF.

(b) CDF.
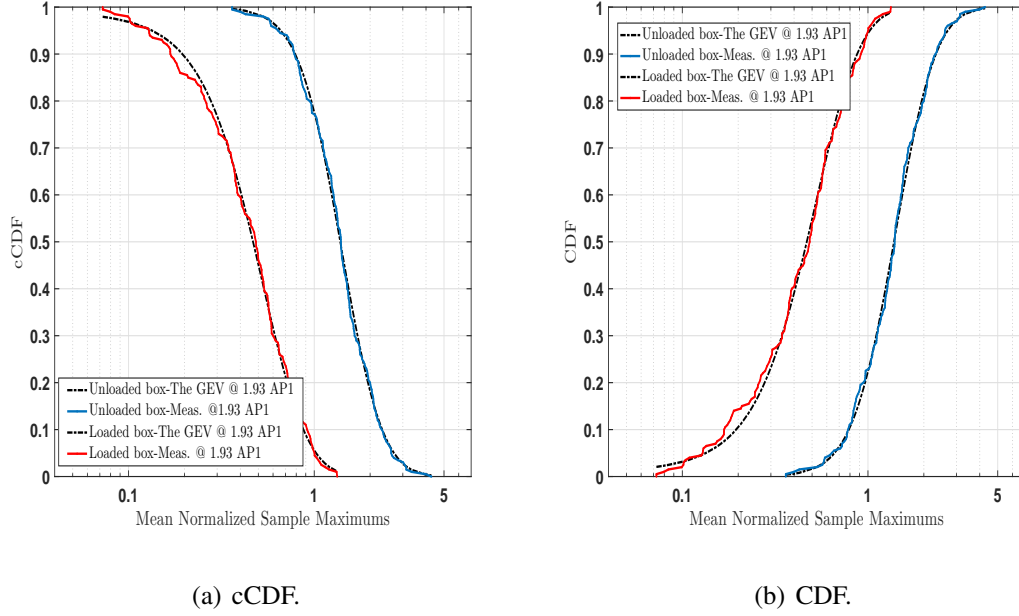
Figure 5.5: GEV distribution-unloaded vs. loaded EUT box in AP1 case at $f = 1.93$ GHz.

In under-moded operation, standard deviation from the ideal field is large which leads a significant effect on the statistical description inside reverberant environment. Therefore, the GEV distribution is a useful method to predict the field level directly at under-moded regime. The GEV distribution was applied for unloaded EUT box at under-moded regime in section 4.2.4. In order to complete the validation of the GEV distribution, the distribution is used to model the maximum level at under-moded regime with the loaded EUT box. As indicated, the GEV distribution converges to the r. Weibull distribution in AP1 case either (the EUT box is unloaded or loaded) due to the big aperture dimension (the SMART-80 is in over-moded regime) as indicated in Table 5.3. Additionally, the cCDF plot at frequencies 6 GHz with both AP1 and AP2 cases are shown in Figure 5.6. As can be seen the results with AP1 have a larger mean compared to AP2 results due to the aperture's dimension.

Overall, though locating absorbing materials could affect on the amount of available
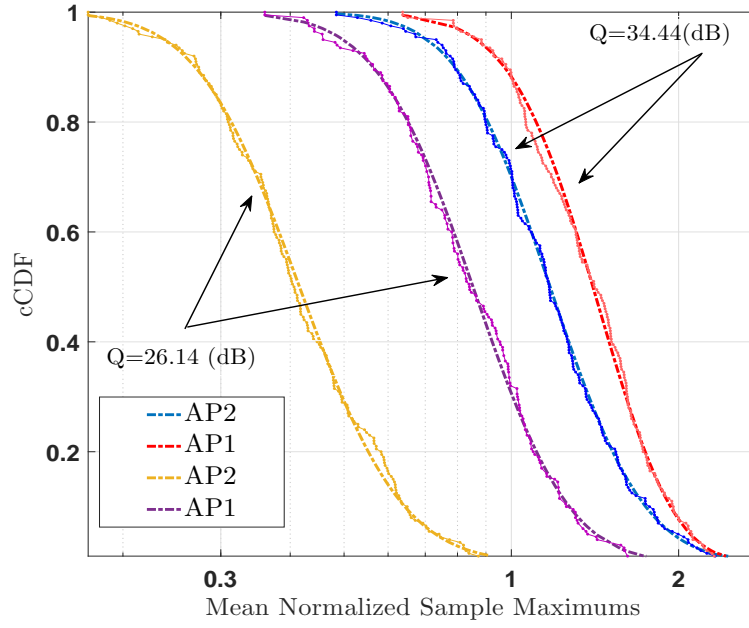
Figure 5.6: GEV distribution by applying maximum likelihood estimator with AP1 vs. AP2 at frequency 6 GHz.

energy and also change the performance of a reverberation chamber, the GEV distribution has a good agreement in both apertures' scenario. Notably, UD material is a Silicon rubber family material that has different permittivity and permeability at each frequency. This means that the material behaves differently at each frequency and that is not considered here. Responses with non-magnetic foam absorber loading are visibly more linear [29]. This effect will be further studied in later work.

5.3 Conclusion

In this chapter, we validated experimentally the GEV distribution while the quality factor of the EUT box was decreased by locating absorbing material. The Q of the enclosure box was measured by using one port technique method. The CDFs and cCDFs plot was shown for each situation. Overall, the results had a good agreement while the method in [4] is not able to predict the maximum field by low quality factor. Additionally, it

seems that k parameter would be larger at the under-moded regime when the EUT enclosure was unloaded which lead to a fatter tail [5]. Notably, we concentrated at AP2 case at the under-moded regime due to the shape and dimension of the aperture. However, the reverberant environment was at over-moded regime at all of the measurements and the aperture dimension was a critical parameter to transfer energy inside the EUT box. The conditions that the SMART-80 (below 80 MHz) works at the under-moded regime remains a topic for future discussion.

CHAPTER 6

ESTIMATION OF REQUIRED ABSORBING MATERIAL DIMENSION INSIDE METAL CAVITIES

Generally, a random dimension or random number of absorbers is used inside an enclosure to see how much absorption can be reached [28] as we did in chapter 5. If the absorption is insufficient, the dimensions of the absorbers is decreased or increased randomly to earn the required Q inside the enclosure. Performing all of the measurements or the simulations is time consuming, and expensive, and they need to be verified in various aspects. As an alternative to this approach, we propose to collet experimental data, including Q values, for a variety of absorber materials and dimensions. We will then train a neural network to interact the process. In this chapter, we used multi layers perceptron (MLP) as function approximators to estimate the dimension of materials to have a specific Q inside a small cavity. The MLPs were trained to minimize the mean square error between the network output (estimated absorber dimension) and target outputs (measured absorber dimension), which were collected from experiments. [1]

6.1 Important Parameters Which Effect Quality Factor

There are various parameters that can effect the Q factor of a chamber. In this section, we explain some of the parameters that are used in the multi layer perceptron (MLP). Absorbing materials that have different properties can change amount of available energy

---

[1]This chapter was presented under the title "Estimation of Required Absorbing Material Dimensions inside Metal Cavities Using Neural Networks", N. Nourshamsi, M.T. Hagan, C.F. Bunting, IEEE EMC Symp., 2017 [49].

inside the cavity.

Absorbing materials can be recognized by their permittivity and permeability. Permittivity describes the interaction of a material with an electric field, while permeability describes the interaction of a material with a magnetic field. These properties are helpful in understanding why the material behaves differently at various frequencies. In addition, permeability and permittivity of materials change with frequencies [10]. Their measurement can be performed by locating materials inside a waveguide and using a transmission line to measure the reflection and transmission coefficient [50]. Permittivity (ε), and permeability (μ) have real (related to the stored energy within the medium) and imaginary (related to the dissipation of energy within the medium) parts [50]:

$$\varepsilon = \varepsilon' - j\varepsilon'', \tag{6.1}$$

$$\mu = \mu' - j\mu'', \tag{6.2}$$

Relative permittivity and permeability are defined [50]:

$$\varepsilon_r = \frac{\varepsilon}{\varepsilon_0}, \tag{6.3}$$

$$\mu_r = \frac{\mu}{\mu_0}, \tag{6.4}$$

where ε_0 and μ_0 are permittivity and permeability of free space. In addition, the dimension of the absorbing materials affects the quality factor of the chamber. It has been shown [29] that increasing the size of absorbing sheets inside the chamber can decrease the quality factor.

There are also other parameters that can affect the quality factor, such as aperture dimension, number of apertures and the position of materials that are not considered in this problem. Figure 6.1 shows the inputs and outputs of the network.
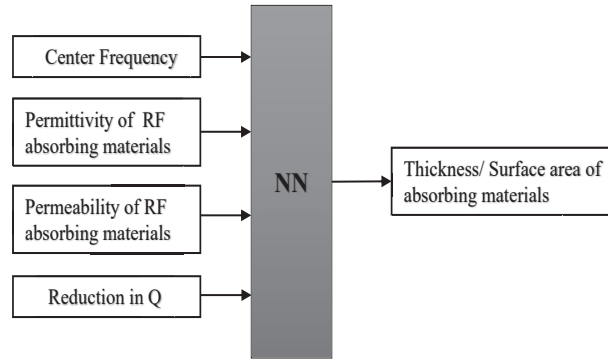
Figure 6.1: Inputs and outputs of the network.

6.2 Case Study

In this section, we describe a case study in order to understand a function approximation problem. "Function approximation can be defined as a mapping between a set of input variables and a corresponding set of output variables" such as estimating the acceptance of loan, based on salary, house rent and available credits [7]. In this case study, we consider a smart sensor system that decreases the voltage of the solar cells by increasing shadow. Figure 6.2 shows the description of the sensor.
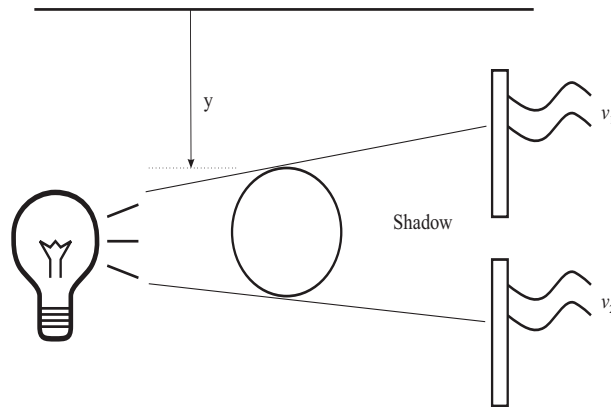
Figure 6.2: Position Sensor Arrangement [7].
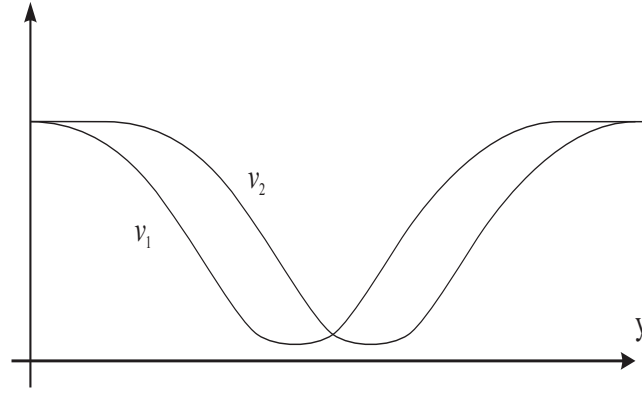
Figure 6.3: Example Solar Cell Outputs vs. Object Position [7].

As shown in Figure 6.3 when position y increases, the voltages v_1 and v_2 decrease respectively. Therefore, the goal is to estimate the object position by knowing the voltages v_1 and v_2. This is obviously a nonlinear problem, and a multilayer network will be used to find the function. The input vector for network can be defined the solar cell voltages:

$$\mathbf{P} = \begin{pmatrix} v_1 \\ v_2 \end{pmatrix}, \tag{6.5}$$

and the target will be ball position

$$t = y. \tag{6.6}$$

Notably, this can be defined as a classic function approximation problem due to computing the inverse of a function.

6.3   Neural Network

In this section, a brief introduction to neural networks and its application in different fields. Neural Networks have diverse applications, such as fitting, pattern recognition, clustering. In this section, we concentrate on the most common neural network architecture:

the multi-layer perceptron and its application to function fitting. Overall, the quality factor of a chamber is a function of the dimension of absorbing materials, the location, frequency range, number of apertures, size and shape of aperture and properties of materials, but for this work the input are limited to quality factor reduction, frequency, permeability, permittivity, and dimensions of absorbing materials.

The input to the network is:

$$\mathbf{P} = \begin{pmatrix} \Delta Q \\ F \\ \varepsilon_r' \\ \varepsilon_r'' \\ \mu_r' \\ \mu_r'' \end{pmatrix} \tag{6.7}$$

where $\Delta Q = Q_{empty} - Q_{loaded}$, Q_{empty} is the Q for the empty enclosure and Q_{loaded} is the Q for the enclosure with the absorbing material. In the next sections, the multi-layer perceptron neural network and how it can be used to approximate a function will be introduced.

6.3.1 Single-Input Neuron

Firstly, a single neuron is introduced, which can be useful to understand the multi-layers of the network. A single input neuron is shown in Figure 6.4. As we can see, the scalar input p is multiplied by a scalar weight w and then summed with a bias b to determine the output n which is referred to as the net input and goes to the transfer function f which produces the neuron output a [7].

Therefore, the neuron output is calculated as:

$$a = f(wp + b). \tag{6.8}$$

where w, b are both adjustable parameters of the neuron.
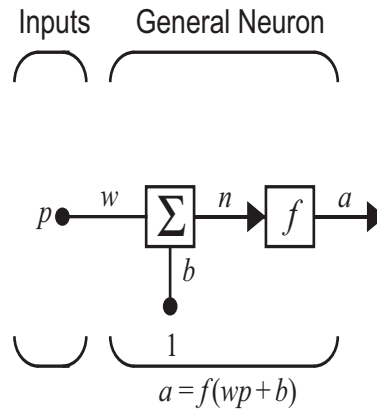
Figure 6.4: Single-Input Neuron [7].

6.3.2 Transfer Functions

The transfer function will be chosen to satisfy the specification of the problem that the neuron tries to solve. A transfer function can be a linear or a nonlinear function of n. Since the problem is nonlinear here, the Hyperbolic Tangent Sigmoid is chosen. This transfer function takes the input and the out put will be between -1 and 1.
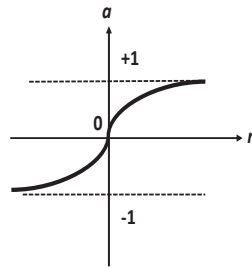
Figure 6.5: $a = tansig(n)$.

$$a = \frac{e^n - e^{-n}}{e^n + e^{-n}}.$$ (6.9)

The Equation 6.9 shows the input and output relation of this function and Figure 6.5 shows the the graph of this function.

6.3.3 Multiple-Input Neuron

Generally, a neuron can have several inputs. The inputs $p_1, p_2, ..., p_R$ have the corresponded weights $w_{1,1}, w_{1,2}...., w_{1,R}$ of the weight matrix W. Figure 6.6 shows the architecture of a neuron with R inputs in matrix form. Therefore, $n = w_{1,1}p_1 + w_{1,2}p_2 + ... + w_{1,R}p_R + b$. Here **p** is a vector with length R $(R \times 1)$ and **W** is a $1 \times R$ matrix.
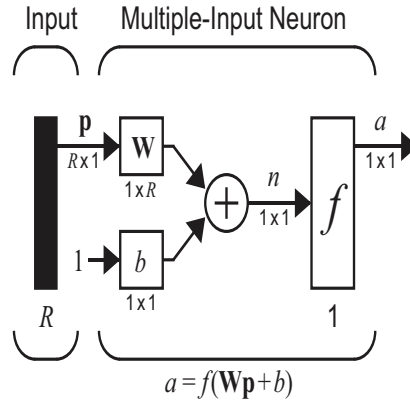
Figure 6.6: Neuron with R inputs [7].

The scalar neuron output is a $f(n)$. Notably only one neuron, with many inputs, is not sufficient to approximate the function. Figure 6.7 shows a network with S neurons and R inputs.

The input vector elements which enter to the network with S neurons will be multiplied by the weight matrix **W**:

$$
\mathbf{W} = \begin{pmatrix} w_{1,1} & w_{1,2} & \cdots & w_{1,R} \\ w_{2,1} & w_{2,2} & \cdots & w_{2,R} \\ \vdots & \vdots & \vdots & \vdots \\ w_{S,1} & w_{S,2} & \cdots & w_{S,R} \end{pmatrix}
\tag{6.10}
$$
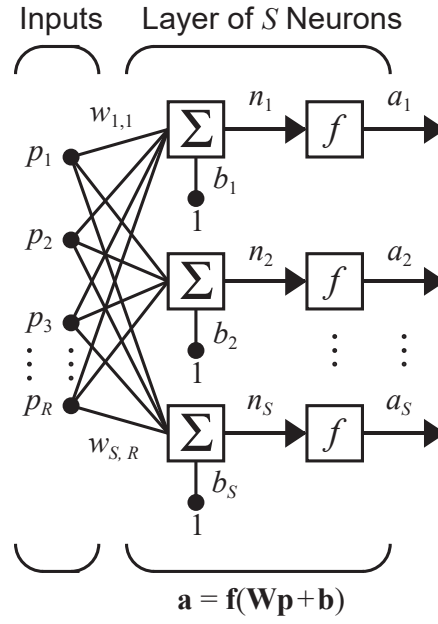
Figure 6.7: Layer of S Neurons [7].

6.3.4 Multiple Layers of Neurons

When the unknown function is not linear, more than one layer in the network is needed. Therefore, multiple layers of neurons are used. In the multiple layers network, each layer has a weight matrix $\mathbf{W}$, bias vector $\mathbf{b}$, net input vector $\mathbf{n}$, and output vector $\mathbf{a}$. Therefore, the weight matrix for the first layer is presented as $\mathbf{W}^1$ and for the second layer is written as $\mathbf{W}^2$. The last layer is called an output layer and the other layers are called hidden layers. Figure 6.8 shows a network with three layers. There are two hidden layers (layer 1 and 2) and an output layer (layer 3). The output of the third layer is defined :

$$\mathbf{a}^3 = \mathbf{f}^3(\mathbf{W}^3\mathbf{f}^2(\mathbf{W}^2\mathbf{f}^1(\mathbf{W}^1\mathbf{p} + \mathbf{b}^1) + \mathbf{b}^2) + \mathbf{b}^3).$$

6.3.5 Backpropagation

As shown in section 6.3.4, the output of each layer is the input of the next layer. The general equation which describes the forward calculation of layer M (last layer) is in Equation 6.11.

94
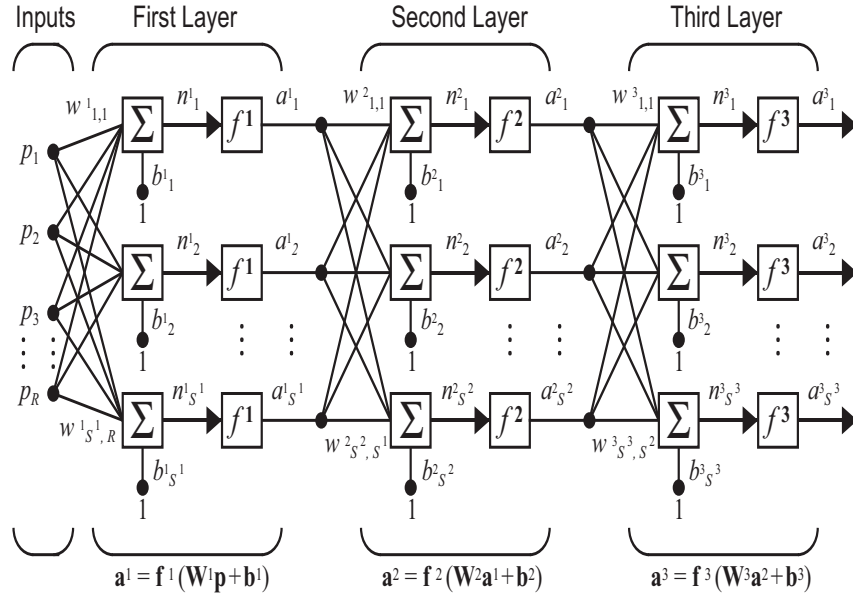
Figure 6.8: Three-layer Network [7].

$$\mathbf{a}^{m+1} = \mathbf{f}^{m+1}(\mathbf{W}^{m+1} \times (\mathbf{a}^{m+1} + \mathbf{b}^{m+1})) \qquad (6.11)$$

Where $m = 0, 1, ...M - 1$. The neurons in the first layer receive external inputs:

$$\mathbf{a}^0 = \mathbf{p}, \qquad (6.12)$$

and the outputs of the neurons in the last layer are considered the network outputs:

$$\mathbf{a} = \mathbf{a}^M. \qquad (6.13)$$

The multi-layer network is well known as a universal approximator. A procedure for adjusting the weights and biases of a network (also called a training algorithm) to have the best approximate function is an important key that will be discussed in this section. In many Neural Network applications, training set consists of a set of Q input vectors $[p_1, p_2, ...p_q]$ and corresponding target vectors $[t_1, t_2, ...t_q]$. The training rules are used for adjusting

weights and biases when there are some targets are called Supervised Rules. However, there are some applications that the target is unknown such as recurrent network.

In this section, we introduced the back propagation algorithm which is an efficient way to calculate the gradient of the performance function with respect to the weight and biases of the network, which is needed for network training.

6.3.5.1 Backpropagation Algorithm

Optimization is one of the fundamental concepts that needs to be explained before describing the details of the backpropagation algorithm. Generally, optimization is a way to find the value of x to minimize $F(x)$. In order to minimize F(x), the derivative of F(x)(gradient) should be negative which means function decreases to find a minimum [7].

$$F(\mathbf{x_{k+1}}) = F(\mathbf{x_k} + \Delta \mathbf{x_k}) \approx F(\mathbf{x_k}) + \mathbf{g_k^T} \Delta \mathbf{x_k}, \tag{6.14}$$

where g_k defined as gradient of $F(x)$ in x_k. In order to find minimize of a function, we should update the x_{k+1} in each iteration by equation:

$$\mathbf{x_{k+1}} = \mathbf{x_k} - \alpha_\mathbf{k} \mathbf{p_k}. \tag{6.15}$$

Therefore, a steepest descent is a common optimization method, which can be used in training algorithm. Steepest descent defines when $\mathbf{p_k} = -\mathbf{g_k}$. Steepest descent can find a local minion if the value of α is enough small. However, there are some other optimization methods which can be used as well. When we used several layers with multiple neurons in each layer (defines as Multi-layer Perceptron or MLP) which are shown in Figure 6.8, the output of each layer is input of the next layer this network can be used as function approximator because there are not any feedback delays on that. For training a network with steepest descent algorithm, we assume a network with a set of inputs and target outputs $[(p_1,t_1),(p_2,t_2),(p_3,t_3),....,(p_Q,t_Q)]$. The network trained untill the sum square errors

between the targets and the outputs minimize (converges to a local minimum of the performance function). Equation 6.16 shows the sum square error where $\mathbf{x}$ is a vector of weights and biases of the network.

$$F(\mathbf{x}) = \sum_{q=1}^{Q} \|e_q\|^2 = \sum_{q=1}^{Q} \|t_q - a_q\|^2 = \sum_{q=1}^{Q} (t_q - a_q)^T (t_q - a_q) = \sum_{q=1}^{Q} F_q(\mathbf{x}). \quad (6.16)$$

The gradient of $\mathbf{F}(\mathbf{x})$ with respect to weights and biases $\frac{\partial F_q}{\partial w_{i,j}^m}$ and $\frac{\partial F_q}{\partial b_i^m}$ need to be calculated by applying chain rules because of indirect relationship between weights and biases in the hidden layers. Equations 6.17 and 6.18 show the calculus of these derivatives:

$$\frac{\partial F_q}{\partial w_{i,j}^m} = \frac{\partial F_q}{\partial n_i^m} \times \frac{\partial n_i^m}{\partial w_{i,j}^m}, \quad (6.17)$$

$$\frac{\partial F_q}{\partial b_i^m} = \frac{\partial F_q}{\partial n_i^m} \times \frac{\partial n_i^m}{\partial b_i^m}. \quad (6.18)$$

The first term in Equations 6.17 and 6.18 defines as a sensitivity $s_i^m \equiv \frac{\partial F_q}{\partial n_i^m}$. In addition, the derivatives can be calculated as:

$$\frac{\partial F_q}{\partial w_{i,j}^m} = s_i^m a_j^{m-1}, \quad (6.19)$$

$$\frac{\partial F_q}{\partial b_i^m} = s_i^m. \quad (6.20)$$

The sensitivity at layer m should be calculated from the sensitivity at layer $m+1$. Therefore, we need to use another chain rule in order to calculate s_m. The relationship between two sensitivities can be defined by the Jacobian matrix.

$$\frac{\partial \mathbf{n}^{m+1}}{\partial \mathbf{n}^m} \equiv \begin{bmatrix} \frac{\partial n_1^{m+1}}{\partial n_1^m} & \frac{\partial n_1^{m+1}}{\partial n_2^m} & \cdots & \frac{\partial n_1^{m+1}}{\partial n_{S^m}^m} \\ \frac{\partial n_2^{m+1}}{\partial n_1^m} & \frac{\partial n_2^{m+1}}{\partial n_2^m} & \cdots & \frac{\partial n_2^{m+1}}{\partial n_{S^m}^m} \\ \vdots & \vdots & & \vdots \\ \frac{\partial n_{S^{m+1}}^{m+1}}{\partial n_1^m} & \frac{\partial n_{S^{m+1}}^{m+1}}{\partial n_2^m} & \cdots & \frac{\partial n_{S^{m+1}}^{m+1}}{\partial n_{S^m}^m} \end{bmatrix}, \quad (6.21)$$

$$\frac{\partial n_i^{m+1}}{\partial n_j^m} = \frac{\partial(\sum_{l=1}^{s^m} w_{i,l}^{m+1} a_l^m + b_i^{m+1})}{\partial n_j^m} = w_{i,j}^{m+1} \frac{\partial a_j^m}{\partial n_j^m} \tag{6.22}$$

$$= w_{i,j}^{m+1} \frac{\partial f^n(n_j^m)}{\partial n_j^m} = w_{i,j}^{m+1} \dot{f}^m(n_j^m).$$

Therefore, the sensitivity can be calculated as:

$$s^m = \frac{\partial \hat{F}}{\partial \mathbf{n}^m} = \left(\frac{\partial \mathbf{n}^{m+1}}{\partial \mathbf{n}^m}\right)^T \frac{\partial \hat{F}}{\partial \mathbf{n}^{m+1}} = \dot{\mathbf{F}}^m(\mathbf{n}^m)(\mathbf{W}^{m+1})^T \frac{\partial \hat{F}}{\partial \mathbf{n}^{m+1}} \tag{6.23}$$

$$= \dot{\mathbf{F}}^m(\mathbf{n}^m)(\mathbf{W}^{m+1})^T s^{m+1}.$$

After calculating the sensitivities, we need to calculate the gradient by using Equations 6.19, 6.20 and then, the weights and biases updated by using steepest descent algorithm (Equation 6.15). However, the steepest descent algorithm is slow in finding a global minimum. Therefore, we present a faster algorithm Levenberg-Marquardt (LM) algorithm to save time in the computation. LM algorithm is related to [7] Newton's method. Therefore, we start to describe briefly about Newton's method and then explain LM algorithm. The update equation in Newton method is:

$$\mathbf{x_{k+1}} = \mathbf{x_k} - \mathbf{A_k^{-1}} \mathbf{g_k}, \tag{6.24}$$

where A_k is a Hessian matrix and g_k is a gradient where the sum square error is:

$$\mathbf{F}(\mathbf{x}) = \sum_{i=1}^{N} e_i^2(\mathbf{x}) = \mathbf{e}^T(\mathbf{x})\mathbf{e}(\mathbf{x}), \tag{6.25}$$

and the gradient

$$\nabla \mathbf{F}(\mathbf{x}) = 2\mathbf{J}^T(\mathbf{x})\mathbf{e}(\mathbf{x}). \tag{6.26}$$

The Jacobian matrix is defined as:

$$\mathbf{J(x)} = \begin{bmatrix} \frac{\partial e_1(\mathbf{x})}{\partial x_1} & \frac{\partial e_1(\mathbf{x})}{\partial x_2} & \cdots & \frac{\partial e_1(\mathbf{x})}{\partial x_n} \\ \frac{\partial e_2(\mathbf{x})}{\partial x_1} & \frac{\partial e_2(\mathbf{x})}{\partial x_2} & \cdots & \frac{\partial e_2(\mathbf{x})}{\partial x_n} \\ \vdots & \vdots & & \vdots \\ \frac{\partial e_N(\mathbf{x})}{\partial x_1} & \frac{\partial e_N(\mathbf{x})}{\partial x_2} & \cdots & \frac{\partial e_N(\mathbf{x})}{\partial x_n} \end{bmatrix}. \tag{6.27}$$

The Hessian matrix can be defined as:

$$\nabla^2 \mathbf{F(x)} = 2\mathbf{J}^T(\mathbf{x})\mathbf{J(x)} + 2\mathbf{S(x)}, \tag{6.28}$$

and

$$\mathbf{S(x)} = \sum_{i=1}^{N} e_i(\mathbf{x})\nabla^2 e_i(\mathbf{x}). \tag{6.29}$$

If $\mathbf{S(x)}$ is assumed small, the Hessain matrix can be written as:

$$\nabla^2 \mathbf{F(x)} = 2\mathbf{J}^T(\mathbf{x})\mathbf{J(x)}, \tag{6.30}$$

Therefore, we can define Newton method update equation by substituting equations 6.26 and 6.30 into equation 6.24 as:

$$\mathbf{x}_{k+1} = \mathbf{x}_k - [\mathbf{J}^T(\mathbf{x}_k)\mathbf{J}(\mathbf{x}_k)]^{-1}\mathbf{J}^T(\mathbf{x}_k)\mathbf{e}(\mathbf{x}_k). \tag{6.31}$$

The only problem in this method is the matrix $\mathbf{H} = \mathbf{J}^T\mathbf{J}$ sometimes is not invertible. This problem can be addressed by a small modification to approximate the Hessian matrix:

$$\mathbf{G} = \mathbf{H} + \mu\mathbf{I}, \tag{6.32}$$

The Levenberg-Marquardt algorithm [7] can be defined as:
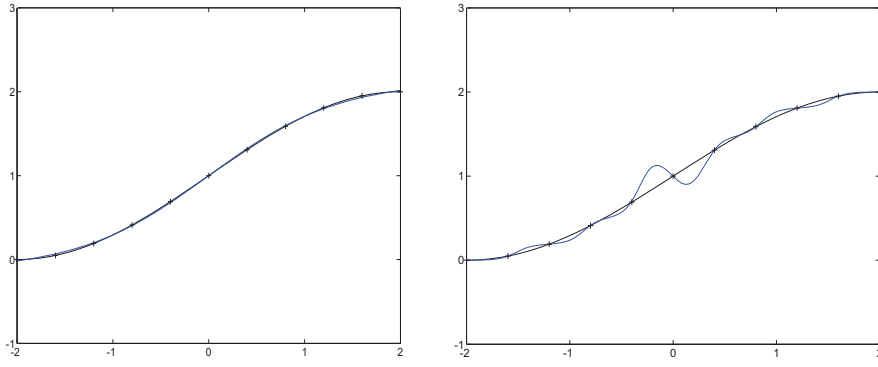
(a) Approximation by 1-2-1 network [7].   (b) Approximation by 1-9-1 network [7].

Figure 6.9: Effects of number of parameters in function approximation.

$$\Delta \mathbf{x}_k = - \left[\mathbf{J}^T(\mathbf{x}_k)\mathbf{J}(\mathbf{x}_k) + \mu_k \mathbf{I} \right]^{-1} \mathbf{J}^T(\mathbf{x}_k)\mathbf{e}(\mathbf{x}_k). \tag{6.33}$$

The important characterization of the LM algorithm is when μ_k becomes large (less than 10^{10} [7]), it becomes effectively steepest descent with a small learning rate. In this way, F(x) definitely decreases if μ is made large enough. In the next section, we will explain another problem (overfitting) that network can de faced during training the weights and biases.

6.3.6   Generalization

In most cases the multilayer network is trained with a finite number of examples of proper network behavior with Q of inputs and targets. This training set is normally representative of a much larger class of possible input/output pairs. It is important that the network generalize what it has learned from the total population. For a network to be able to generalize, it should have fewer parameters than data points in the training set. Therefore, we need to choose a network which is fitted to the problem.

If we use a bigger network (more number of layers), we will have overfitting. We explain the overfitting by an example of a network with two layers. Figure 6.9(a) shows the response of a network with two neurons in the first layer and one neuron in the second layer

100

to an input (1-2-1) and Figure 6.9(b) shows the response of a network with nine neurons in the first layer and one neuron in the second layer (1-9-1). Each + marks a point from training set.

It can be seen that the network in Figure 6.9(a) has accurate results in approximating the function while the network in Figure 6.9(b) fits the training points but does not have an accurate response for data outside the training set. This network does not generalize well. In order to improve generalization, we attempt to restrict the magnitude of weights by using Regularization.

6.3.6.1   Regularization

Regularization is used to avoid overfitting the network [51]. For this method, we modify the sum squared error performance index Equation 6.34 and add a term which forces the approximated function to be smooth.

$$\mathbf{F(x)} = E_D = \sum_{q=1}^{Q} (t_q - e_q^T)(t_q - e_q). \tag{6.34}$$

The Regularized performance index can be written as follows:

$$\mathbf{F(x)} = \alpha E_D + \beta E_w = \beta \sum_{q=1}^{Q} (t_q - e_q^T)(t_q - e_q) + \alpha \sum_{i=1}^{n} x_i^2, \tag{6.35}$$

Where the ratio $\frac{\alpha}{\beta}$ controls the effective complexity of the network solution. The larger this ratio is, the smoother the network response. There are several methods which can be used in selection of the regularization parameter, but we focus on a Bayesian statistical framework. This framework starts with assumption that the network weights are random variables. In addition, it is necessary to calculate the Hessian matrix of $\mathbf{F(x)}$ at the minimum point. We applied the Gauss-Newton approximation to calculate Hessian matrix and used LM optimization to locate the minimum point. The steps of the Baysian Regularization Algorithm are as follows [52]:

1− Initialize α, β and the weights. The weights are initialized randomly, then E_D and E_w are computed. Set $\gamma = n$ and compute α, β using following equations:

$$\alpha^{MP} = \frac{\gamma}{2E_w(\mathbf{x}^{MP})}, \tag{6.36}$$

$$\beta^{MP} = \frac{N - \gamma}{2E_D(\mathbf{x}^{MP})}. \tag{6.37}$$

2− Take one step of the Levenberg-Marquardt algorithm toward minimizing the objective function $\mathbf{F(x)} = \alpha E_D + \beta E_w$.

3− Compute the effective number of parameters $\gamma = n - 2\alpha tr(\mathbf{H}^{-1})$ which shows the effective number of weights and biases that we used in training of network, making use of the Gauss- Newton approximation to the Hessian available in LM training algorithm:

$$\mathbf{H} = \nabla^2 \mathbf{F(x)} \approx 2\beta \mathbf{J}^T \mathbf{J} + 2\alpha \mathbf{I}_n, \tag{6.38}$$

4− Compute new estimates for the regularization parameters α, β from Equation 6.36 and Equation 6.37.

5− Now iterate steps 2 through 4 until convergence.

This algorithm can help us to improve generalization in the network.

6.3.6.2 Committee of Networks

It has been shown that the performance achieved by a single neural network can be improved by using a committee of networks (also is called a group of networks) . Each network in the committee is trained with a slightly different training/testing division of the data. Also, each network is trained with different random initial weights. After the networks have been trained, the same input is applied to each network in the committee, and the outputs of all of the networks are averaged together to form the committee response [53].

102

The number of networks (N_n) and the number of neurons used in the hidden layer of the network (S^1) are architecture settings that need to be determined through experiment. In the results section of the work we will describe the process of selecting N_n and S^1.

6.3.7 Monte Carlo cross-validation

The performance of a network, or a committee of networks, can be sensitive to the data division process. In order to better understand the robustness of the network and to develop confidence bounds on future network performance, we use Monte Carlo cross-validation. This method involves two sets of data divisions. First, 15% of the full original data set is randomly removed. The remaining data is used to create a committee of networks, as described in the previous section, where a further division of the data occurs for each committee member. After a committee is formed, the Root Mean Square Error (RMSE) and the Percent Error (PE) for the committee are computed on the 15% of the data that was originally removed. This process is repeated for a specified number of Monte Carlo trials, with data replaced after each selection. For our tests, 100 Monte Carlo trials were used.

After the Monte Carlo trials are complete, the mean and standard deviation of RMSE and PE can be computed (in addition to the R value). In this way, we can learn not only what level of error we can expect in the future, but also how much variation there will be. It would not be appropriate for any nonlinear regression application to report only a single accuracy level. Because results are very data dependent, it is important to provide error bars on any reported results.

Notably, that the 15% of the data that is randomly removed at each Monte Carlo trial is not used for training any of the committee members during that trial.

6.4 Results and Analysis

In this section, we train a committee of networks using Bayesian Regularization to find how much absorbing material should be used to produce a specific quality factor in a cavity

Top View
Absorbing Material positions
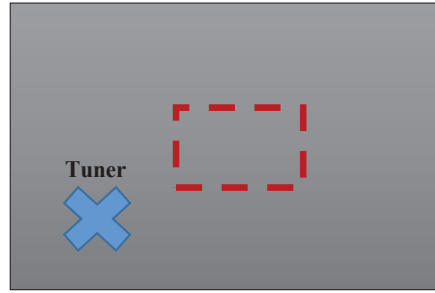
Figure 6.10: Topview of material spacing.

at different frequency bandwidths. Quality factor (Q) is measured by applying one port technique [10] and [23].

The dimension of the enclosure for our experiments is $0.25 \times 0.15 \times 0.3$ m^3. A z-fold tuner was used to stir the fields as described in chapter 4. Figures 5.1 and 6.10 show the test configuration and material spacing respectively. The reverberant environment starts with frequencies no lower than triple the cut-off frequency [10], which is 3 GHz for this enclosure. We chose center frequencies from 5.5 GHz to 11 GHz (in steps of 500 MHz) to be sure the cavity is over-moded. All measurements were performed using only one monopole antenna due to small dimension of the cavity [46].

We selected 10 different materials, which were all members of the silicon rubber family. The materials were cut in rectangular parallel piped sections and placed in the center of the cavity. We measured the time domain S_{11} at 50 tuner positions and calculated Q. The VNA collected $1,601$ data samples in each tuner position.

Table 6.1 shows the ranges of all input and output data that are provided from ARC Technology Co. As can be seen, 12 different frequencies were used, and ΔQ ranged from around 1 dB to 14.5 dB. The material thickness has a small range, but the surface area range is more significant. We used 55 different surface areas and 25 different thicknesses. Some of the dimensions were the same for several materials. As shown in the table by having

Table 6.1: Range of Input/ Output data

Input/Output	Range
Frequency	5.5 to 11 (GHz) (step 500 MHz)
ΔQ	0.9958 to 14.36 (dB)
ε_r'	9.9880 to 308.9860
ε_r''	0.0567 to 51.5450
μ_r'	0.0870 to 2.7936
μ_r''	0.1040 to 2.8007
Thickness of materials	0.254 to 4.4 (mm)
Surface area of materials	4200 to 51300 (mm^2)

frequency, type of material and ΔQ, approximated function should be able to estimate the required surface and thickness of the material. We considered two options for estimating the appropriate material thickness and surface area. The first option was to use one committee, with two outputs, to estimate both thickness and surface area simultaneously. The second option was to use two different committees -one to estimate thickness, and the other to estimate surface area. For this work, we chose the two-layer network shown in Figure 6.11. Initial testing demonstrated that we could achieve more accurate results by using two committees. The results summarized below were all for the two-committee solution. There are two committee settings that need to be determined through experiment: the number of networks in the committee, N_n, and the number of neurons in the first layer of the networks, S^1. In our experiments, we tested 10, 20 and 100 as values for N_n and 5, 10, 15 and 20 as values for S^1.

Tables 6.2 to 6.7 show the results for surface area and thickness estimation with all combinations of these values for N_n and S^1. The first column shows the number of committee members. The second column shows the number of neurons in the hidden (first) layer.
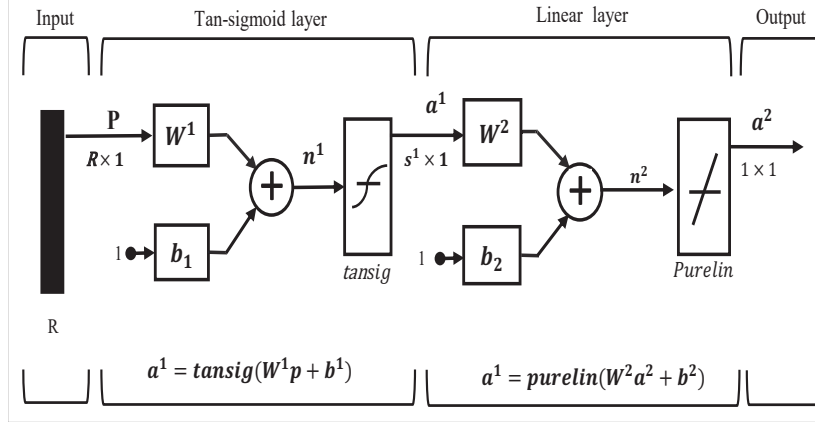
Figure 6.11: Two layer Network.

The next two columns show the average and standard deviation of the Percent Error on the testing sets over the 100 Monte Carlo trials. Finally, the last two columns show the average and standard deviation of the Root Mean Squared Error (RMSE) on the testing sets. Recall that the testing sets were not used in training any of the networks on the committee they were used to test.

Equation 6.39 shows how the RMSE was computed for the test set.

$$F(\mathbf{x}) = \sqrt{\frac{1}{M} \sum_{q=1}^{M} (t_q - a_q)^2}, \tag{6.39}$$

The chosen materials are from Laird and Arc Technology company with different properties. But, all of them are members of the silicon rubber group. The materials were cut in rectangular cube or square cube and placed in the center in the bottom of the cavity.

The inputs of each network include frequency range, delta quality factor and properties of materials, and the targets include surface and thickness of materials (one network for each). Because neural network results can be sensitive to the training set, we used Monte Carlo cross-validation to develop confidence levels on the results. For each Monte Carlo trial, 15% of the data was removed for testing. Then, for each network in the committee 85% of remaining data was randomly selected for training. Each committee member was trained with a slightly different data set and different initial weights. After each committee

Table 6.2: Surface result with 10 network committee

Number of Neurons in Hidden layer	Averaged testing Error(%)	Std.(%)	Averaged testing RMSE	Std. RMSE
5	2.5252	1.4774	3.3E-3	3.02E-4
7	2.7191	1.6038	3.3E-3	2.83E-4
10	2.3366	1.5056	3.1E-3	2.95E-4
15	1.9906	1.4201	3.0E-3	2.73E-4
20	2.1982	1.3804	3.1E-3	2.96E-4

Table 6.3: Surface result with 20 network committee

Number of Neurons in Hidden layer	Averaged testing Error(%)	Std.(%)	Averaged testing RMSE	Std. RMSE
5	2.7995	1.4129	3.3E-3	2.46E-04
7	2.4708	1.4626	3.3E-3	2.74E-04
10	2.5488	1.5156	3.2E-3	3.30E-04
15	1.9819	1.2976	3.0E-3	5.66E-04
20	1.8639	1.2241	3.0E-3	2.89E-04

was formed, errors were computed on the test set, which was not in the training process. We decided to use two individual networks one for surface and one for thickness. Tables 6.2 to 6.4 show the results for surface networks. The results are based on 100 monte carlo trails and 10, 20 and 100 networks per committee in each trial. The columns shows the number of neurons in the hidden layer (we have only two layers), percent error, standard deviation of percent error, root mean square error (RMSE) and standard deviation of RMSE.

For the network that predicts surface area, the best results are obtained with committees of 20 networks with 15 or 20 neurons in the hidden layer. The average percent error is about 2%, and the average R value is about 0.97. Tables 6.5 to 6.7 show the results for the networks that predict thickness. The best results for this case are found with 100 network

Table 6.4: Surface result with 100 network committee

Number of Neurons in Hidden layer	Averaged testing Error(%)	Std.(%)	Averaged testing RMSE	Std. RMSE
5	2.6766	1.4346	3.3E-3	2.55E-04
7	2.5830	1.5841	3.3E-3	2.82E-04
10	2.1383	1.2884	3.1E-3	2.80E-04
15	2.2102	1.3381	3.0E-3	2.55E-04
20	2.0635	1.3632	3.0E-3	2.91E-04

Table 6.5: Thickness result with 10 network committee

Number of Neurons in Hidden layer	Averaged testing Error(%)	Std.(%)	Averaged testing RMSE	Std. RMSE
5	10.201	4.3022	6.23E-04	6.79E-05
7	9.5660	3.8883	6.22E-04	7.60E-05
10	8.7619	4.5259	6.16E-04	7.11E-05
15	8.9555	4.7050	6.13E-04	7.24E-05
20	9.4179	4.7679	6.13E-04	7.90E-05

Table 6.6: Thickness result with 20 network committee

Number of Neurons in Hidden layer	Averaged testing Error(%)	Std.(%)	Averaged testing RMSE	Std. RMSE
5	9.4903	3.6876	6.30E-04	7.61E-05
7	8.8649	3.8229	6.11E-04	7.44E-05
10	8.8964	4.0517	6.33E-04	6.93E-05
15	8.6038	4.3529	6.27E-04	7.27E-05
20	9.3375	4.2974	6.18E-04	7.08E-05

Table 6.7: Thickness result with 100 network committee

Number of Neurons in Hidden layer	Averaged testing Error(%)	Std.(%)	Averaged testing RMSE	Std. RMSE
5	9.2459	4.6125	6.23E-04	6.74E-05
7	8.6516	4.2756	6.21E-04	7.16E-05
10	9.3128	4.1685	6.22E-04	6.77E-05
15	8.3594	4.1575	6.07E-04	6.94E-05
20	8.1132	4.4948	6.22E-04	7.90E-05

committees and 20 neurons in the hidden layer. The average percent error is about 8%, and the R value between network outputs and targets is about 0.85.

The best results in surface network is for a network which has 20 networks per committee and 15 and 20 neurons in the hidden layers. In thickness networks, the best results is for 100 network per committee with 20 neurons in the hidden layer.

6.5 Conclusion

We used committees of neural networks to estimate the required surface area and thickness of absorbing materials to achieve a specific quality factor inside a reverberation chamber. The networks used in the committees were two layer perceptron networks with hyperbolic tangent transfer functions in the first layer and linear transfer functions in the second layer. The individual networks were trained with Bayesian regularization to prevent overfitting. Monte Carlo cross-validation was used to investigate the robustness of the methods, and to provide error bars on the performance results. Separate committees were trained to estimate required surface area and thickness. Experiments were performed to determine the appropriate number of networks to use for each committee and the appropriate number of neurons to use in the hidden layer of each network. The testing results show that we can consistently achieve a less than 2% error on the required surface error and a less than 10%

error on the required thickness. To achieve improved results on thickness estimation, we need to collect more data at a finer thickness resolution. It should be noted that the trained neural network can be used to determine absorber dimensions for Q values that are not contained in the measured data. This means that the network interpolates between measured values.

CHAPTER 7

THE GENERALIZED EXTREME VALUE DISTRIBUTION vs.
REVERBERATION CHAMBERS' CHARACTERISTIC

In this chapter, we will begin in section 7.1 with a description of uniformity, using mean and standard deviation. The uniformity inside the reverberation chamber is analyzed by varying shape parameter (k) of the GEV distribution. The methodology to calculate the number of independent samples while the chamber is either unloaded or loaded is described and shown in section 7.2. In addition, the number of independent samples is assessed for various center frequencies. Finally, the comparison between the GEV distribution and the traditional method is shown in section 7.3. The advantages and disadvantages of both methods are discussed.

7.1   Statistical Description of The Uniformity Quantity

The field uniformity is another important factor inside a reverberation chamber that needs to be studied when we focus on the EM field inside a reverberation chamber. The field uniformity is useful to see if the reverberant environment is isotropic and homogenous [10]. The typical experimental method in the calculation of the uniformity has been shown in [10] and [14]. The uniformity can be computed in calibration process, by the measuring field in one component for eight different locations inside a reverberation chamber. In addition, Orjubin [14] showed the uniformity inside a reverberation chamber by using FEM method (numerical simulation). Uniformity can be estimated by S, the second-order characterization (mean value and variance), [14], which can be defined as:
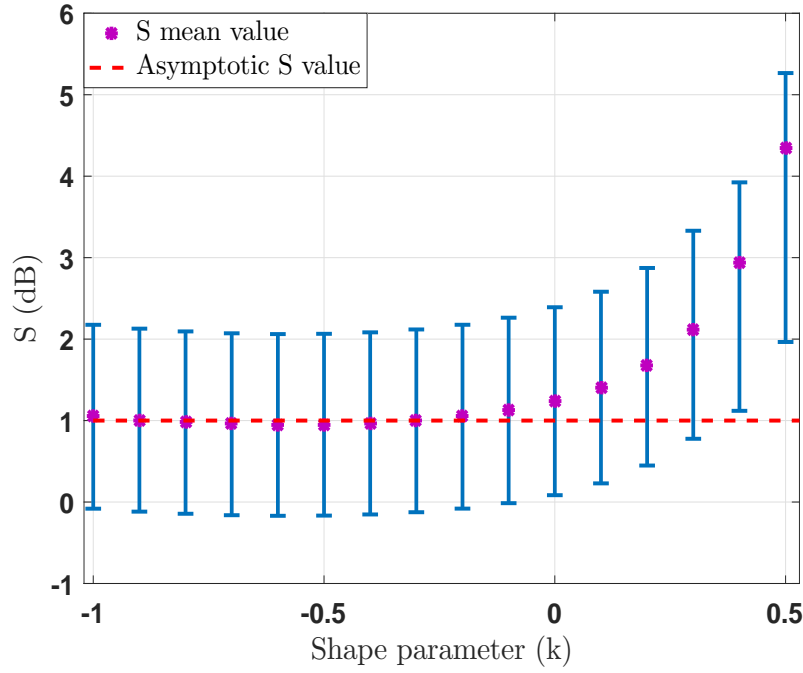
Figure 7.1: S statistics for a maximum field modeled by the GEV distribution. The vertical blue line shows extreme *S* and the dash line shows asymptotic *S* value.

$$S = 20\log(1 + \frac{\sigma_{E_Rmax}}{<E_{Rmax}>}), \tag{7.1}$$

where $<E_{Rmax}>$ and σ_{E_Rmax} are the mean and the variance of the maximum field in one component respectively. An alternative method is applying Monte Carlo simulation to compute the S statistics.

Notably, the GEV distribution can converge to three asymptotic distributions due to the value of shape parameter. Therefore, we tried to show the effects of varying shape parameter of the GEV distribution on the uniformity by using Monte Carlo simulation [14]. Figure 7.1 shows the relation between the shape parameter and the uniformity inside the nested chamber, when the maximum field is obtained by the GEV distribution from Monte Carlo simulation over $1,601$ samples. As can be seen, the asymptotic theoretical value is equal to the mean expected one when $-1 \le k < -0.2$. As indicated, S is changing when k moves to positive values and passes 3 dB criteria. The result is consistent with the results in

112

Table 7.1: Measurement parameters to collect samples

Parameter	Value
Frequency range	1-6 GHz
Number of frequency points	1601
VNA sweep time	8 Sec.
Paddle step size (Only vertical)	0.5 °

chapter 4 which means the uniformity passes the 3 dB criteria in under-moded regime. In other words, the GEV distribution converges to the Fréchet distribution while the k value is positive and this has happened when the chamber is in under-moded regime. This result has a good agreement with the above-mentioned work that Orjubin presented in [5]. However, the previous work used FDTD, while we used Monte Carlo simulation.

7.2 Number of Independent Samples

In a reverberation chamber, the number of independent (uncorrelated) samples can be assessed as the number of uncorrelated field samples (statistically) in the chamber at a specific frequency (for one complete rotation of the tuner). The number of independent samples (IS) is a function of frequency and the number of measured samples at each frequency. The estimation of independent samples is possible using the autocorrelation as discussed in chapter 2. At high frequencies, small change in the tuner position will result in electrically large changes in the boundary conditions due to a short wavelength, while at low frequencies small change in the boundary conditions, which corresponds to the large wavelength.

In order to assess the number of uncorrelated samples, measurements were performed for 750 vertical stirrer orientations (0.5° tuner step), and the autocorrelation was used for the frequency range of 1-6 GHz when the chamber is either unloaded or loaded with a

113
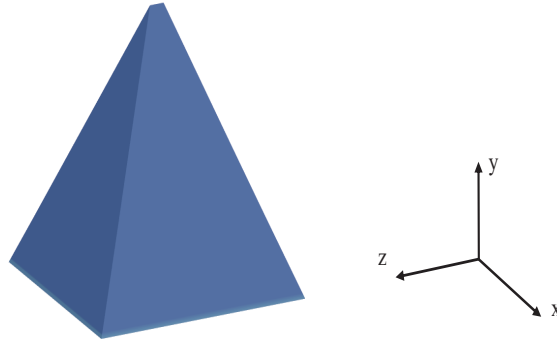
Figure 7.2: Absorbing material.

specific number of absorbing material. Key measurement parameters are summarized in Table 7.1. Effects of loading on the number of IS is interesting since loading is necessary during performance of communication testing inside a reverberation chamber. It has been shown [54] that loading can has a significant effect on the BER for digitally modulated signals with various data rates. We are able to estimate the number of uncorrelated samples that tuner steps are able to generate by using mechanical stirring. In other words, by applying autocorrelation at each specific frequency, we can define whether tuner was able to change the boundary conditions inside the chamber to generate the field distribution with a statistically significant variation. Therefore, the number of IS are considered as the samples that collected under statistically significant different conditions [55].

The material loading the chamber is FS-980 FERROSORB from ETS-Lindgren with a dimension of 30 cm by 30 cm by 10 cm. The materials were located at the corner of the chamber and the transmitter antenna was directed to the y axis of the absorber as shown in Figure 7.2.

Figures 7.3(a) and 7.3(b) show two examples of the autocorrelation for different frequencies. As shown, there is a complete correlation at no shift, and the autocorrelation function has a highest value of 1. For other shifts, the autocorrelation function has a magnitude between 0 and 1. The magnitude values near 1 show strong correlation and values near 0 show weak correlation.

114
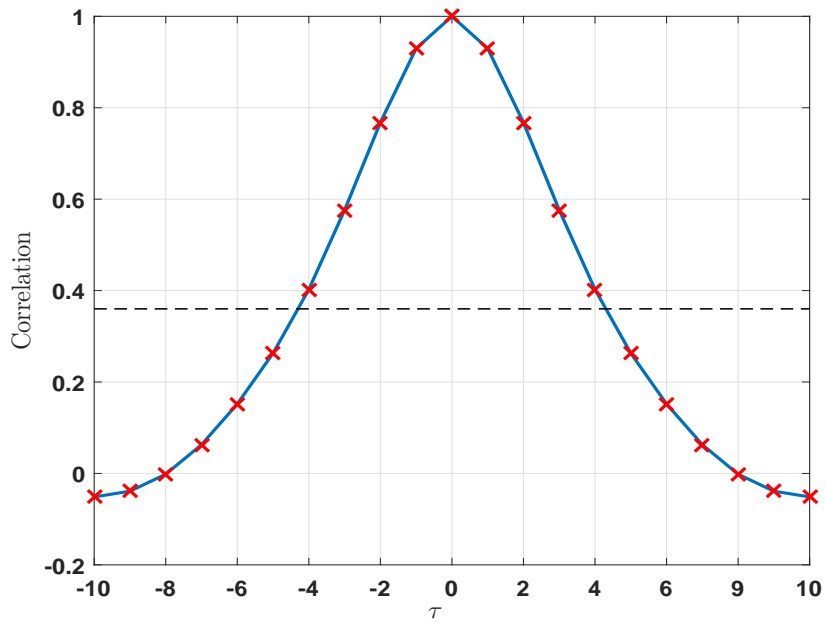
(a) Unloaded chamber at $f = 1$ GHz.
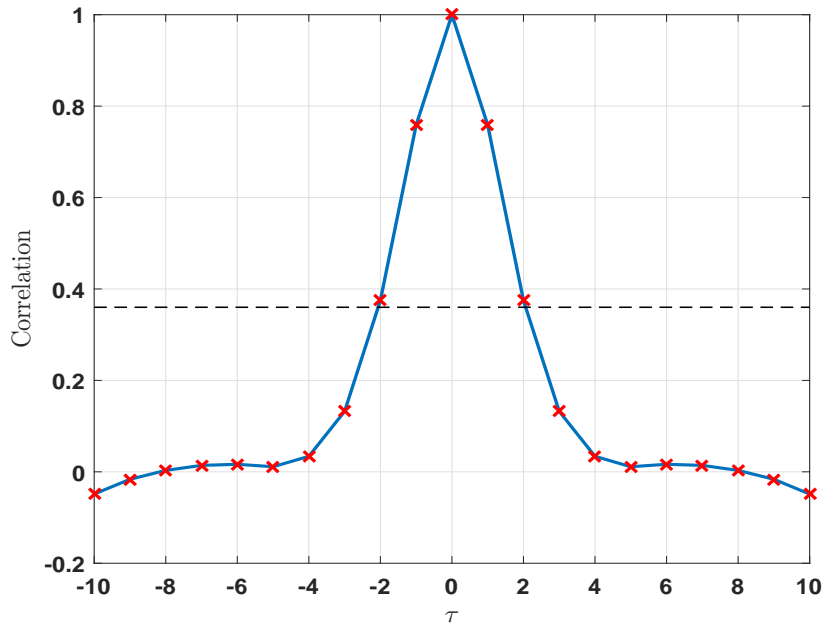
(b) Loaded chamber at $f = 3$ GHz.

Figure 7.3: Correlation between different paddle steps for a single vertical stirrer. Dash line shows the threshold $\frac{1}{e}$.

By using $\frac{1}{e}$ threshold (as described in chapter 2) over the total number of measured samples, the number of independent samples can be calculated. For the unloaded chamber at 1GHz frequency, the number of IS is calculated as:

$$\frac{750}{4.2} \approx 178, \tag{7.2}$$

and for the loaded chamber at 3 GHz, the number of IS is calculated as:

$$\frac{750}{2} \approx 375, \tag{7.3}$$

where the denominator shows the value corresponds to the threshold $\frac{1}{e}$ on x axis. Notably, by locating 8 pieces of materials, the Q of the chamber was higher than Q_{thr} and the field in this chamber can be still considered approximately uniform [45]. Table 7.2 shows the results of number of independent samples for various frequencies that were calculated by using autocorrelation. As indicated, the number of independent samples increased in higher frequency both when the chamber is unloaded or loaded. However, the number of independent samples decreased by loading the chamber due to the effects of absorbing materials on statistical description of the field inside the chamber [45]. This result is consistent with the results in [54]. But, the results are shown in terms of bit error rate (BER) and power delay profile (PDP), while we focused on the number of IS.

Table 7.2: Number of IS - unloaded chamber and loaded chamber

no.IS	Center Frequency		
	1 GHz	3 GHz	5 GHz
Unloaded	178	468	750
Loaded	150	375	576

7.3   Comparison to Traditional Method

The traditional method to find the probability density function of the minimum or maximum of the samples is based on the theory of order statistics in Appendix A. In this section, we will compare the traditional method with the GEV distribution, since it is possible to write the probability density function of the minimum and maximum with both methods. We will use the notation $[A]_N$ to indicate the maximum of N independent samples, each taken from distribution A, which is the parent distribution. The distribution of the maximum N samples is [56]:

$$f_{[A]_N} = N[F_A(x)]^{N-1} f_A(x).$$ (7.4)

The parent distribution is Rayleigh distribution for EM field in one component. The relation between the parameter of the distribution (scale) with mean (μ) which is defined as:

$$\sigma = \mu \sqrt{\frac{\pi}{2}},$$ (7.5)

By applying equation 7.5 to equation 7.4, we have:

$$f_{[A]_N} = Nx\frac{\pi}{2}(1 - exp(\frac{-\pi}{4}x^2))^{N-1} exp(\frac{-\pi}{4}x^2).$$ (7.6)

As indicated, the type of the parent distribution should be known before using the mentioned method. Figure 7.3 shows the comparison between the GEV distribution and the traditional method. As indicated, the GEV can converge to a fat tail distribution or an upper bounded distribution compared to the traditional method.

The comparison between the GEV distribution and the traditional method is as follows:

- The traditional method can *only* be applied when the parent distribution is known, while the GEV distribution is not limited to over-moded scenario. Therefore, by using the GEV distribution, the maximum distribution can be computed in different
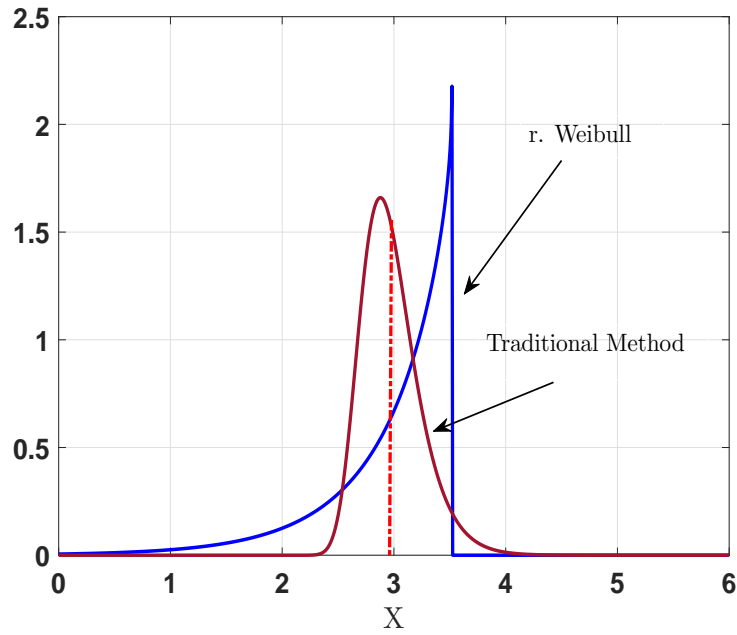
Figure 7.4: The GEV distribution vs. traditional method. Red dash line shows mean value.

cases where the parent distribution is not clear. In other words, the GEV distribution can model the maximum field level in the under-moded regime or when parent distribution is not known.

- The traditional method has only one parameter. Therefore, using the traditional method might be considered in over-moded regime for different EMC testings. However, the GEV distribution can provide three different asymptotic distributions with different type of tails (which can provide a potential upper bounded distribution function or a fat tail distribution) which is of interest in study of EMPAT frame work [31]. Additionally, the distribution has three parameters which are needed to be estimated [35].

- Both methods can be used to find the distribution of either maximum samples or minimum samples. The application of the minimum distribution will be the subject of future works in chapter 8.

7.4 Conclusion

The relation between the uniformity and the shape parameter of the GEV distribution was shown. It can be seen that the uniformity passed 3 dB criteria when the GEV distribution converged to the Fréchet distribution. The Fréchet distribution is representative of the maximum field level in under-moded regime as described in chapter 4. The measurement process to assess the number of independent samples was explained, while the chamber was unloaded and loaded with 8 pieces of absorbing materials. Overall, the number of independent samples increased as frequency increased. However, the number of independent samples decreased by loading the chamber. The traditional method to calculate the maximum field's level was explained and compared to the GEV distribution.

CHAPTER 8

CONCLUSION AND FUTURE WORK

8.1 Conclusion

Chapter 2 presented the statistical description for a properly stirred reverberation chamber. The real and imaginary parts of the electric field follow a Gaussian distribution and the field for one component follows a Rayleigh distribution. Two different methods, time domain and frequency domain, to calculate the Q were described. The required bandwidth to measure the Q in the time domain technique was explained, and the process of computing the number of independent samples inside the chamber with both mechanical stirring and frequency stirring was presented. The effects of different locations, working volume or near chamber walls, of the absorbing materials on Q reduction inside the reverberation chamber were shown. Additionally, the effects of shape of absorbing materials on the quality factor while they are located inside the working volume or surface area were discussed. Different types of measurement inside reverberation chambers were explained. We emphasized the maximum field level, since mode stirring inside the EUT causes that all of components reach maximum fields in immunity testing, which are a critical step in product development.

In chapter 3, the Generalized Extreme Value distribution was introduced. The distribution can converge to three different asymptotic distributions with different tails (an upper bounded or a fat tail). The distribution has three parameters: location, scale and shape. Maximum likelihood was presented as an unbiased linear estimator which can be used to estimate the parameters in the GEV distribution by applying a simplex optimization. The GEV distribution was applied to model the maximum field level for different apertures in

over-moded regime, for a frequency range 5-5.1 GHz, by applying mechanical stirring, spatial sampling and using the concept of coherent bandwidth. There was a good agreement between parametric and non-parametric plots and it was shown that the scalable results can be used in EMC/V testing due to the restriction in the test equipment and facilities.

The GEV can be used to describe the maximum-sample statistics obtained from any parent distribution. It is therefore applicable to the field samples where the parent distribution is not known, such as when the reverberation chamber or EUT box is under-moded, or the fields are not well stirred. It can therefore be used for different coupling aperture dimensions or configurations, changing cavity quality factors of the enclosure and arbitrary frequency range. As a novelty, this property of the GEV distribution was validated experimentally inside the nested chamber in chapter 4. Mechanical stirring was applied both within the reverberation chamber ("external stirring") and within the EUT box ("internal stirring") to generate numerous samples for estimation of the GEV parameters. Notably, the advantage of the external mechanical stirring is that all excitation fields to which the EUT enclosure is exposed are taken from the same chi distribution, whose statistics are well understood. The AD test was applied to check the Rayleigh distribution for the samples at each frequency step. As indicated, the samples from the external stirring followed a Rayleigh distribution. However, placing a tuner inside the EUT box changed the configuration of the EUT box and the generated samples followed a non-Rayleigh distribution. Since the box was over-moded at frequencies above 2.7 GHz, the environment inside the box was divided in two different regimes, over-moded and under-moded. The GEV distribution was applied to model the maximum field level in both regimes. The GEV distribution also was used on the samples while the EUT box was covered with two different apertures, small and large (considering shielding effectiveness). Consistent with the numerical simulation results from Orjubin and Gradoni et *al.*, the samples converged to the r. Weibull distribution (a potential bounded distribution) in the over-moded regime and to the Fréchet distribution (a fat tail distribution) for the under-moded regime. The results can be used in study of

EMPAT framework, where the traditional method is not applicable. However, when there are few modes inside the box, the distribution did not model reasonably. Additionally, the good agreement between theory and experiment is of interest in the study of physical properties of complex EM cavities. As a novelty, the uncertainties inherent also were calculated, which were required for the statistical modeling inside EM complex cavities.

Loading the EUT box is representative of electronic devices inside the reverberant environment. As a novelty, the GEV distribution was validated at the cases that the EUT box was loaded by the absorbing materials in chapter 5. The quality factor (Q) is a critical parameter for reverberation chambers analysis. In this chapter, the EUT box was loaded by absorbing material and the GEV distribution was applied to show the maximum field level for both under-moded and over-moded regimes. The results from parametrically and non-parametrically estimation had a good agreement. In conclusion, for the over-moded regime regardless the dimension of the aperture, the GEV distribution converged to the r. Weibull distribution. However, for the under-moded regime, the result was dependent on the aperture dimensions. By using a small aperture, the results converge to the Fréchet distribution. By contrast, the large aperture dimension allowed coupling between the reverberant environment and the EUT box.

In general, we test different dimensions or number of absorbing materials inside an enclosure to achieve a required quality factor inside an enclosure. If the absorption in not sufficient, we will change the dimension of absorbing material. As an alternative to this method, we used a neural network to compute the required absorbing material dimensions inside the EUT box to have a specific amount of quality factor in chapter 6. As a novelty, multi layers perceptron (MLP) as a function approximator was trained to minimize mean squared error between the network output and target output. A committee of networks was presented in order to improve the performance of the network. Monte Carlo cross validation was also used to understand the robustness of the network by dividing the data to 85% of full original data for training and 15% of the original data for testing the accuracy

of the network. Notably, 15% of the data were chosen randomly at each Monte Carlo trial and did not use for training the network. The results showed that we had achieved less than 2 % error on the required surface by using 20 networks per committee and less than 10 % error on the required thickness by using 100 networks per committee.

In chapter 7, the uniformity inside reverberation chamber was presented. Shape parameter value plays key role in the GEV distribution. As a novelty, Monte Carlo simulation was used to show the effects of varying the shape parameter on the uniformity inside the reverberation chamber. We observed that the S statistics passed 3 dB criteria when the shape parameter moved toward a positive value (followed the Fréchet distribution). The methodology to calculate the number of independent samples was investigated. The number of independent samples was calculated for three different center frequencies, while the chamber was both unloaded and loaded. It was shown that the number of independent samples increased in higher frequencies irrespective of the loading conditions. Finally, the GEV distribution and the traditional method were compared. The advantages and disadvantages of each method were discussed.

8.2 Future Work

In recent decades, wireless systems testing has been presented as an important issue. In fact, manufacturers of wireless systems need a reliable, controllable and repeatable facility for various measurements. However, the wireless devices should be tested for a wide range of environmental conditions from strong direct coupling to pure Rayleigh environment, and reverberation chambers have the capability of mimicing any arbitrary path environment. The statistics of the fields can usually be obtained, by rotating a tuner inside a reverberation chamber.

In this work, we presented the GEV distribution to model the maximum fields directly without *a priori* knowledge about the parent distribution. This was experimentally validated in a nested chamber while the EUT box had a tuner inside and made a non-Rayleigh

distribution. However, the GEV distribution could also be used to find the minimum distribution as well.

It has been shown [57] that the statistics of the EM field corresponds to the outage in a wireless communication, which usually occurred by fading. The fading can happen due to a destructive EM field (usually called a deep fade) in multipath propagation from multiple reflections, diffractions or etc. as part of the propagation process. Fading is a physical phenomena that is known as a source of malfunctioning in communication links. This is similar to the breakdown that happens when electronic devices pass the maximum EM field threshold. Reverberant environment can achieve Rayleigh or Rician distribution by having indirect or direct coupling (changing the reverberation chamber's characterization or the antenna configurations). Therefore, it is possible to simulate the real behavior of communication channels or wireless devices inside the chamber.

A wireless channel sends a transmitter signal with required information by using a digital (more common) or analogue modulation. However, noise or fading can change the signal to noise ratio (SNR) to a small value and increase the bit errors resulting in loss of the communication. Therefore, it is interesting to use the GEV distribution to model a minimum distribution for fading. Gradoni et *al.* [58] has shown theoretically the minimum distribution to model fading. However, the experimental validation still is needed to be performed. This can be started in over-moded regime inside a reverberation chamber, which can be considered to mimic a multipath fading in a wireless channel. In this case, the GEV distribution converged to reverse Gumbel distribution, reverse Fréchet distribution and Weibull distribution as follows:

$$F_1(x) = 1 - \exp(-\exp(\frac{-x-m}{s})), \quad \text{for all } x, \quad \textit{r. Gumbel} \tag{8.1}$$

$$F_2(x) = \begin{cases} 1 - \exp(-\frac{(x-m)}{s})^k, & \text{if } x > m \\ 1, & \text{otherwise} \end{cases} \quad \textit{r. Fréchet} \tag{8.2}$$

$$F_3(x) = \begin{cases} 1 - \exp(-\frac{(m-x)}{s})^k, & \text{if } x \leq m \\ 0, & \text{otherwise} \end{cases} \quad \textit{Weibull} \tag{8.3}$$

In addition, a reverberation chamber can be used to simulate different Rician multipath environments. But, not all of multipath environments follow Rician distribution [59] such as mixing both scattering and direct coupling components inside reverberation chamber. In the mentioned environment, the direct coupling components have difference Doppler shifts. A topic of interest for future research will likely be showing a minimum distribution of the fading in these environments by applying the GEV distribution.

REFERENCES

[1] C. E. Hager, J. D. Rison, and G. B. Tait, "Electromagnetic probability-of-effect assessment tool for high-power susceptibility testing," *IEEE Trans. On Electromagn. Compat.*, vol. 58, no. 4, August 2016.

[2] C. Bruns, "Three dimensional simulation and experimental verification of a reverberation chamber," Dissertation, University of Fridericiana Karlsruhe (TH), May 2005.

[3] Yuhui He and Andrew C. Marvin, "Aspects of field statistics inside nested frequency stirred reverberation chambers," *IEEE International Symposium on Electromagnetic Compatibility, Austin, TX, USA*, August 2009.

[4] Paul G. Bremner, Gabriel Vazquez, Dawn H.Trout, and Daniel J. Christiano, "Canonical statistical model for maximum expected immission of wire conductor in an aperture enclosure," *IEEE International Symposium on Electromagnetic Compatibility, Ottawa, CA*, pp. 758–763, August 2016.

[5] G. Orjubin, "Maximum Field inside a Reverberation Chamber Modeled by the Generalized Extreme Value Distribution," *IEEE Trans. On Electromagn. Compat.*, vol. 98, no. 1, pp. 104–113, February 2007.

[6] Kurtosis as peakedness, 1905–2014. r.i.p. the american statistician 68(3): 191–195. [Online]. Available: http://www.ncbi.nlm.nih.gov/pmc/articles/PMC4321753/

[7] M. Hagan, H. Demuth, M. H. Beale, and O. D. Jesus, *Neural Network Design, 2nd Edition*. CreateSpace, 2014.

[8] H. P. Gavin, "Nelder Mead algorithm in two dimensions," *Department of Civil and Environmental Engineering Duke University*, 2016.

[9] C. R. Paul, *Introduction to Electromagnetic Compatibility*. New York, NY: John Wiley and Sons, 1992.

[10] IEC, "Electromagnetic compatibility (EMC) – part 4-21: Testing and measurement techniques – reverberation chamber test methods," Phillips Airforce Laboratory, Kirtland Airforce Base, International Electrotechnical Commission, 3, rue de Varemb´e, Case postale 131, CH-1211 Geneve 20, Switzerland,IEC 61000-4-21, Technical Report PL-TR 91-1036, ADA 243551, 2003.

[11] J. S. Hong, "Electrical Mode Stirring in Reverberating Chamber by Reactively Loaded Antennas," *IEEE Trans. On Electromagn. Compat.*, vol. 29, no. 19, November 2007.

[12] Carlo Monteverde, Galen H. Koepke, Christopher L. Holloway, John M. Ladbury, David A. Hill, Valter Mariani Primiani, and Paola Russo, "Source Stirring Technique for Reverberation Chambers, Experimental Investigation," *IEEE International Symposium on Electromagnetic Compatibility, Hamburg, Germany*, September 2008.

[13] T.Lehman and G.J.Freyer, "Characterization of The Maximum Test Level in a Reverberation Chamber." IEEE International Symposium on Electromagnetic Compatibility , Austin, Texas, USA, August 1997.

[14] G. Orjubin, E. Richalot, S. Mengue, and O. Picon, "Statistical model of an undermoded reverberation chamber," *IEEE Transaction On Electromagnetic Compatability*, vol. 48, no. 1, p. 248–251, Feburary 2006.

[15] L. Arnaut, "Compound exponential distributions for undermoded reverberation chambers," *IEEE Transaction On Electromagnetic Compatability*, vol. 44, no. 3, pp. 442–457, November 2002.

[16] C. F. Bunting, "Shielding Effectiveness in a Two-Dimensional Reverberation Chamber Using Finite-Element Techniques," *IEEE Transaction on Electromagnetics Compatibility*, vol. 45, no. 3, pp. 548– 552, August 2003.

[17] C. L. Holloway, D. A. Hill, M. Sandroni, J. M. Ladbury, J. Coder, G. Koepke, A. C. Marvin, and Y. He, "Use of Reverberation Chambers to Determine the Shielding Effectiveness of Physically Small, Electrically Large Enclosures and Cavities," *IEEE Trans. On Electromagn. Compat.*, vol. 50, no. 4, November.

[18] T. A. Loughry, "Frequency stirring: An alternative approach to mechanical mode-stirring for the conduct of electromagnetic susceptibility testing," Phillips Airforce Laboratory, Kirtland Airforce Base, Albuquerque, NM, Technical Report PL-TR 91-1036, ADA 243551, November 1991.

[19] D. A. Hill, "Plane Wave Integral Representation for Fields in Reverberation Chambers," *IEEE Transaction on Electromagnetics Compatibility*, vol. 40, no. 3, pp. 209– 217, August 1998.

[20] Endegena Assefa, James C.West, Vignesh Rajamani, and Charles F. Bunting, "Numerical Study of Currents Induced on a Partially Shielded Wire Within an Ideal Reverberation Test Chamber," *IEEE International Symposium on Electromagnetic Compatibility, Pittsburgh, PA, USA*, pp. 150– 155, August 2012.

[21] M. L. Crawford and G. H. Koepke, "Design, evaluation, and use of a reverberation chamber for performing electromagnetic susceptibility/vulnerability measurements," National Bureau of Standards (NBS), Technical Report 1092, 1986.

[22] IEEE, "IEEE standard dictionary of electrical and electronics terms," New York, NY, John Wiley and Sons, Tech. Rep., 1972.

[23] Neda Nourshamsi, J. C. West, and C. F. Bunting, "Required bandwidth for time-domain measurement of the quality factor of reverberation chambers," *IEEE Inter-*

national *Symposium on Electromagnetic Compatibility, National Harbor, MD, USA*, August 2017.

[24] R. E. Richardson, "Reverberent microwave propagation," Naval Surface Warefare Center-Dahlgren Division, Dahlgren, Virginia,$22448 - 5100$, Technical Report $NSWCDD/TR - 08/127$, 2008.

[25] Kent Madsen, Paul Hallbjorner, and Charlie Orlenius, "Models for the Number of Independent Samples in Reverberation Chamber Measurements With Mechanical, Frequency, and Combined Stirring," *IEEE Antenna and wireless propagation letters*, vol. 3, no. 1, pp. 48–51, February 2004.

[26] C. L. Holloway, Haider A. Shah, Ryan J. Pirkl, Kate A. Remley, David A. Hill, and John Ladbury, "Early Time Behavior in Reverberation Chambers and Its Effect on the Relationships Between Coherence Bandwidth, Chamber Decay Time, RMS Delay Spread, and the Chamber Buildup Time," *IEEE Transactions on Electromagnetic Compatibility*, vol. 54, no. 4, pp. 714–725, Augest 2012.

[27] S. Kildal, Charlie Orlenius, and Jan Carlsson, "OTA Testing in Multipath of Antennas and Wireless Devices with MIMO and OFDM," *Proceedings of the IEEE*, vol. 100, no. 7, pp. 2145–2157, September 2012.

[28] Jason B. Coder, John Ladbury, Christopher L. Holloway, and Kate A. Remley, "Examining the True Effectiveness of Loading a Reverberation Chamber," *IEEE International Symposium on Electromagnetic Compatibility, Fort Lauderdale, FL, USA*, July 2010.

[29] Neda Nourshamsi and Charles F. Bunting, "Impact of the shape of lossy materials inside a reverberation chamber," *IEEE International Symposium on Electromagnetic Compatibility, National Harbor, MD, USA*, August 2017.

[30] L. Kovalevsky, R. Langley, P.Besnier, and J.Sol, "Experimental Validation of the Statistical Energy Analysis for Coupled Reverberant Rooms," *IEEE International Symposium on Electromagnetic Compatibility, Dresden, Gr*, August 2015.

[31] Carl E. Hager, Justin D. Rison, and Gregory B. Tait, "Maximum Recieved Power Statistics within RF Reflective Enclosures for Hero and EMV Testing," August 2015, pp. 237–241.

[32] Neda Nourshamsi, J. C. West, and C. F. Bunting, "Effects of aperture dimension on maximum field level inside nested chambers by applying the generalized extreme value distribution," *IEEE International Symposium on Electromagnetic Compatibility*, pp. 628–633, June 29- August 3 2018.

[33] J. M. Mendel, *Estimation Theory for Signal Processing, Communication and Control*. Prentice Hall PTR, 1995.

[34] Samuel Kotz and Saralees Nadarajah, *Extreme Value distributions, Theorey and applications*. Imperial College Press, 2000.

[35] Eduardo S. Martins and Jery R. Stedinger, "Generalized Maximum-Likelihood Generalized Extreme-Value Quantile Estimators for Hydrologic Data," *Water Resources Research*, vol. 36, no. 3, pp. 737–744, March 2000.

[36] Kurtosis. [Online]. Available: https://www.mathworks.com/help/stats/kurtosis.html

[37] M. A. Stephens, "EDF statistics for goodness of fit and some comparisons," vol. 69, no. 347, pp. 730–737, September 1974.

[38] G. Gradoni and L. R. Arnaut, "Generalized extreme-value distributions of power near a boundary inside electromagnetic reverberation chambers," *IEEE Transaction On Electromagnetic Compatability*, vol. 52, no. 3, August 2010.

[39] Neda Nourshamsi, J. C. West, and C. F. Bunting, "Investigation of electromagnetic complex cavities by applying the generalized extreme value distribution," *IEEE International Symposium on Electromagnetic Compatibility, Long Beach, CA, USA*, pp. 622–627, June 29- August 3 2018.

[40] J. C. West, R. Bakore, and C. F. Bunting, "Statistics of the current induced within a partially shielded enclosure in a reverberation chamber," *IEEE Transaction On Electromagnetic Compatibility*, vol. 59, no. 6, December 2017.

[41] C. Hager and J. Rison, "On applying the generalized extreme value distribution to undermoded cavities within a reverberation chamber," National Harbor, MD. IEEE International Symposium Electromagnetic Compatability, August 2017, p. 682–686.

[42] L. Wasserman, *All of Statistics: A Concise Course in Statistical Inference*, ser. 1431-875X. Springer-Verlag New York, 2004, no. 1.

[43] G. B. Tait, C. Hager, M. B. Slocum, and M. O. Hatfield, "On measuring shielding effectiveness of sparsely moded enclosures in a reverberation chamber," *IEEE Transaction On Electromagnetic Compatability*, vol. 55, no. 2, April 2013.

[44] L. Arnaut, "Sampling distributions of random electromagnetic fields in mesoscopie or dynamic systems," Phys. Rev. E, Tech. Rep. pp.036601.1-036601.17, Sept. 2009.

[45] C. L. Holloway, D. A. Hill, J. M. Ladbury, and G. Koepke, "Requirements for an effective reverberation chamber: Unloaded or loaded," *IEEE Trans Antennas Propag*, vol. 48, no. 1, pp. 187 – 194, Feburary 2006.

[46] C. Vyhlidal, "Investigating the Corrolation between Quality Factor of Metal Cavities and Electromagnetic Radiation," Master's thesis, Oklahoma State University, June 2015.

[47] P. G. Bremner, D. H. Trout, G. Vazquaz, N. Nourshamsi, J. C. West, and C. F. Bunting, "Modal Q factor and modal overlap of electrically small avionics boxes," Long Beach, CA. IEEE International Symposium Electromagnetic Compatability, June 29- August 3 2018, pp. 286–291.

[48] C. L. Holloway, H. A. Shah, R. J. Prikl, K. A. Remley, D. A. Hill, and J. Ladbury, "Early time behavior in reverberation chambers and its effects on the relationships between coherence bandwidth, chamber decay time, RMS delay spread, and the chamber buildup time," vol. 54, no. 4, pp. 714–725, Apr. 2012.

[49] Neda Nourshamsi, M. T. Hagan, and C. F. Bunting, "Estimation of required absorbing material dimensions inside metal cavities using neural networks," *IEEE International Symposium on Electromagnetic Compatibility*, pp. 69–74, 7-11 August.

[50] Max. Sucher and Jerome Fox, *Handbook in Microwave Measurement, Second Volume*, Third Edition.

[51] F. D. Foresee and M. T. Hagan, "Gauss-Newton approximation to Bayesian learning," in *Neural Networks, 1997., International Conference on*, vol. 3. IEEE, 1997, pp. 1930–1935.

[52] P. Werbos, "Beyond regression: New tools for prediction and analysis in the behavioral sciences," Ph.D. dissertation, Harvard University, Cambridge, MA, 1974.

[53] G. A. Carpenter and S. Grossberg, "Hierarchical search using chemical transmitters in self-organizing pattern recognition architectures," *Neural Networks*, vol. 3, no. 2, pp. 129–152, December 1990.

[54] E. Genender, C. L. Holloway, K. A. Remley, J. M. Ladbury, G. Koepke, and H. Garbe, "Simulating the multipath channel with a reverberation chamber: Application to bit error rate measurements," *IEEE Trans Antennas Propag*, vol. 52, no. 4, pp. 766 – 777, April 2010.

[55] D. Senic, K. A. Remley, C. M. J. Wang, D. F. Williams, C. L. Holloway, D. C. Ribeiro, and A. T. Kirk, "Estimating and reducing uncertainty in reverberation-chamber characterization at millimeter-wave frequencies," *IEEE Transaction On Electromagnetic Compatability*, vol. 64, no. 7, p. 3130–3140, December 2016.

[56] J. Ladbury, G. Koepke, and D. Carnell, "Evaluaion of the nasa langley research center mode-stirred cahmber facility," NIST Technichal Note 1508, Technichal Report, January 1999.

[57] L. Arnaut, "Measurement uncertainty for reverberation chambers—i. statistics," NPL Report, TQE 002, 2008.

[58] G. Gradoni and L. Arnaut, "Minimum-value distribution of random electromagnetic fields for modeling deep fading in wireless communications," *Springre*, vol. 66, June 2011.

[59] C. L. Holloway, D. Hill, J. M. Ladbury, P. Wilson, G. Koepke, and J. Coder, "On the use of reverberation chambers to simulate a rician radio environment for the testing of wireless devices," *IEEE Trans Antennas Propag*, vol. 54, no. 11, pp. 3167 – 3177, November 2006.

[60] R. Magrogan, "Basic hazards of electromagnetic radiation to ordnance," Naval Surface Warefare Center, Tech. Rep.

[61] "Nelder Mead algorithm," *Scholarpedia*, vol. 4, no. 7, p. 2928, 2009.

[62] Nelder mead algorithm. [Online]. Available: http://adl.stanford.edu/aa222/lecture_notes_files/chapter6_gradfree.pdf

[63] H. Stark and J. W. Woods, *Probability and Random Processes with Application to Signal Processing*. Prentice Hall.

[64] S. Silfverskiold, M. Backstrom, and J. Loren, "Microwave field-to-wire coupling measurements in anechoic and reverberation chambers," *IEEE Transaction On Electromagnetic Compatability*, vol. 44, no. 1, p. 222–232, Feburary 2002.

[65] K. A. Remley, R. J. Pirkl, H. A. Shah, and C.-M. Wang, "Uncertainty from choice of mode-stirring technique in reverberation-chamber measurements," *IEEE Transaction On Electromagnetic Compatability*, vol. 55, no. 6, p. 1022–1030, December 2013.

[66] A. Cozza, "The role of losses in the definition of the overmoded condition for reverberation chambers and their statistics," *IEEE Transaction On Electromagnetic Compatability*, vol. 53, no. 2, pp. 296–307, December 2011.

[67] B. N. Taylor and C. E. Kuyatt, "Guidelines for Evaluating and Expressing the Uncertainty of NIST Measurement Results," *National Institute of Standards and Technology, Boulder, CO*, p. NIST Tech. Note 1297, 1994.

APPENDIX A

FUNDAMENTAL CONCEPTS IN STOCHASTIC SYSTEM

A.1 Overview

In this chapter we have a brief review of some fundamental concepts in the stochastic systems which is the basis of statistical description inside the reverberation chamber. In addition, the extreme value theory and the correlation coefficient are explained in details.

A.1.1 Random Variables

Consider an experiment H with sample description space Ω. The elements Ω , ζ are the outcomes of H. If to every ζ we assign a real number $X(\zeta)$, we establish a correspondence rule between ζ and R , the real line. Such a rule, subject to certain constraints is called a *random variable*. Thus a random variable is not really a variable but a function whose domain is Ω and whose range is some subset in real line [33]. Figure A.1 shows the mapping X, such an event (E_B) maps into the points on the real lines.

A.1.2 Cumulative Density Functions

Cumulative distribution function (CDF) of a real-valued random variable X, is the probability that X will take a value less than or equal to λ.

$$F_X(\lambda) = P(S : X(s) \leq \lambda), \tag{A.1}$$

Where S is sample space. The properties of CDF can be as follows [63]:

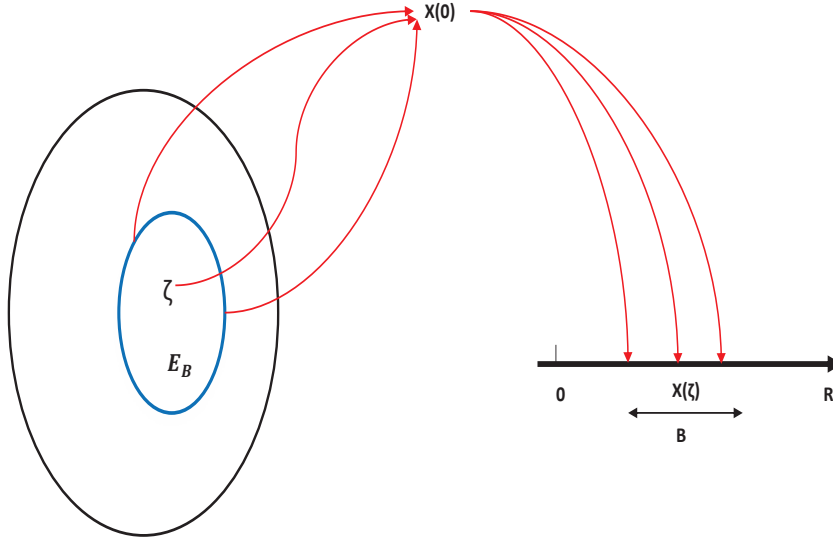- The CDF is non decreasing function which can not be negative.

Figure A.1: Symbolic representation of the action of the random variable X

- $\lim_{\lambda \to -\infty} F_X(\lambda) = 0$.

- $\lim_{\lambda \to +\infty} F_X(\lambda) = 1$.

- $P(S : \lambda_1 \leq X(s) \leq \lambda_2) = F_X(\lambda_2) - F_X(\lambda_1)$.

A.1.3 Probability Density Functions

Probability density function (PDF) can be defined [63]:

$$f_X(\lambda) = \frac{\partial F_X(\lambda)}{\partial \lambda}. \tag{A.2}$$

PDF provides a relative likelihood that the value of the random variable would equal that sample. The properties of PDF can be as follows [63]:

- $\int_{-\infty}^{+\infty} f_X(\lambda) d\lambda = 1$.

- $f_X(\lambda) \geq 0$.

- $F_X(\lambda) = \int_{-\infty}^{\lambda} f_X(\lambda) d\lambda$.

Figures A.2(a) and A.2(b) show CDF and PDF of Gaussian distribution.
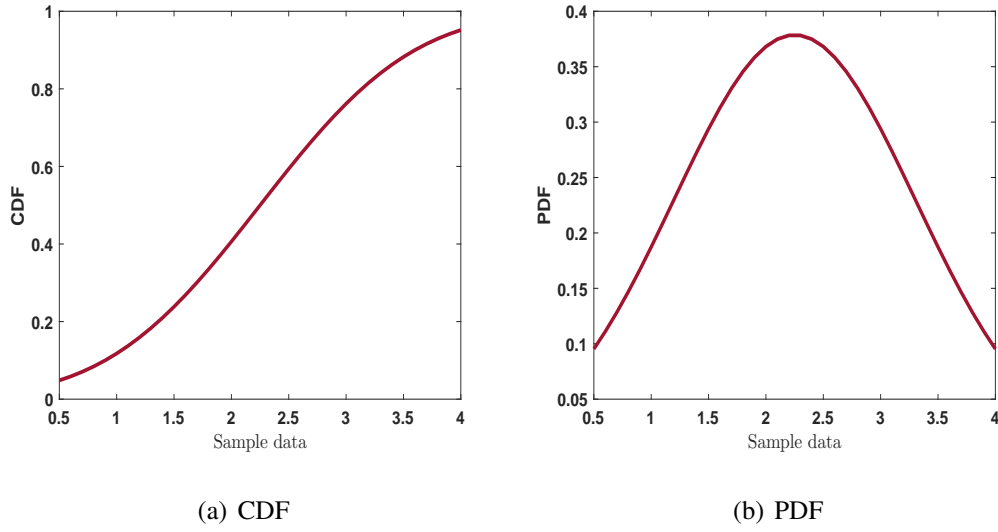
136

(a) CDF   (b) PDF

Figure A.2: CDF and PDF of Gaussian distribution $N(2.25, 1.05)$

A.1.4 The Mean and Variance of Probability Density Function

The expected value (first order moment) of a random variable X with PDF $f_X(\lambda)$ is defined [63] (for both discrete and continues random variables) :

$$E[X] = \int_{-\infty}^{+\infty} \lambda f_X(\lambda) d\lambda, \tag{A.3}$$

Where $f_X(\lambda)$ represents PDF. In this work the symbol μ_X or $E[X]$ used to show the expected value of X. The variance can be define as:

$$E[(X - \mu_X)^2] = \sigma_x^2. \tag{A.4}$$

The standard deviation can be defined as squared root of the variance.

A.1.5 The Extreme Value Theory

Suppose $X_1, X_2...., X_n$ are a sequence of independent and identically distributed random variables and $M_n = max\{X_1, X_2, ..., X_n\}$.

In theory, the exact distribution of the maximum can be derived [63]:

137

$$P(M_n \leq \lambda) = P(X_1 \leq \lambda, ..., X_n \leq \lambda)$$

$$= P(X_1 \leq \lambda).....P(X_n \leq \lambda) \tag{A.5}$$

$$= (F_X(\lambda))^n.$$

Therefore $P(M_n > \lambda)$ can be defined [63]:

$$P(M_n > \lambda) = (1 - F_X(\lambda))^n. \tag{A.6}$$

However, as can be seen it is important to know the original distribution in order to find the distribution of the maximum by applying Extreme Value Theory.

A.1.6   Correlation between Two Sets of Data

The correlation coefficient between two variables X and Y can be defined [33]:

$$\rho = \frac{\sigma_{XY}}{\sigma_X \sigma_Y}, \tag{A.7}$$

Where $\sigma_{XY}, \sigma_X, \sigma_Y$ show respectively the covariance between X and Y, variance of X and variance of Y. The covariance can be defined as:

$$\sigma_{XY} = E[(X - \mu_X)(Y - \mu_Y)], \tag{A.8}$$

Where μ_X, μ_Y already defined in section A.1.4. The correlation around zero ($\sigma_{XY} = 0$) shows the samples are uncorrelated.

APPENDIX B

NUMERICAL OPTIMIZATION

In this chapter we will explain some fundamental concepts about optimization performance, which is the applicable in Maximum likelihood Estimator. The objective of optimization is to find the value of x, which minimizes a performance index $F(x)$.

Nelder Mead algorithm is one of the well-known algorithms for multidimensional unconstrained optimization without derivatives. The method is frequently used to solve parametric estimation since it does not need any derivative. The algorithm is suitable for the function values are uncertain or for problems with discontinuous functions. This optimization finds the minimum value by using the concept of simplex, which is a special polytope with $N + 1$ vertices in N dimensions to find local minimum of a function with several variables.

Suppose there are $x_1, x_2, ..., x_{n+1}$ test points. The general algorithm could have steps as following [61]:

$1-$ The values at the vertices should be ordered; $f(x_1) \leq f(x_2) \leq ..... \leq f(x_{n+1})$. The centroid of all points (except x_{n+1}) need to be calculated:

$$x_m = \frac{1}{n}\sum_{i=1}^{n} x_i \tag{1}$$

$2-$ **Reflection**: Compute the reflection point $x_r = x_m + \alpha(x_m - x_{n+1})$ with $\alpha > 0$. If x_r is better than x_1, we step forward in the same direction to expansion. Figure 1 shows the reflection for two variables. However, if $f(x_r)$ is worst than the worst point, we move to step 4.

3− **Expansion**: The expansion step can be defined: $x_e = x_m + \gamma(x_r - xm)$ with $\gamma = 1$. Figure 3(a) shows the expansion for two variables.

4− **Contraction**: If $f(x_r) > f(x_{n+1})$, then $x_c = x_m - \beta(x_{n+1} - x_m)$ with $\beta = 0.5$, which is called inside contraction(ic). If $f(x_1) < f(x_r) < f(x_{n+1})$, $x_c = x_m + \beta(x_{n+1} - x_m)$, which is called outside contraction (oc). Figure 2 shows the inside and outside contraction for two variables.

After the expansion, we either accept the new point (if the value of the objective function is better than the best point) or we just accept the previous reflected point.
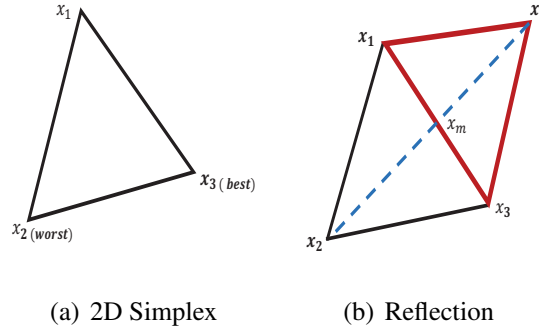

(a) 2D Simplex   (b) Reflection

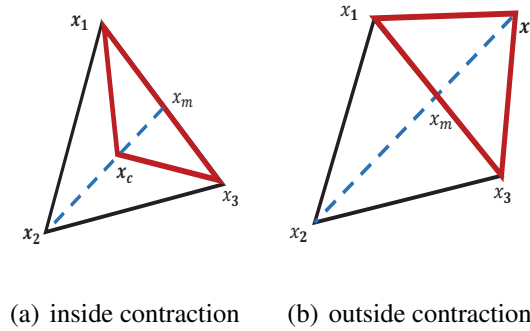Figure 1: 2D simplex and Reflection for two variables

(a) inside contraction   (b) outside contraction

Figure 2: Contraction (inside and outside for two variables)
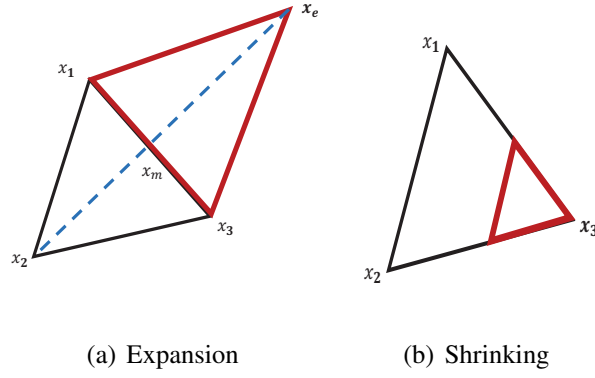
(a) Expansion   (b) Shrinking

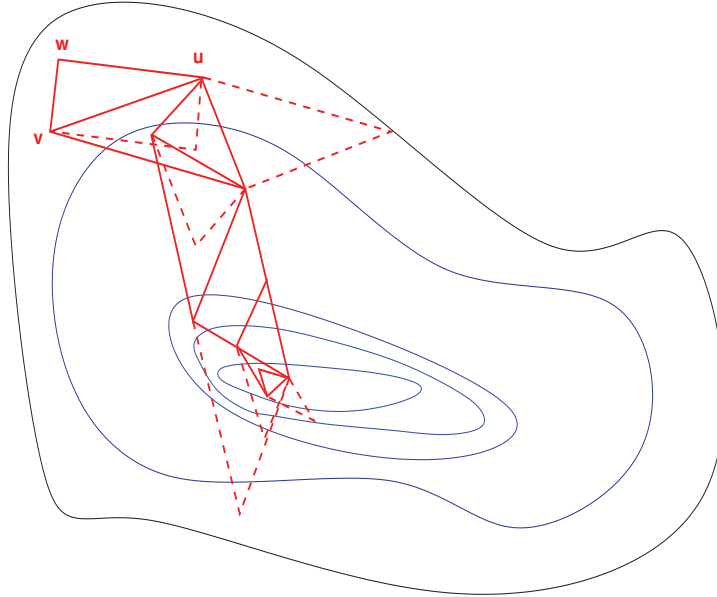Figure 3: Expansion and shrinking for two variables

Figure 4: Sequence of surplices that minimize a function (Dash lines show the reflection steps) [8]

$5-$ **Shrink**: If the all mentioned steps fail, we replace all points except the best (x_1) with $x_i = x_1 + \rho(x_i - x_1)$ with $\rho = 0.5$. Figure 3(b) shows the shrinking for two variables.

α, γ, β and ρ are respectively the reflection, expansion, contraction and shrink coefficients.

For two variables, a simplex is a triangle, and the method is a pattern search that com-

pares function values at the three vertices of a triangle. The worst case is the place that $f(x)$ is the largest. This would be replaced with new vertex. A new triangle would be formed and the search will be continued. The algorithm will continue and create a sequences of the triangles. This means that the function would be getting smaller and smaller at the vertices (the dimension of triangle is decreased) till the minimum point is reached. Figure 4 shows the a sequence of steps that minimize a function (2D results).

VITA

Neda Nourshamsi

Candidate for the Degree of

Doctor of Philosophy

Dissertation: STATISTICAL ANALYSIS OF ELECTROMAGNETIC COMPLEX CAVI-
TIES

Major Field: Electrical and Computer Engineering

Biographical:

Education:
Completed the requirements for the Doctor of Philosophy in Electrical Engineer-
ing at Oklahoma State University, Stillwater, Oklahoma in December, 2018.
Received the M.S. degree from Strasbourg, France, 2014, in Mechatonics and En-
ergy Engineering.
Received the B.S. degree from Tehran, Iran, 2007, in Electrical and Computer En-
gineering.

Experience:
Exchange Student at Oklahoma State University in August 2013 - June 2014.
Exchange Student (Erasmus program) at Université Libre de Bruxelles in January
2013 - June 2013.